2020

DIRECT METAL LASER SINTERING OF TI-6AL-4V ALLOY: PROCESS-PROPERTY-GEOMETRY EMPIRICAL MODELING AND OPTIMIZATION

Behzad Fotovvati

DIRECT METAL LASER SINTERING OF TI-6AL-4V ALLOY: PROCESS-PROPERTY-GEOMETRY EMPIRICAL MODELING AND OPTIMIZATION

by

Behzad Fotovvati

A Dissertation

Submitted in Partial Fulfillment of the

Requirements for the Degree of

Doctor of Philosophy

Major: Mechanical Engineering

The University of Memphis

May 2020

ACKNOWLEDGEMENTS

I would first like to thank Dr. Ebrahim Asadi, for his constant support, patience, motivation, enthusiasm, and help during these past four years. I am extremely grateful to have him as my advisor and much more.

I am grateful to Dr. Gladius Lewis, Dr. Amir Hadadzadeh, Dr. Madhusudhanan Balasubramanian, and Dr. Ranganathan Gopalakrishnan who devoted their precious time for being in my dissertation committee and for the valuable and constructive suggestions. I would also like to thank Dr. Steve Wayne and Dr. Ali Fatemi for all the valuable lessons I have learned from them.

I would also like to thank my family for supporting me and providing an environment for me to grow and reach my goals.

At last but not the least, I would like to thank the love of my life, Hanieh, who has stood by me through all my travails and gave me support and courage, discussed ideas, and prevented several wrong turns.

PREFACE

Based on the work of this dissertation, three papers are published, and one manuscript is prepared to be submitted, as follows:

The paper presented in chapter two, i.e. “A Review on Melt-Pool Characteristics in Laser Welding of Metals”, is published in *Advances in Materials Science and Engineering*, volume 2018, pages 1-18, 2018.

The paper presented in chapter three, i.e. “Size effects on geometrical accuracy for additive manufacturing of Ti-6Al-4V ELI parts”, is published in *The International Journal of Advanced Manufacturing Technology*, volume 104, pages 5-8, 2019.

The paper presented in chapter four, i.e. “Process-property-geometry correlations for additively manufactured Ti–6Al–4V sheets”, is published in *Materials Science and Engineering: A*, volume 760, pages 431-447, 2019.

The paper presented in chapter five, i.e. “Application of Taguchi, Response Surface, and Artificial Neural Networks Toward Optimizing the Processing Parameters for Direct Metal Laser Sintering of Ti-6Al-4V Alloy”, is submitted to *Additive Manufacturing*, 2020.

This work is supported by the FedEx Institute of Technology, Medtronic Sofamor Danek USA Inc, US Naval Air System Command, and the University of Memphis through the “Herff Graduate Fellowship” awarded to B. Fotovvati.

ABSTRACT

Fotovvati, Behzad. Ph.D. The University of Memphis. May 2020. Dissertation title: Direct metal laser sintering of Ti-6Al-4V parts: process-property-geometry correlations. Major Professor: Dr. Ebrahim Asadi.

Direct metal laser sintering (DMLS) is a widely used powder bed fusion (PBF) additive manufacturing (AM) technology that offers extensive capabilities to fabricate complex metallic components. In the DMLS process, part fabrication involves small moving melt-pools formed by the interaction of laser beam and metal powders. The formation of a melt-pool and subsequently its rapid solidification results in alteration of properties and microstructure of the product. Therefore, understanding and predicting relationships between DMLS process parameters and melt-pool characteristics is critical to control and improve the properties of parts. The melt-pool formation in this process is very similar to what occurs in metal laser welding, having solid metallic parts rather than metal powders, plus laser welding is more investigated and is better known compare to DMLS. So, a critical review of the literature on experimental and modeling studies on laser welding, with the focus being on the influence of process parameters on geometry, thermodynamics, fluid dynamics, microstructure, and porosity characteristics of the melt-pool is presented. However, the DMLS process has several variables, altering which increases the complexity of the correlations between them and the final properties. A solution is to isolate the variable sets from the other ones during the investigation. Therefore, keeping all the processing parameters constant, an investigation of the size and geometry dependence of the dimensional accuracy of the DMLS process is presented. For all features, with different geometries and different sizes, the percent error significantly

increases with decreasing the feature size. Then, the effect of thickness, orientation, distance from free edges, and height on the mechanical properties and their correlations to material microstructure and thermal history as dictated by DMLS process parameters are investigated and the results are correlated to the porosity volume fraction and their elongation direction, prior β grain width and orientation, β nanoparticle volume fraction, martensitic α' decomposition to α+β and α" orthorhombic structure, and Oxygen content variation. Furthermore, the influence of five most influential DMLS processing parameters, i.e. laser power, scan speed, hatch spacing, layer thickness, and stripe width, on relative density, microhardness, and surface roughness are thoroughly investigated. Two design of experiment (DoE) methods, including the Taguchi and fractional factorial DoE for response surface method (RSM), along with an artificial neural network (ANN) are designed and trained to predict the response values. A multi-objective RSM model is developed for the optimization of DMLS processing parameters. It is shown that the proposed ANN model can most accurately predict various response properties of DMLS components.

TABLE OF CONTENTS

List of Tables

TABLE PAGE

List of Figures

FIGURE PAGE

List of Abbreviations

AlN: Aluminum Nitride

AM: Additive Manufacturing

ANN: Artificial Neural Network

ANOVA: Analysis of Variances

ASTM: American Society for Testing and Materials

C: Carbon

CD: Channel Diameter

CI: Confidence Interval

DG: Diagonal Gap

DMLS: Direct Metal Laser Sintering

DoE: Design of Experiments

EBM: Electron Beam Melting

EDM: Electrical Discharge Machining

FDM: Fused Deposition Modeling

FEA: Finite Elements Analysis

H: Hydrogen

HAZ: Heat-Affected Zone

HIP: Hot Isostatic Pressing

HT: Heat Treatment

HV: Vickers Hardness

IB: Inverse Bremsstrahlung

LOF: Lack of Fusion

ML: Machine learning

MMA: Molten-Metal Area

MSD: Mean Square Deviation

N: Nitrogen

Nd: YAG: Neodymium-doped Yttrium Aluminum Garnet

O: Oxygen

OM: Optical Microscopy

PBF: Powder Bed Fusion

RD: Rod Diameter

RSM: Response Surface Method

SE fit: Standard Error of the fit

SEM: Scanning Electron Microscopy

ST: Square Thickness

TEM: Transition Electron Microscopy

TT: Tube Thickness

VG: Vertical Gap

WT: Wall Thickness

XRD: X-Ray Diffraction

1. Introduction

Among various types of manufacturing processes for different applications based on material and design, Additive Manufacturing (AM) technologies have provided several advantages such as design freedom, manufacturing of complex structures, reduction in raw material consumption, reduced inventory management need, etc. [1]. Powder bed fusion (PBF) is an AM technique based on spreading a thin layer of metal powders and scanning the part geometry using a moving laser. Repeating this process in successive layers generates the designed three-dimensional geometry. Direct metal laser sintering (DMLS) is a widely adopted PBF-AM process to produce high-performance metallic parts with complex geometries via selective laser scanning of thin layers of metal powders successively on top of each other. During the DMLS process, the interaction of laser beam and metal powders forms small moving melt-pools (Figure 1), size of which is influenced by many variables, such as material, laser power, and scan speed [2]. The formation of a melt-pool and subsequently its rapid solidification results in alteration of properties and microstructure of the product [3,4]. Therefore, understanding and predicting relationships between DMLS process parameters and melt-pool characteristics is critical to control and improve the properties of products. A similar phenomenon occurs in the metal laser welding process, which is more investigated in the literature and is better known compared to the DMLS process [5]. So, in chapter two, a critical review of the literature on experimental and modeling studies on laser welding, with the focus being on the influence of process parameters on geometry, thermodynamics, fluid dynamics, microstructure, and porosity characteristics of the melt-pool is presented.

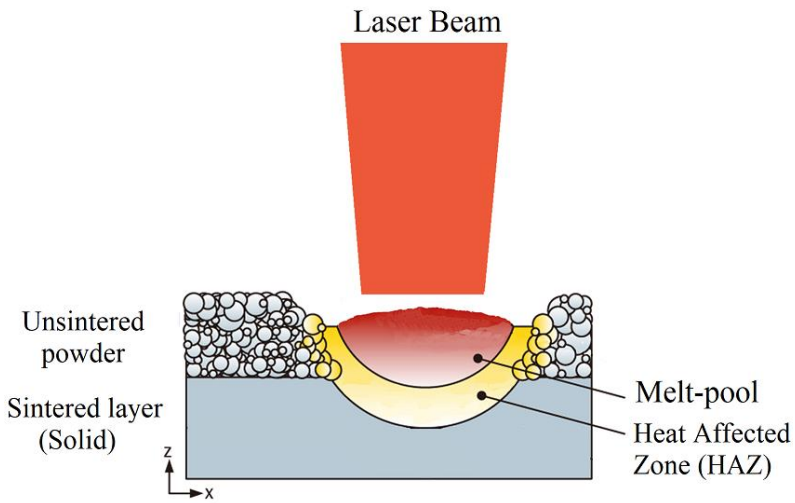

Figure 1. A schematic of the formation of melt-pool and heat affected zone (HAZ) around it during the DMLS process.

Although the DMLS process is widely used in many industries, the geometrical accuracy of the parts produced by this method is questionable when dealing with very small features. Furthermore, the mismatch between the as-designed and as-manufactured geometry of parts can lead to the inconsistency in the mechanical properties of AM products [6]. Dimensional accuracy of DMLS-manufactured parts is affected by several factors, such as processing parameters (i.e. laser power, scan speed, etc.) [7], which change the characteristics and geometry of the melt-pool [8], the overall temperature of the part during DMLS, which is a function of size and shape of the geometry, and part location on the build platform [9]. The effects of these factors should be investigated in isolation from each other. So, first, we keep the processing parameters constant and investigate the effects of other factors. Then, we evaluate the variations of the properties while the processing parameters are changing. Therefore, the third chapter is dedicated to the investigation of the effects of size, geometry, and location on the build plate on the dimensional accuracy of DMLS-manufactured Ti-6Al-4V features. The effect of global

shrinkage, laser curing zone, and partially fused powders are eliminated from the size and geometry dependent dimensional inconsistency during the process. The design of dimensional features includes holes, gaps, walls, squares, tubes, and rods with different sizes. A mathematical model is proposed and tested successfully for predicting the size and geometry dependent dimensional inconsistencies of DMLS-manufactured Ti-6Al-4V parts.

Extending the application of the DMLS process to critical components requires a deeper understanding of the process-properties-geometry correlation in this process. As dictated by the process, DMLS-manufactured parts experience a cyclic thermal history, which is a function of location in the part and DMLS process parameters [10], resulting in the mechanical performance of DMLS-manufactured parts to vary by the feature size and the location in the geometry [11]. So, understanding these variations and their correlations to material microstructure and defects is a key to better understand the DMLS process and improve the process parameters. Furthermore, the process-property-geometry correlations can feed to geometry optimization methodologies for AM, such as those currently used to reduce component weight and improve performance [12]. Therefore, in this work, we investigate mechanical performance, microhardness, porosity, and microstructure of DMLS- and traditionally manufactured thin sheets. Specimens with different geometries and in different orientations are cut from these sheets using wire electrical discharge machining (EDM) to minimize the cutting effects and represent “in component” properties. The effects of sheet thickness and the orientation of specimens with the build platform on the mechanical response of DMLS-manufactured sheets are investigated. Moreover, we study the effect of specimen distance from the free edge

followed by the effect of specimen height from the build platform on the mechanical properties of DMLS-manufactured sheets. Then, the mechanical properties are correlated to the porosity volume fraction and their elongation direction, prior β grain width and orientation, β nanoparticle volume fraction, martensitic α' decomposition to α+β and α" orthorhombic structure, and oxygen content variation.

In addition to the above-mentioned geometry-property correlations in the DMLS process with constant processing parameters, there are correlations between processing parameters and properties of parts with the same size and geometry. The DMLS process offers extensive opportunities to alter the microstructure and subsequently to enhance the mechanical properties of the products by designing targeted processing parameters [13]. There are more than 130 factors/process parameters affecting the quality of the manufactured parts in the DMLS process [14]. Design of experiments (DoE), which includes a branch of applied statistics, is a proper technique to deal with the planning and analyzing controlled tests to evaluate the factors that control and affect particular response values or properties. The Taguchi with orthogonal arrays and response surface method (RSM) are among DoE techniques to determine design factor settings to improve or optimize the performance or response of a process. RSM can be used with a full factorial DoE or fractional factorial DoE. A complete factorial DoE with a large number of factors requires a very large number of observations. Therefore, the reduction of the size of a complete factorial experiment can be very helpful by employing the fractional factorial design. Another technique for controlling the properties based on the process parameters is Artificial Neural Networks (ANN), which is a mathematical model mapping an input space to an output space. Once the ANN is trained, it is capable of

predicting the responses based on unseen input values. Numerous research studies have been devoted to investigating the correlations between the DMLS process parameters and various properties of the fabricated parts such as surface quality, internal porosity, and mechanical performance [15–22]. Most of the studies in the literature that employed DoEs based on the Taguchi and RSM methods are limited to a single target property for optimization based on the variation of few numbers of AM process parameters. Most notably, layer thickness has been precluded from the list of the DMLS processing parameters for optimization. However, the layer thickness is reported [23–25] as the most significant parameter in the DMLS process. Furthermore, there is a lack of comprehensive study to compare the optimization of DMLS processing parameters via Taguchi, RSM, and ANN methods. In the fifth chapter of this dissertation, the five most influential parameters, i.e. laser power, scan speed, hatch spacing, layer thickness, and stripe width, are considered as the design factors for DMLS processing of Ti-6Al-4V alloy. Top, upskin, and downskin surface roughness parameters, microhardness, and relative density are considered as the target properties for optimization of the DMLS processing parameters. The correlations between the DMLS processing parameters and the target properties are discussed and modeled extensively, and the sets of optimum processing parameters predicted by each method are determined and compared with each other. The results showed that all three models exhibit reasonable predictive capabilities while ANN outperforms the predictive capabilities of RSM and Taguchi.

Organization

Chapter two of this dissertation presents a literature review on experimental and modeling studies on the effects of laser welding process parameters, on geometry, thermodynamics, fluid dynamics, microstructure, and porosity characteristics of the melt-pool. In the third chapter, the effects of size, geometry, and location on the build plate on the dimensional accuracy of DMLS-manufactured parts are investigated. Chapter four correlates the mechanical properties to the porosity volume fraction and their elongation direction, the microstructural properties, and oxygen content variation. Finally, the correlations between the DMLS processing parameters and the responses are discussed, and predictive models for this process are developed and compared in chapter five.

References

[1] M. Attaran, The rise of 3-D printing: The advantages of additive manufacturing over traditional manufacturing, Bus. Horiz. 60 (2017) 677–688. doi:10.1016/J.BUSHOR.2017.05.011.

[2] L. Scime, J. Beuth, Melt pool geometry and morphology variability for the Inconel 718 alloy in a laser powder bed fusion additive manufacturing process, Addit. Manuf. 29 (2019) 100830. doi:10.1016/j.addma.2019.100830.

[3] A. Keshavarzkermani, E. Marzbanrad, R. Esmaeilizadeh, Y. Mahmoodkhani, U. Ali, P.D. Enrique, N.Y. Zhou, A. Bonakdar, E. Toyserkani, An investigation into the effect of process parameters on melt pool geometry, cell spacing, and grain refinement during laser powder bed fusion, in: Opt. Laser Technol., Elsevier Ltd, San Francisco, CA, 2019: pp. 83–91. doi:10.1016/j.optlastec.2019.03.012.

[4] M. Bisht, N. Ray, F. Verbist, S. Coeck, Correlation of selective laser melting-melt pool events with the tensile properties of Ti-6Al-4V ELI processed by laser powder bed fusion, in: TMS 2020 149th Annu. Meet. Exhib. Suppl. Proc., Springer, Cham, San Diego, CA, 2020: pp. 353–365. doi:10.1016/j.addma.2018.05.004.

[5] T.R. Allen, F. AlTal, B.J. Simonds, J.M. Fraser, Measurement of melt pool dynamics in stationary laser welding using inline coherent imaging (Conference Presentation), in: S. Kaierle, S.W. Heinemann (Eds.), High-Power Laser Mater. Process. Appl. Diagnostics, Syst. VIII, SPIE, 2019: p. 15. doi:10.1117/12.2509003.

[6] D.A. Hollander, M. Walter, T. Wirtz, R. Sellei, B. Schmidt-Rohlfing, O. Paar, H.-

J. Erli, Structural, mechanical and in vitro characterization of individually structured Ti–6Al–4V produced by direct laser forming, Biomaterials. 27 (2006) 955–963. doi:10.1016/J.BIOMATERIALS.2005.07.041.

[7] L. Zhang, S. Zhang, H. Zhu, Z. Hu, G. Wang, X. Zeng, Horizontal dimensional accuracy prediction of selective laser melting, Mater. Des. 160 (2018) 9–20. doi:10.1016/j.matdes.2018.08.059.

[8] B. Fotovvati, S.F. Wayne, G. Lewis, E. Asadi, A Review on Melt-Pool Characteristics in Laser Welding of Metals, Adv. Mater. Sci. Eng. 2018 (2018). doi:10.1155/2018/4920718.

[9] J. Allison, C. Sharpe, C.C. Seepersad, A Test Part for Evaluating the Accuracy and Resolution of a Polymer Powder Bed Fusion Process, J. Mech. Des. 139 (2017) 100902. doi:10.1115/1.4037303.

[10] N.D. Ghate, B. Gaur, A. Shrivastava, Effect of Scanning Strategy on Additively Manufactured Ti6Al4V, in: Miner. Met. Mater. Ser., Springer, 2020: pp. 353–365. doi:10.1007/978-3-030-36296-6_33.

[11] B.E. Carroll, T.A. Palmer, A.M. Beese, Anisotropic tensile behavior of Ti-6Al-4V components fabricated with directed energy deposition additive manufacturing, Acta Mater. 87 (2015) 309–320. doi:10.1016/j.actamat.2014.12.054.

[12] N. Shamsaei, A. Yadollahi, L. Bian, S.M. Thompson, An overview of Direct Laser Deposition for additive manufacturing; Part II: Mechanical behavior, process parameter optimization and control, Addit. Manuf. 8 (2015) 12–35. doi:10.1016/J.ADDMA.2015.07.002.

[13] Y.M. Wang, T. Voisin, J.T. McKeown, J. Ye, N.P. Calta, Z. Li, Z. Zeng, Y. Zhang, W. Chen, T.T. Roehling, R.T. Ott, M.K. Santala, P.J. Depond, M.J. Matthews, A. V. Hamza, T. Zhu, Additively manufactured hierarchical stainless steels with high strength and ductility, Nat. Mater. 17 (2018) 63–70. doi:10.1038/NMAT5021.

[14] H. Shipley, D. McDonnell, M. Culleton, R. Coull, R. Lupoi, G. O'Donnell, D. Trimble, Optimisation of process parameters to address fundamental challenges during selective laser melting of Ti-6Al-4V: A review, International Journal of Machine Tools and Manufacture 128 (2018) 1-20.

[15] C. Qiu, M. Al Kindi, A.S. Aladawi, I. Al Hatmi, A comprehensive study on microstructure and tensile behaviour of a selectively laser melted stainless steel, Sci. Rep. 8 (2018). doi:10.1038/s41598-018-26136-7.

[16] G. Kasperovich, J. Haubrich, J. Gussone, G. Requena, Correlation between porosity and processing parameters in TiAl6V4 produced by selective laser melting, Mater. Des. 105 (2016) 160–170. doi:10.1016/J.MATDES.2016.05.070.

[17] G. Casalino, S.L. Campanelli, N. Contuzzi, A.D. Ludovico, Experimental investigation and statistical optimisation of the selective laser melting process of a maraging steel, Opt. Laser Technol. 65 (2015) 151–158. doi:10.1016/j.optlastec.2014.07.021.

[18] S. Pal, H.R. Tiyyagura, I. Drstvenšek, C.S. Kumar, The Effect of Post-processing and Machining Process Parameters on Properties of Stainless Steel PH1 Product Produced by Direct Metal Laser Sintering, Procedia Eng. 149 (2016) 359–365. doi:10.1016/j.proeng.2016.06.679.

[19] A. Charles, A. Elkaseer, L. Thijs, V. Hagenmeyer, S. Scholz, Effect of process parameters on the generated surface roughness of down-facing surfaces in selective laser melting, Appl. Sci. 9 (2019) 1–13. doi:10.3390/app9061256.

[20] N. Perevoshchikova, J. Rigaud, Y. Sha, M. Heilmaier, B. Finnin, E. Labelle, X. Wu, Optimisation of selective laser melting parameters for the Ni-based superalloy IN-738 LC using Doehlert's design, Rapid Prototyp. J. 23 (2017) 881–892. doi:10.1108/RPJ-04-2016-0063.

[21] J.C. Fox, S.P. Moylan, B.M. Lane, Effect of Process Parameters on the Surface Roughness of Overhanging Structures in Laser Powder Bed Fusion Additive Manufacturing, Procedia CIRP. 45 (2016) 131–134. doi:10.1016/J.PROCIR.2016.02.347.

[22] M. Sadowski, L. Ladani, W. Brindley, J. Romano, Optimizing quality of additively manufactured Inconel 718 using powder bed laser melting process, Addit. Manuf. 11 (2016) 60–70. doi:10.1016/j.addma.2016.03.006.

[23] M. Hiren, M.E. Gajera, K.G. Dave, V.P. Jani, Experimental investigation and analysis of dimensional accuracy of laser-based powder bed fusion made specimen by application of response surface methodology, Prog. Addit. Manuf. (2019). doi:10.1007/s40964-019-00076-8.

[24] C. Qiu, C. Panwisawas, M. Ward, H.C. Basoalto, J.W. Brooks, M.M. Attallah, On the role of melt flow into the surface structure and porosity development during selective laser melting, Acta Mater. 96 (2015) 72–79. doi:10.1016/J.ACTAMAT.2015.06.004.

[25] J. Sun, Y. Yang, D. Wang, Parametric optimization of selective laser melting for forming Ti6Al4V samples by Taguchi method, Opt. Laser Technol. 49 (2013) 118–124. doi:10.1016/j.optlastec.2012.12.002.

2. A Review on Melt-Pool Characteristics in Laser Welding of Metals

2.1 Introduction

Laser is a coherent single-phase beam of lights from a single wavelength (monochromatic) with low beam divergence and high-energy content, which creates heat when it strikes a metal surface. The advent of high-power (multi-kW) lasers in the 1970s [1] opened the door to many metal working applications, which, previously, had been done using conventional high-flux heat sources, such as reacting gas jets, electric discharges, and plasma arcs. One metal working application of lasers is laser welding, which requires power density > 10^3 kW cm^{-2} [2]. In laser welding, two adjacent or stacked metal pieces are fused together by melting the parts at the weld line; usually, the process is conducted under an inert gas flow with or without addition of material to the weld line. The moving melted volume is called the melt-pool (Figure 2). The size of this pool, which is on order of 1 mm, is influenced by many variables, such as material, laser power, and welding speed.

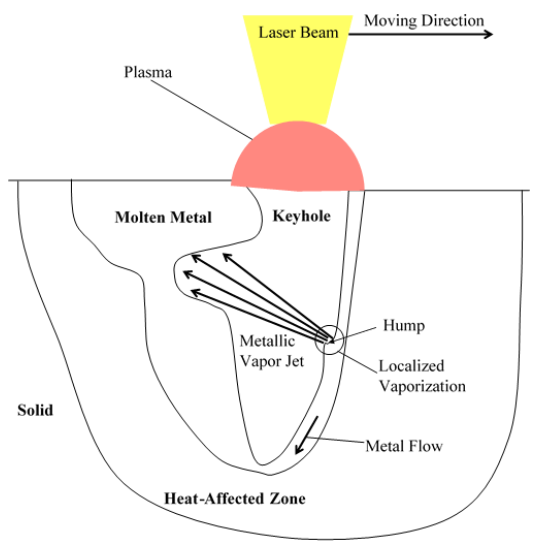

Figure 2. A cross sectional schematic of a side view (the interface between two solids) of the melt-pool formed during a laser welding process.

The deep volume directly under the laser focus area is called the keyhole, within which the high energy of the laser creates heating rates > 10^9 K s^{-1} [3]. Thus, the material in the keyhole is rapidly melted and even boiled, thereby creating a metallic plasma around it. Boiling of the material maximizes the absorption of the laser energy by the material because it turns the keyhole to a black body [4]. The amount of absorbed energy in the material decreases exponentially through the thickness, as predicted by the Beer–Lambert law. A smaller portion of the absorbed energy is conducted away through re-radiation and convection from the surface while the rest is conducted into the substrate. An intense recoil pressure created by evaporation of the material in the keyhole generates a vapor jet and a fluid flow in the keyhole and the melt-pool (Figure 2) [5]. In addition, the surrounding area of the melt-pool that is still in the solid state will reach temperatures high enough to change the microstructure of the material or to cause solid-state phase transformation, depending on the material thermodynamics. This area is called the heat-affected zone (HAZ). Hereafter, we use the term “melt-pool” to refer to the combination of the keyhole, the molten-metal area (MMA), and the HAZ. Laser welding mechanisms can be divided into two categories based on the existence of the keyhole: keyhole mode and conduction mode. Keyhole-mode welding is more common because it produces narrow HAZs. However, keyhole oscillations and closures result in instabilities of the melt-pool, leading to creation of pores in the welded zones. On the other hand, there is more stability in the conduction mode since vaporization is minimal. Conduction-mode welds are produced using low-power laser beams; as such, these welds are shallower

rather than keyhole-mode welds [6]. The focus of this review is keyhole-mode laser welding.

Melt-pool characteristics directly control the quality of the weld; for example, porosity in the weld through keyhole thermodynamics and residual stresses through HAZ thermomechanics. As a result, one of the main goals of many research studies is to understand the relationships between weld quality and laser welding process parameters (such as laser type and laser power), substrate temperature, and melt-pool characteristics [7–12]. There are different types of lasers, three widely used ones being neodymium-doped yttrium aluminum garnet (Nd:YAG), CO_2, and argon lasers. Lasers differ in characteristics, such as maximum output power and pulse repetition rate that they can provide and, as such, choice of laser should be based on the application being considered. For instance, Morgan et al. [13] conducted density analysis experiments on 316L stainless steel and chose Nd-YAG laser over CO_2 laser due to increased absorption of a 1.064 μm wavelength by metallic powder compared to a longer wavelength (10.64 μm) [14].

Locke et al. [15] carried out one of the early experiments on laser welding of metals. They used laser power levels of 8 kW and 20 kW, leading to penetration depth and speed that had not been possible previously. The penetration depth achieved was 12.7 mm at a ratio of 2.54 m min^{-1} in a 5 to 1 depth-to-average-width fusion zone in 304 stainless steel at a 20-kW laser power level. The state of the art of laser welding of metals and associated melt-pool characteristics in those early days of research was reviewed by Mazumder in 1982 [2] and in 1987 [16]. Since then, laser welding of metals has advanced significantly in many aspects, such as welding materials, process monitoring,

computational modeling, and quality. There are a few review papers in the literature that deal with recent advancements in laser welding of metals. In 1989, David and Vitek [17] focused on the solidification behavior of the melt-pool and investigated the correlation between weld metal microstructure and solidification parameters such as crystal growth rates and the consequent interface cooling rates. They presented a diagram showing the variation of weld microstructure as a function of cooling rate, growth rate, and combination(s) of these variables. In 2003, Cao et al. [18,19] reviewed research and progress in laser welding of wrought Al alloys. They reviewed findings regarding the influence of an assortment of parameters, which they divided into three categories (laser-, process-, and material-related parameters), on weld quality. They quantified the weld quality by metallurgical microstructures and defects, such as porosity, cracking, oxide inclusions, and loss of alloying elements, as well as mechanical properties of the weld, such as hardness, tensile strength, fatigue strength, and formability. In 2005, Shao et al. [20] reviewed on-the-fly monitoring techniques for inspecting the laser welding process, highlighting the advantages and limitations of acoustic, optical, visual, thermal, and ultrasonic techniques. In 2006, Cao and coworkers [21] conducted a similar review but focused on Mg alloys. In 2014, Liu et al. [22] reviewed laser welding studies of dissimilar Mg and Al alloys. Their review also included discussion of progress on research on other welding techniques applied to these alloys, including solid-state processes and fusion welding. The authors stated that a challenge in welding dissimilar Mg and Al alloys is the formation of brittle intermetallic compounds, which can be addressed by eliminating or reducing the Mg-Al intermetallic reaction layer through careful selection of process parameters.

Modeling the laser welding process has been another major research focus. This is challenging due to the multi-physics nature of the problem (see Figure 1); that is, it involves laser-material interaction, fluid flow, large temperature variation, plasma formation, vapor-liquid-solid coexistence, and possible solid-state phase transformation [4,23–25]. As analytical solution of the laser welding process is not possible (except in the case of a simplified physics and geometry model), numerical/computational approaches have been taken. In 2005, Mackwood and Crafer [26] reviewed the literature on thermal modelling up to 2002. They divided the work conducted into categories based on the welding method, such as arc, resistance and friction, as well as welding processes, such as alloying, cladding and surface hardening. The review covered basic analytical solutions, such as a moving/fixed point heat source combined with a line source of heat, along with numerical solutions, including standard heat transfer solutions, welding dissimilar metals, multi-pass welding, melt-pool models, and keyhole models. Also, in 2005, Yaghi and Becker [27] reviewed thermal and mechanical welding simulations in which finite element analysis (FEA) was used. The simulations included heat flow processes and solid-state phase transformations occurring in the welding process. They discussed several relevant modelling considerations (such as parametric studies of residual stresses), influence of material properties on residual stresses, and combination of welding simulation with other heat transfer engineering processes. In 2012, He [28] updated the review of FEA studies on laser welding, with special attention to the simulation of defect formation. He discussed numerical problems in FEA of laser welding, including materials modeling, meshing procedure, and failure criteria. He concluded that establishing an accurate and reliable finite element model of laser welding

is very difficult because the process is a complex phenomenon that comprises many interrelated mechanisms and metallurgical processes. In 2015, Svenungsson et al. [29] conducted a review of modeling investigations of the keyhole and categorized these models based on the considerations and assumptions used in constructing the models.

Most reviews on laser welding are limited to either a specific material or method of study, namely, experimental, on-the-fly monitoring, or computational. In other words, there is no review on the state of the art on the properties of the melt-pool and their relationship to the welding process parameters and weld quality. In the present review, we focus on these aspects. Thus, the present review focuses on the following melt-pool characteristics: 1) geometrical features, such as penetration depth, width, HAZ geometry, keyhole geometry, and MMA geometry; 2) thermodynamics characteristics, such as laser energy absorption, surface temperature, cooling rates, and temperature map in the melt-pool, 3) fluid dynamic characteristics, such as fluid flow in the melt-pool and vaporization in the keyhole, 4) resulting microstructures, and 5) porosity characteristics, including factors that influence porosity formation and methods to avoid it. Due to the multi-physics and integrated nature of the melt-pool, in some literature reports, there may be some overlap coverage of the above-mentioned aspects. In each section of the present review, we critically discuss the state of the art in determination of the considered melt-pool characteristic, its variation with process parameters, and its influence on commonly-used weld quality quantifiers, such as microstructure and mechanical properties. In the final section, we summarize the key points made and identify some gaps in the reviewed models of laser welding of metals that hinder full characterization of the process.

2.2 Melt-Pool Geometry

The magnitude and distribution of cooling rates, temperature, and the maximum thickness that can achieved a single welding pass is determined by the melt-pool geometry [7]. Additionally, the microstructure of the fusion zone is also influenced by the melt-pool geometry. There are several studies on the influence of laser power and welding speed on melt-pool geometrical features (Table 1). A summary of optimum laser welding process parameters, for a selection of metals and alloys materials, is given in Table 1. Summaries of studies on the influence of laser welding process variables on melt-pool and keyhole features presented in the Appendix.

Table 1. Influence of two laser welding parameters on various melt-pool geometry parameters

Geometry parameter	Process parameter	
	Laser power	Welding speed
Melt-pool depth	+[a]	-[b]
Melt-pool width	+[c]	-[d]
Melt-pool depth/width ratio	NS	+ [e]
Melt-pool length	+[f]	-[g]
Keyhole radius	+[g]	-[g]
Cooling rate	-[h]	+[i]
Melt-pool surface area	+[j]	-[k]
Vaporization rate	+[l]	NS

+: Direct relationship, -: inverse relationship; NS: Not stated in the report.
[a] [30–38]. [b] [31,33,37,39–42]. [c] [33–38,43–45]
[d] [12,31,33,37,39,42,43,46]. [e] [30]. [f] [32,43].
[g] [43,46]. [h] [7,8]. [i] [8].
[j] [44,47]. [k] [39,42,48]. [l] [45,47].

In laser welding applications, the maximum achievable welding speed is limited by the maximum available laser power. For economic reasons, it is desirable to apply the

highest possible speed during laser welding, while a full penetration is achieved at the same time. A feedback controller, in which an optical sensor measures the intensity of the melt-pool radiation and exports it to a feedback control system, has been described by Postma et al. [49]. They also proposed a dynamic model, which describes the sensor and laser source dynamics, using system identification techniques. This model, which uses laser power as the input and the modeled sensor signal as the output, is capable of maintaining full penetration in the presence of artificial power variations and speed changes. This procedure optimizes the welding speed without risking lack of penetration.

Surface structure and hardness of the substrate after laser-related processes are also affected by process parameters. Ashby and Easterling [53] conducted experiments and combined the equations of heat flow and kinetics to evaluate the near-surface structure and hardness after laser treatment. Using a Gaussian heat source for their model, they presented diagrams, which show the structure and the hardness of the surface, as a function of process parameters. Using these diagrams, the maximum achievable surface hardness without surface melting that results from using an optimum combination of process parameters is identified.

In the process of deep-penetration welding, a high energy density is transferred to the workpiece through the keyhole; therefore, the flows of metal vapor inside the keyhole and the molten material around it play an important role in the welding process, and the shape of the keyhole would highly affect the weld quality. One approach that is employed to evaluate the shape of the keyhole in this process is to estimate its cross-sectional area in each depth.

Table 2. Optimum laser welding parameters for a selection of metals and alloys

Metal/alloy	Parameter			
	Laser power (kW)	Welding speed ($m.min^{-1}$)	Focal position (relative to surface) (mm)	Shielding gas
Mg alloy, WE43 [37]	2	2	0 or -1	Helium
Mg alloy, AZ91 [37]	2	3	0	Helium
Several Mg alloys [50]	1.5[a] 2 – 2.5[b]	2.5 – 3[a] 1 – 2[b]	-2	Helium
Ti-6Al-4V alloy [51]	NS	0.8	NS	Helium
Stainless steel 304L [30]	4	3	0.2	Helium
Stainless steel 347 [30]	5	2	0.4	Helium
Stainless steel 304 [33]	1.25	0.75	NS	NS
Galvanized steel [34]	1.3	1	NS	Argon
Inconel 625 [40]	1.5	2	NS	NS
Zn and Sn [52]	1.6	1.5	5	NS
Stainless steel 440 and 416 [35]	Any combination of parameters that produces energy density in the range of 20.8 to 27.7 $J.mm^{-2}$			

NS: Not stated in the report. [a]For thinner plates (2.5 mm and 3.0 mm) [b]For thicker plates (5.0 mm and 8.0 mm)

The model presented by Dowden et al. [54] utilized this approach. They assigned a single temperature to vapor materials. Therefore, by obtaining the temperature distribution in each depth, a border between the vapored materials and the materials that are not vapored could be distinguished as the keyhole. The keyhole shape that they obtained was one that has a circular cross-section with a curved axis. Steen et al. [55] employed another approach to estimate the keyhole shape by the combination of a point heat source and a line heat source. They found a simple analytical form for the

temperature distribution and possible weld profiles were found numerically with specific choices for the strengths of the line and point sources, and specific locations for the point source. Comparison of the obtained profiles with the actual measured profile led to the profile that gave the best fit, leading to magnitudes of the line and point sources and the point source location.

Beck et al. [56] used the equations of continuity, motion, and energy to obtain the velocity and temperature fields and, hence, the keyhole shape and the maximum velocity of the melt flow at the sides of the keyhole. Kaplan [57] employed another technique to obtain the keyhole shape. He used the energy balance point-by-point through the substrate thickness to find the position of each point of the keyhole profile. This work showed that most of the laser beam heat was absorbed at the front wall of the keyhole rather than at the rear wall. Lampa et al. [58] simplified Kaplan's model and used it for calculating the penetration depth, by applying a correction factor for the material conductivity at the top of the melt-pool. The correction factor was calculated as 2.5, which makes the material more conductive.

Amara and Bendib [59] solved the Navier-Stokes equations for an incompressible fluid flow concentrated on the vapor pressure in the keyhole and confirmed that the vapor pressure works against forces, such as surface tension, that tend to close the keyhole opening. They used the ray-tracing code, which allows calculation of the energy deposited on the keyhole wall after each reflection of the laser beam. However, Fabbro et al. [60] showed that due to the high absorptivity of the front keyhole surface (60% to 80%), only one reflection of the laser beam is necessary for the modeling. Tenner et al. [61] used another method to estimate keyhole shape; that is, by relating it to the plasma

plume. Through experiments, they showed that the keyhole dynamic behavior is well correlated with the plume when a threshold laser power is reached, with this power being ~80% of the power required for full penetration (in this case, 2.5 kW). They concluded that at low laser powers, the stability of the keyhole is determined by the evaporation process in the keyhole. Fabbro [62] defined some regimes in laser welding and investigated keyhole shape, particularly, the keyhole front wall tilting, in the different regimes. They observed that at low welding speeds, the keyhole is more unstable, and the intensity, which is absorbed by the keyhole front wall, depends on the welding speed, not the intensity itself. Postaciogl et al. [63] estimated the shape of the surface of the weld as elevated or depressed. Kar and Mazumder [64] used mass conservation, momentum, and energy equations along with the heat transfer in the solid and vapor phases of the materials to predict the shape of the melt-pool by calculating the surface velocity and temperature distribution. They observed that the axial velocity at the beginning of the laser melting process is negligible, compared to velocities in other directions; however, after keyhole development, the dominant velocity is in the axial direction. They asserted that the moving speed of the solid-liquid interface is much higher than that of the liquid-vapor interface; in other words, the melt-pool depth increases more rapidly than does the keyhole depth.

2.3 Melt-Pool Thermodynamics

Heat transfer in the melt-pool during laser welding significantly affects the melt-pool shape, melt flow inside the melt-pool, and cooling rates of the melt-pool, and, thus, the quality and microstructure of the weld [65]. Since, in laser welding, dimensions of the melt-pool are on the order of mm and timescales are on the order of fractions of a second,

measuring the temperature profiles and cooling rates of each point is costly and time consuming. Thus, many of the studies reported on the thermodynamic characteristics of the melt-pool during laser welding are modeling works.

Mazumder and Steen [66] developed a three-dimensional quasi-steady heat transfer model of laser melting and compared their results using this model to those obtained from experiments. For simplicity, they assumed that there is no reflectivity at the material surface, where the temperature exceeds the boiling temperature of the material and the thermal properties of the material are constant and independent of temperature changes. Using this model, some process parameters were predicted, including temperature profile, maximum welding speed, HAZ width, thermal cycle at any location or speed, and the effect of supplementary heating or cooling, thickness, reflectivity, and thermal conductivity on melt-pool shape.

Goldak et al. [67] presented a more sophisticated model of weld heat sources that consisted of two combined ellipsoid shapes and is flexible enough to change the size and the shape of the heat source so that it could be used for shallow or deep penetration welding with various types of heat sources, such as arc, laser, and electron beam. They observed some differences between FEA and experimental results and suggested the reason to be due to neglecting the heat flow in the longitudinal direction. They found that the energy losses due to radiation and convection near the heat source are negligible.

Wang et al. [68] considered continuity, energy, and momentum equations and employed the volume-of-fluid method [69], which can be used to calculate the free surface shape of the keyhole, to solve a three-dimensional model of the temperature distribution. Using assumptions that the material properties are constant, and the fluid

flow is laminar and incompressible during the process, they found large temperature gradients in the front region of the keyhole. They claimed that the recoil pressure is the main driving force for the keyhole formation. Akbari et al. [70] used the same sets of equations and assumed the melt-pool surface to be flat and the fluid flow to be transient, laminar, and incompressible. They found that regardless of the welding speed, the temperature distribution decreased sharply at the laser beam center and then decreased slightly far away from the center of the laser beam. Frewin and Scott [71] considered temperature dependence of material properties and stated that the temperature profile is a function of absorptivity and laser beam energy distribution. De et al. [72] assumed a double ellipsoidal model for the heat source to present a two-dimensional conduction heat transfer model. They investigated the effect of varying the penetration depth and absorptivity on the exactness of the model results.

Vaporization is important in laser welding of alloys that contain one or more volatile constituents, this being because vaporization determines the thermodynamic characteristics of the melt-pool. Khan and DebRoy [45] concluded that the relative rates of vaporization of any two elements from the melt-pool was an indicator of melt-pool temperature, irrespective of the element pair selected. Increasing the laser power will increase the vaporization rate by increasing the temperature and the surface area of the melt-pool. Collur et al. [73] conducted several experiments to examine the role of gas phase mass transfer in the vaporization of alloying elements and modeled the role of plasma in the vaporization of alloying elements. The melt-pool is surrounded by a plasma during laser welding, allowing molten metal drops to vaporize, both in the presence and absence of plasma, isothermally. They found that under various shielding gas

environments, the rates of vaporization of alloying elements is independent of the flow rate and also of the nature of the shielding gas but is controlled by plasma-influenced intrinsic vaporization at the melt-pool surface.

To simplify modeling convection in the melt-pool, many researchers assumed that the thermal conductivity of the material is isotropic in that region [24,74,75]. In contrast, Safdar et al. [76] took into account anisotropic thermal conductivity and stated that the anisotropy-enhanced thermal conductivity approach leads to a more accurate result in the prediction of melt-pool temperature distribution.

There are many parameters that affect the shape of the melt-pool. One of them is Marangoni convection, also called surface-tension-driven convection, which is convection along an interface between two fluids due to a surface tension gradient [77]. Tsotridis et al. [78] presented a simplified model of the melt-pool considering Marangoni convection. For simplicity, they assumed that all the physical properties of the solid and the liquid are the same and they claimed that Marangoni flow dominated over buoyancy flow. Tsai and Kou [75] presented a two-dimensional heat transfer fluid flow model to describe Marangoni convection in the melt-pool that is dependent on the surface tension temperature coefficient. They asserted that when this parameter has a negative value, the Marangoni convection direction is radially outward, and the pool center is depressed but the outer part is elevated. However, a positive coefficient results in a convex melt-pool.

Limmaneevichitr and Kou [44] conducted experiments to investigate the effect of Marangoni convection on melt-pool shape. In this work, they used $NaNO_3$ and Ga for welding as these two materials have extremely high and low Prandtl number (Pr), respectively. $\mathrm{Pr} = \mathrm{C_p}\mu/\mathrm{k}$, where $\mathrm{C_p}$ is the specific heat, μ is the dynamic viscosity, and

k is the thermal conductivity. The Peclet number (Pe) is also important in determining the effect of Marangoni convection. Pe expresses the ratio of heat transport by convection to heat transport by conduction; that is, $\mathrm{Pe} = \mathrm{LV}/\alpha$, where L is the pool surface radius, V is the maximum outward surface velocity, and α is the thermal diffusivity. For the melt-pools of $NaNO_3$, a material with a high Pr, α is very low and V is high (strong Marangoni convection). Therefore, Pe is very high and heat transport in the melt-pool is dominated by Marangoni convection. Increasing the beam power increases Marangoni convection, the melt-pool size, V, L, and, hence, Pe. Experimental results showed that if a strong outward surface flow carries the heat outward to the melt-pool edge, it makes a concave pool bottom wide and flat. Reducing the beam diameter also increases Marangoni convection and Pe. The return flow penetrates the pool bottom close to the pool edge and turns the flat pool bottom to a convex one. Both the convex and flat pool bottoms indicate that Marangoni convection dominates over buoyancy convection, which is induced by gravity in the pools. On the other hand, for melt-pools of Ga, Pe is very low, and conduction dominates heat transport in the melt-pool. Heat is conducted downward and outward, and, thus, makes the pool bottom concave. Reducing the beam diameter makes the melt-pool more hemispherical, which confirms the domination of conduction over heat transport in the pool. Yang et al. [9] presented a model by combining continuity, momentum, and energy equations for liquid and solid phases and reported that the thermal properties of the material as well as Marangoni flow in the melt-pool could significantly influence melt-pool shape such that more Marangoni flow results in a wider and shallower melt-pool. Abderrazak et al. [10] utilized their experimental and finite volume simulation results obtained from Mg alloy specimens to assert that a negative

Marangoni effect, due to the absence of the surface-active agent in the alloy composition, makes the melt-pool wider and shallower.

The physical origin of the enhanced energy transfer from a laser to a material may be explained on the basis of two alternative mechanisms, namely, Fresnel absorption and inverse Bremsstrahlung (IB) absorption [79]. The Fresnel equation describes the behavior of light when moving between media of differing refractive indices. The absorption of light that the equations predict is known as Fresnel absorption. IB absorption is one of the important mechanisms for transferring energy from laser light to matter. In the very intense field used in a laser fusion program, processes involving multiphoton absorption and emission are very important [80]. There have been a number of different formalisms suggested for treating IB in intense fields [81] together with a few numerical calculations [81]. For example, Zhang et al. [82] presented a sandwich model to observe the keyhole in deep penetration laser welding, thus providing an effective way to analyze both Fresnel and IB absorption. By increasing the thickness of Al films between two glass pieces, higher densities of the keyhole plasma are achieved, leading to deep keyholes. By continuing to thicken the Al films, the aperture of the keyhole continues to widen. However, above a critical thickness, the depth of the keyhole reduces (in Al films, this critical thickness is 0.3 mm). This is due to the excess density of keyhole plasma, which prevents the transmission of the laser beam to the keyhole. The density of the keyhole plasma creates similar effects on changes in welding depth compared to keyhole depth. Cheng et al. [79] computed the laser intensity absorbed on the keyhole wall using Fresnel and IB absorption of the keyhole plasma. They concluded that IB absorption of keyhole plasma plays a more important role than does Fresnel absorption. They asserted that the

temperature of the keyhole plasma decreases from the top to the bottom of the keyhole and decreases from the center to the edge of the keyhole. , Tan et al. [83] found that, almost invariably, the maximum temperature in the keyhole wall is located at the bottom of the keyhole.

2.4 Melt-Pool Fluid Dynamics

In order to obtain a high-quality laser-welded metal product, it is necessary to prevent defects before they occur. When a metal is in the liquid state, the probability of collapsing of the melt-pool or its partial penetration is high. Therefore, the dynamics of the melt-pool and the fluid flow patterns are important.

Zacharia et al. [84] proposed that surface active elements may alter the flow field in the melt-pool and, hence, affect weld penetration. They showed that a combination of the concentration of the surface active elements and the temperature distribution has an important role in determining weld penetration. It was also shown that the melt-pool flow can be simulated more realistically considering not only the coefficient of surface tension as a function of temperature but also the concentration of the surface active elements. In laser welding (unlike gas tungsten arc welding [85,86]), the latter factor makes the temperature coefficient of surface tension largely negative, causing the flow to be radially outward at the melt-pool surface. This flow transfers the heat out from the center of the melt-pool and makes the pool shallow.

Semak et al. [87] investigated the dynamics of the melt-pool by conducting experiments using three different types of pulses: a single 20- or 30-ms pulse, continuous wave pulse, and repetitive 20-ms pulses. They observed that the vaporization pressure exceeds surface tension and hydraulic pressure in the melt-pool, creating a high-velocity

melt flow and, thus, a melt crown around the keyhole at the melt-pool edge. Also, significant variations in the shape of the keyhole opening were observed, which were attributed to the instability of the vapor pressure. Semak et al. [88] presented a model to simulate the fluid flow in the melt-pool during pulsed laser welding. In a later contribution, they modified their simulation to include the effect of surface tension [89]. They asserted that the effect of this force could be an ejection or a retention, depending on the distribution of the beam intensity.

Cho et al. [90] simulated the fluid flow in the melt-pool during the transition from conduction laser spot welding to keyhole laser spot welding and showed an upward and downward oscillation in the fluid flow in the center of the melt-pool in the direction of normal to the surface. They attributed this oscillation to interaction of competing pressures, including recoil pressure and surface tension pressure. Using a sandwich model, Zhang et al. [91] observed the dynamics of the keyhole and showed that the hydrodynamics at the keyhole wall has a dominant effect on defects in the weld. Geiger et al. [92] used continuity, heat conduction, and the Navier–Stokes equations to show how pores form at high welding speeds (such as 12 m min^{-1}). A higher welding speed results in a higher pressure at the keyhole front and, thus, higher velocities of melt flow around the keyhole, which lead to a depression outside the keyhole. A combination of this phenomenon with the surface tension leads to formation of pores.

The coupling between the melt-pool and the keyhole is complicated. It has been shown that the sideways liquid displacement around the front keyhole wall is the main process for generating high velocities of the fluid that enter the melt-pool [25,93]. Basu and DebRoy [94] found a threshold for the melt-pool surface temperature above which

the vaporization-induced recoil pressure overcomes the surface tension pressure, causing an outward flow to the sides [95]. The recoil pressure is one of the three main mechanisms responsible for expelling melt from the keyhole. The other two, which are particularly important at higher melt surface temperatures, are melt evaporation and the shielding gas interaction with molten metal. The melt flow generated by the recoil pressure has a direction in which the recoil pressure gradient is the highest. Therefore, in laser welding, the melt flow is ejected by the recoil pressure to the sides of the melt-pool [25]. Fabbro et al. [41] discussed the effects of the interaction between the vapor, which is generated by the ablation process occurring on the front keyhole wall, and the surrounding melt-pool. They showed that an efficient control of the dynamics of melt-pool can be achieved using a side gas jet, which can be localized in the front or the rear position. This gas jet decouples the interaction zone inside the keyhole and the melt-pool. Therefore, the melt-pool flow can be well stabilized, resulting in a high-quality weld and improved penetration at low welding speeds. Amara and Fabbro [96] modelled the fluid flow in the melt-pool, considering the interaction between the vapor and the liquid and between the liquid and the air. Fabbro et al. [97] showed that the escaping vapor, which is generated in the keyhole, creates friction forces, which, in turn, play an important role in fluid flow in the melt-pool. Experiments [98] showed that these forces generate humping instabilities on the melt-pool above a critical welding speed. Amara et al. [99] considered the friction effects of the vapor flow with the liquid walls as an important factor to numerically solve the hydrodynamic equations, obtaining the shear stress distribution on the keyhole walls. Further investigations [100] lead to three-dimensional calculations of the molten metal flow velocity induced by the friction phenomenon and the thickness of

the boundary layer. The friction force, which is induced on the melt-pool wall, results in a drag force expelling the flow towards the surface. The other main driving forces for the molten material in the melt-pool result from surface tension, recoil pressure, and buoyancy forces [5,87,96]. By solving a combination of the Navier-Stokes, energy conservation, and ideal gas equations, using the finite volume method, it was confirmed that using a gas jet during deep penetration laser welding results in better weld joints because the melt flow in the melt-pool is enhanced.

Insufficient metal flow in the melt-pool may be due to excessive welding speed or incorrect laser power, which leads to hump formation, a phenomenon that produces variation in weld penetration [101]. Once the hump starts to be solidified, further melt flows upwards and resolidifies, causing the hump to grow [102]. The travel angle between the laser beam and the welding direction has been found to affect the onset of humping. Forehand welding has been shown to suppress hump formation to higher welding speeds [103,104]. Gratzke et al. [105] defined a critical ratio of the width to the length of the melt-pool, which determined the likelihood of hump formation, such that maximizing this ratio during welding decreases the possibility of hump formation. Another way of reducing humping defects in laser welding is by using a tandem dual beam [106]. When the beams are far apart, the second beam suppresses the humps formed by the first one and when the beams are close, the following beam stabilizes the keyhole, thereby preventing hump formation after the leading beam. According to Beck et al. [107], any reduction in flow velocities in the rearward direction avoids hump formation. Kern et al. [108] used this concept in their experiments of CO_2 laser welding of steel by applying a magnetic field transverse to the welding direction, thus altering the

melt flow profile within the melt-pool and suppressing hump formation. Matsunawa and Semak [109] simulated the keyhole during high speed laser welding and found that hump formation frequency was increased with increasing welding speed. However, Kawahito et al. [110] defined a process window of welding speed and laser beam diameter, in which humping occurred over a particular range of laser power density. In a later work [111], these authors found hump formation to be caused by several dynamic and static factors, including flow velocity, surface tension, solidification, and melt volume. They asserted that hump formation could be avoided in fully penetrated welds by decreasing melt volume so that the formation of the convex surface at the rear end of the melt-pool was suppressed. According to the model of Matsunawa and Semak [109], when the component of the keyhole velocity that is parallel to the surface was higher than the beam translation speed, the instability of the keyhole resulted in hump formation on the weld surface. A hump may also form on the keyhole wall surface when the upper part of the keyhole wall moves away from the laser beam axis and the lower part continues to move towards the axis. Ilar et al. [112] introduced root humping, which was different from top surface humping, being formed due to a gravity effect. Root humping was initiated by increase in the amount of material flowing in the melt-pool that originated from the bottom of the melt-pool. Amara and Fabbro [113] presented a 3D model based on the numerical resolution of the fluid flow and the heat transfer equations showing hump formation at high welding speeds in deep-penetration laser welding. Pang et al. [114] found significant differences between melt-pool dynamics of an unstable keyhole and a stable one, and that by controlling the welding speed and surface tension they could prevent the formation of humps on the keyhole wall, thus reducing keyhole instability.

They stated that under certain low-heat-input welding conditions, collapse of the keyhole wall could be avoided.

Ki et al. [46,115] presented a three-dimensional laser keyhole welding model and used the Navier-Stokes and energy equations to simulate the movements of the liquid-vapor interface and the solid-liquid interface as well as the heat transfer. In addition, they simulated the transition from conduction-mode welding to keyhole-mode welding. For the sake of simplicity, they extrapolated material properties at high temperatures from values obtained at lower temperature. They did not take plasma into account, assumed the gas was incompressible, and neglected re-condensation of the vapor after interacting with the hole surface. They confirmed that one of the main differences between the two types of laser welding (keyhole-mode and conduction-mode) is the recoil pressure, which is generated by evaporation during the laser keyhole welding. There is a fluctuation in the amount of laser energy absorbed in the keyhole, which, in turn, leads to fluctuation of the shape of the keyhole and this fluctuation affects the recoil pressure and the flow field in the melt-pool. Their model also allows prediction of microstructure and property evolution in laser-welded joints. Chakraborty et al. [74] developed a three-dimensional model of laser welding using conservation of mass, momentum, and energy equations to evaluate the influence of turbulence in the melt-pool on the process parameters and found that the velocity and temperature gradients are smaller in the turbulent melt-pool, a finding that agrees with the experimental results.

2.5 Weld Microstructure

A high cooling rate typically is experienced by the melt-pool immediately after laser welding. Solidification takes place usually in a few tens of milliseconds and metastable microstructures are produced that influence the final mechanical properties of the weld. Therefore, microstructure characterization is vital in the determination of weld quality [116,117]. Solidification of molten weld metal depends on the kinetics of liquid-solid interface. Kou [118] described this by using values of the thermal gradient (G) (usually, they are in range of 100-1000 K m^{-1}) and the travel speed of the liquid-solid interface (R) (usually, they are in the range of 10 -103 m s^{-1}). Kou identified four possible modes of solidification: 1) planar (high G and low R), 2) cellular, 3) columnar dendritic, and 4) equaixed dendritic (low G and high R) (Figure 3). The ratio of G to R determines the mode of solidification. Kou showed that the product of G and R indicated the cooling rate, so these two parameters determined the fineness of the solidified microstructure (Figure 3). Kou also noted that solidification of the melt-pool could take place in one of two ways, namely, a) epitaxial and b) non-epitaxial, depending on the composition of the weld metal.

The microstructure of rapidly-solidified laser-molten Al-4.5 wt % Cu alloyed surfaces was studied and melted regions were found to resolidify epitaxially onto unmolten crystalline substrates [119]. Solidification proceeded as follows: a plane front mode, then cellular, and, finally, continuing in a columnar competitive manner. The major impact of the rapid solidification was a refinement of the surface microstructure. Kou [118] found that melt convection was not sufficiently vigorous to produce a homogeneous melt. Evidence of epitaxial resolidification was also found in a nickel-

based superalloy (Udimet 700) when laser melted [120]. This face-centered-cubic (fcc) material showed a strong preference for dendritic growth along (100) directions. The consequence of rapid cooling rate was evident by fine dendritic regrowth, with a spacing of ~2.5 mm. The dendrites grew nearly parallel to the local direction of maximum heat flow [120].

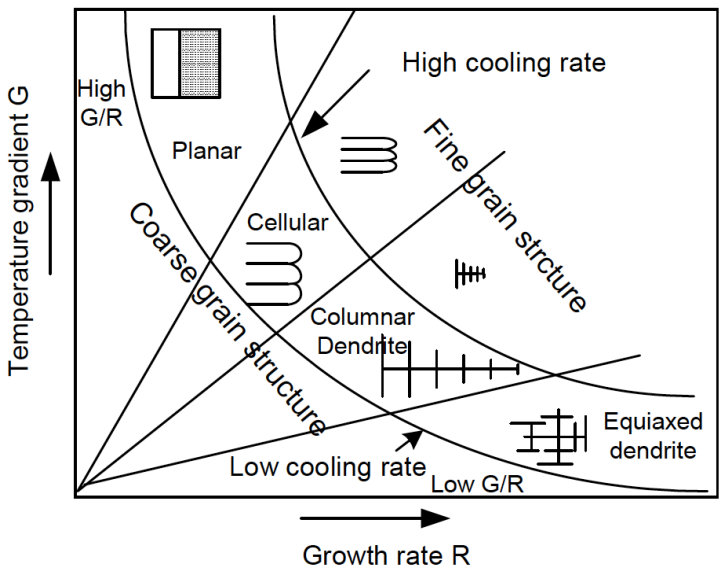

Figure 3. Influence of G & R on mode of solidification and grain structure [118]

Many researchers have investigated the microstructures of welds in laser welding of stainless steels and other ferrous alloys. Zambon and Bonollo [121] characterized the microstructure of weld beads and HAZ of austenite and duplex stainless steels. They stated that high cooling rates might result in formation of non-equilibrium microstructures, which contain larger amounts of δ-ferrite in duplex steels, than predicted both by the Fe-Ni-Cr pseudo-binary phase diagram and by the Schaeffier diagram. They concluded that non-equilibrium microstructures decreased the corrosion resistance of the welded joints. The rate at which a ferrous metal/alloy weldment cools significantly influences the ferrite morphology and distribution [122]. Zacharia et al. [8] presented a

model to obtain the complex temperature distribution and the cooling rates and showed that in laser pulsed welding, at low speeds, the weld metal remains molten, even during time when the laser beam is not being applied. They confirmed that the microstructure is dependent on the cooling rates and ranged from duplex austenite + ferrite to fully austenitic or fully ferritic. These authors conducted another study in two parts (analytical and experimental) [84,123] and by employing the equations of momentum, energy, and mass continuity concluded that the dominant force for the fluid flow is the surface tension gradient. They found the cooling rates at the solidification temperature to be the highest at the edge of the melt-pool rather than at the bottom or top center of it. In another study by Zacharia et al. [84], their observed microstructural evaluation of laser welded 304 stainless steel fusion zones revealed a fine dispersion of chromium oxide inclusions and a continuous oxide layer. The observed microstructures were sensitive to the cooling rates, with decrease in the cooling rate resulting in a coarser solidification substructure with a widely spaced ferrite network. The rapid solidification of the laser beam welded metal resulted in a fully austenitic microstructure with a fine solidification substructure. Lippold [124] determined the susceptibility of weld solidification cracking in austenitic stainless steels during pulsed-laser welding. The author found that a shift in weld solidification behavior occurred under rapid solidification conditions. Solidification as primary austenite was found to be most detrimental and cracking depended mainly on composition, whereas pulsed-laser welding process parameters had only a small influence. A solidification model was discussed that related the transition in primary solidification from ferrite to austenite to dendrite tip undercooling at high solidification growth rates.

Lippold [124] also found out that the available predictive microstructure diagrams and solidification models (the Suutala weldability diagram [125] and the Welding Research Council constitution diagram [126]) are not accurate under rapid solidification conditions, which happens during pulsed-laser welding of stainless steels. Therefore, regarding rapid solidification, they proposed a predictive diagram for weld solidification cracking susceptibility; a solidification model relating the transition in primary solidification from ferrite to austenite to dendrite tip undercooling; and a microstructural map for austenitic stainless steel welds. Brooks et al. [127] studied high energy stainless steel welds and concluded that minimal solid-state diffusion occurs during the solidification and cooling of primary austenite solidified welds, whereas structures which solidify as ferrite may become almost completely homogenized as a result of diffusion. A nearly segregation-free, single-phase austenite structure, which appears to be unique to the rapid solidification velocities and cooling rates of high-energy welds, was also observed. They suggested that this structure was a product of a marked phase transformation in which ferrite was transformed to austenite.

Recently, marked transformations were identified in the selective electron beam melting of Ti-6Al-4V. Thus, Lu et al. [128] concluded that the β (body-centered-cubic (bcc)) to α_m (hexagonal close-packed) transformation led to the formation of a variety of patch-shaped massive grains, including large grain-boundary-crossing grains with misorientations being as much as 30°. Marked transformations have been identified in laser welding of stainless steels where the influence of composition and cooling rate on the solid-state transformation to γ-austenite was studied [129]. An analysis by D'amato et al. [130] showed that grain refinement at the weld area occurred and that δ-ferrite was

present in the as-welded samples. The authors also concluded that the welds solidified by primary ferrite solidification with some chromium carbide precipitates in the weld area. The microstructure of the weld metal of a duplex stainless steel made with Nd:YAG pulsed laser was studied by Mirakhorli et al [131]. They found the weld microstructure to be composed of two distinct zones: 1) at high overlapping factors, an array of continuous axial grains at the weld centerline was formed and 2) at low overlapping factors, in the zone of higher cooling rate, a higher percentage of ferrite was transformed to austenite. They concluded that the high cooling rates involved in pulsed laser welding led to low overlapping, thus, limiting the ferrite-to-austenite transformation to the grain boundaries only.

Concerning other ferrous-based alloys, Babu et al. [132] studied the primary solidification phase of Fe-C-Al-Mn steel welds under rapid- and slow-cooling rates. They found nonequilibrium austenite solidification during rapid cooling in contrast to equilibrium δ-ferrite solidification that occurs under slow cooling conditions. Nakao et al. [133] studied the effects of rapid solidification by CO_2 laser surface melting of Fe-Cr-Ni ternary alloys. They found rod-like eutectic microstructures that first increased and then decreased with increasing cooling rate. So-called ‘massively solidified structures’ were formed when the cooling rate exceeded a critical value, which, in turn, is markedly influenced by the chemical composition of the alloy. Microstructurally, the δ-ferrite contents were influenced by the cooling rate.

El-Batahgy [30] evaluated fusion zone shape and solidification structure as a function of laser welding parameters. He found that the type of the fusion zone microstructure does not depend on change in heat input and it is always austenite, with

~2-3 vol.% ferrite. However, a finer solidification structure could be obtained by lowering the heat input.

Mohanty and Mazumder [134] observed the solidification behavior of the melt-pool during laser melting and stated that the keyhole shape influences the flow pattern in the melt-pool, and that may change the microstructure characteristics. Even under constant scanning speed conditions, they observed an unsteady motion of the solid-liquid interface, resulting in fluctuation in growth rates and in thermal fields, which makes a solidified zone remelt and resolidify. This leads to discrete structural bands in the solidified bead. Using time-resolved x-ray diffraction, David et al. [135] analyzed the instabilities at the solid-liquid interface and confirmed that on slowly cooled spot welds, the equilibrium primary solidification phase is δ-ferrite but, in rapid solidification, primary austenite was observed. Using momentum, continuity, and energy equations for incompressible, laminar, and Newtonian flow, Roy et al. [136] developed a model to simulate the temperature and velocity fields during pulsed laser welding and verified it using experimental results [137]. The computed cooling rates and weld bead dimensions were consistent with experimental results. However, the ratio of the temperature gradient to the solidification rate indicated that conditions for plane front solidification of stainless steel were not satisfied for the pulsed laser welding parameters. Therefore, these workers suggested that numerical calculations could improve understanding of solidification during pulsed laser welding.

The role of the shape of the melt-pool on weld microstructure has been studied by Rappaz et al. [138], who created a three-dimensional reconstruction of electron beam weld pool shape and measured dendrite spacing as a function of growth velocity. The

dendrites were found to grow parallel to three <100> crystallographic directions, which indicated that dendrites that occurred from the single crystal portion remained solid during the welding process. The weld microstructure contained dendrites that were only slightly branched and had a cell-like structure. David and Vitek [139] were the first one to observe the effect of cooling rate on the modification of microstructure from austenite + ferrite to fully austenitic structure in austenitic stainless steels. They determined this was due to a large undercooling encountered by the liquid under rapid cooling conditions encountered during electron and laser beam welding. Here, two phenomena occur as solidification growth velocities increase: 1) partitioning of solute between solid and liquid and 2) nonequilibrium phase formation. Kelly et al. [140] made similar observations in their study of rapid solidification of 303 stainless steel droplets and found that solute elements were more completely trapped in the bcc structures. The crystal-to-liquid nucleation temperatures showed that bcc nucleation was favored at large liquid super cooling. More recently, Siefert and David [141] studied the weldability of austenitic stainless steels and attributed changes in microstructure to large undercooling in the liquid and partitionless solidification.

Hu and Richardson [142] evaluated the cracking behavior in welds of high strength Al alloys and found out that cracking happens when the fusion zone is in the semi-solid state and it is related to the temperature distribution, which is elongated in the welding direction. These workers confirmed that this temperature distribution during the cooling phase causes a transverse tensile strain in the fusion zone. To avoid cracking, they suggested three solutions: decrease scanning speed in order to decrease the longitudinal strain; alter the composition in the fusion zone to improve the strength and ductility of the

weld; and add a heating or cooling source to modify the thermal history of the fusion zone in the semi-solid temperature range. Rai et al. [143] stated that the values of solidification parameters at the trailing edge of melt-pool depend on the physical properties of the material, with some very influential ones being thermal diffusivity, absorption coefficient, melting temperature, and boiling temperature. Materials with a lower thermal conductivity are expected to have a fusion zone, which is spread near the top. A number of workers have combined various existing models that consider multiple beam reflections in the keyhole to calculate temperature and velocity fields, weld geometry, and solidification parameters during laser welding of tantalum, Ti–6Al–4V, 304L stainless steel, and vanadium [25,54,57,63,66,144–154]. In addition, these researchers used a turbulence model to calculate the thermal conductivity and effective viscosity in the melt-pool. They confirmed that the main mechanism of heat transfer for all four materials was convective heat transfer that depends on the thermal diffusivity and temperature coefficient of surface tension. The smallest melt-pool was observed in tantalum, a consequence of its high boiling temperature, melting temperature, and solid-state thermal diffusivity.

Ghaini et al. [155] conducted experiments to examine the influence of process parameters on microstructure and hardness during overlap laser bead-on-plate spot welding. They defined the effective peak power density that takes into account the effect of overlapping. They presented two approaches for full penetration welding: high peak power densities with high travel speeds that have low overlapping and medium peak power densities with medium travel speeds. In the first approach, due to the higher cooling rates and the nature of the thermal effects of the next pulse on the previous weld

spot, the weld metal has high hardness and displayed large hardness variation while opposite results were obtained when the latter approach was used. Combining these two approaches and having the optimum power density with overlapping factor enhances prediction of the weld microstructure and hardness. In a bid to understand the hot cracking phenomena in laser overlap spot welding of Al alloys, Ghaini et al. [156] investigated the interdependency of solidification cracking in the weld metal with liquation cracking in the base metal and concluded that the liquation cracks act as initiation sites for solidification cracks. However, at low laser pulse energies, liquation grain boundary cracks occur less frequently, and solidification cracks initiate independently from the fusion lines between subsequent weld spots. These workers stated that cracks could only occur when the rate of induced strains was greater than the rate of backfilling.

Kadoi et al. [156] studied the influence of welding speed on solidification cracking susceptibility in laser welding of Type 310S stainless steel and found that an increase in welding speed decreases the critical strain for solidification crack initiation. They suggested the reason to be the distribution morphology of the residual liquid at the weld bead center that depends on the microstructure at the rear of the melt-pool. Tan and Shin [157] presented a multi-scale model of solidification and microstructure development during laser keyhole welding of austenite stainless steel. On a macro-scale, a model was utilized to predict the fluid flow, thermal history, and solidification conditions of the melt-pool, which is influenced by the welding speed. The meso-scale model was used to predict the grain growth in welds and the macro-scale model was developed to simulate the dendrite growth. These workers observed that grain growth direction varies according

to the melt-pool complex shape. The maximum temperature gradient controls the dendrite orientation while the dendrite morphology is influenced by cooling rate. Increasing the cooling rate reduces the spacing of the primary dendrite arms and suppresses the growth of the secondary dendrite arms. A summary of microstructural development as a function of cooling rate is presented in Table 3.

Table 3. Effect of solidification rate on microstructure of metals and alloys.

Cooling rate ($K.s^{-1)}$	10^5	10^4	10^3	10^2	10^1
Microstructural features	Amorphous	Fine grains	Fine dendrites	Martensite [158]	Dendrites [135]
Comments	Metastable	Nonequilibrium	None	None	Follows equilibrium phase diagram

2.6 Weld Porosity

Porosity is especially important in Mg and Al alloys and researchers have conducted several experiments on these two metal alloys in order to determine the porosity characteristics of the melt-pool in keyhole laser welding process. In recent years, Mg and its alloys have gained increasing interest in industry, mainly due to their low density [159]. Furthermore, liquid Mg has a much larger solubility of hydrogen than solid Mg [160]. Therefore, hydrogen porosity is an important concern for the welding of Mg alloys [161]. Galun et al. [50] observed a large number of pores in welds of high-pressure die-cast alloys, such as AZ 91 and AM 60, due to escaping gas entrapped in the material during the die casting process. Through experiments, Pastor et al. [42] showed that overfill on AM60B alloy weld was caused by the displacement of liquid metal by the

pores. Therefore, any parameter that reduces porosity in the melt-pool decreases overfill. They showed that expansion of the initial pores in the base metal is the most important mechanism of porosity formation. For this alloy, Zhao and DebRoy [48] came to the same conclusion. They observed that coalescence and expansion of the initial pores, due to heating and reduction of internal pressure, play a key role in increasing porosity in the fusion zone. They asserted that a balance between surface tension pressure and vapor pressure determines the stability of the keyhole. However, pore formation during laser welding of alloy AM60B does not depend on the keyhole instability.

The 2000, 5000, and 6000 series Al alloys are used in many automotive applications, such as body panels, because of the combination of high specific strength, good crash-worthiness, and excellent corrosion resistance [162]. These attributes make laser beam welding an attractive joining process for such applications [163,164]. However, porosity, hot cracking, and weld metal composition change are major concerns in the welding of Al alloys [165]. The formation of the keyhole leads to a deep-penetration weld and a hole created in a liquid is unstable by its nature, causing the formation of porosity in the weld metal. Since porosity is one of the serious problems in very high-power laser welding, Matsunawa et al. [5] observed that in pulsed laser spot welding of Al alloys, the keyhole opening collapses within one tenth of the time that the melt-pool solidifies and a large cavity forms at the bottom of the keyhole. Fluctuation of the keyhole opening was less unstable in continuous-wave laser than that in pulsed laser. However, the shape and the size of the melt-pool changes with time. By observing the keyhole using optical and x-ray methods, they found that a deep depression is formed on the rear wall of the keyhole, moving from the top to the bottom periodically. They also observed a large bubble in the

melt-pool, resulting in the formation of pores. The bubble is composed of evaporated metal vapor and entrained shielding gas. These workers observed two types of porosity in laser welded parts: porosity induced by hydrogen and a large cavity caused by the fluctuation of the keyhole by intense evaporation of the metal. They also found two effective methods for reducing porosity in Al alloys: use of a low-dew-point shielding gas below 250 °C and removal of the oxide layer from the surface. The cavity formation in pulsed laser spot welding can be suppressed by adding a proper tailing pulse to avoid collapse of the keyhole opening. In continuous-wave laser welding of Al alloys, Matsunawa et al. [5] found N_2 shielding to be effective in suppressing large pores. This is because of the formation of aluminum nitride (AlN) on the liquid surface, which suppresses the perturbation of both the melt-pool and the keyhole. Moreover, entrained N_2 in the keyhole is consumed, forming AlN; therefore, the number of shielding gas-filled pores is reduced.

Mizutani et al. [52] irradiated a laser beam to the surface of a solid metal and to an already molten metal and observed that the keyhole initiates much earlier in the molten metal than it does in the solid metal. They presented a simplified numerical calculation demonstrating that the formation of bubbles is influenced by surface tension. They showed that the deepest location of the keyhole tends to collapse more easily. Therefore, formation of the bubbles in deep and narrow keyholes is expected. Courtois et al. [166] confirmed that in pulsed laser welding with a high laser power, when the laser beam is not being applied, the keyhole wall collapses and entraps some gas, creating bubbles, which, in turn, lead to pores. In addition to resolidification microstructures, defects, such as voids, form. Kim and Weinman [167] irradiated samples of 2024-T3-51 Al with a

pulsed Nd-glass 1.06 μm laser at an incident energy density of 440 J cm^{-2}, with and without a protective helium gas flow over the surface. A cooling rate of 105 to 107 K s^{-1} was estimated. They found that many elongated and small voids formed at the melt-matrix interface due to a combination of shrinkage and gas expulsion and that void presence reduced fracture resistance. These authors determined that gas ejection in the melt affected dendrites growth patterns.

In a computational fluid dynamics study, Zhao et al. [168] considered the existence of the three phases of the material and employed continuity, energy, and momentum equations. They extrapolated the material properties for high temperatures and assumed the fluid to be Newtonian and the flow to be laminar and incompressible. They reported the main cause of porosity defect to be the oscillation of the keyhole depth, while the depth of the melt-pool is steady. The keyhole oscillates due to the opposition of the dynamic forces and the melt flow. Courtois et al. [169] confirmed the findings by Zhao et al. by calculating the laser reflections in the keyhole during laser welding. They used Maxwell equations, coupled with continuity, energy, and momentum equations, to develop a model for calculating the laser reflections in the process. Moreover, they showed that the shear stress at the keyhole surface has a marked influence on the melt-pool dynamics. Cho et al. [170] simplified the laser welding process by assuming a void region for the region of gas or plasma. They modified the laser beam model they used in their previous work [171], in which an infinitesimal point was considered as the focal point on the surface. In the later model, the focal point was calculated, and the reflections were taken into account. Using mass, energy conservation, and the Navier-Stokes equations, they considered buoyancy and Marangoni forces as well as recoil pressure.

They confirmed that using a beam with a Gaussian profile could lead to reliable results and they observed that consideration of the shear stress on the keyhole wall, which is generated by the metal vapor, does not play a significant role in the shape of the HAZ.

2.7 Summary

The present work is a state-of-the-art literature review on the properties of the melt-pool in laser welding and the relationship between welding process parameters and melt-pool characteristics. The characteristics considered were geometry, thermodynamics, fluid dynamics, microstructure, and porosity. Furthermore, the optimum laser welding parameters for a selection of metals and alloys are presented in this review. Several experimental studies have been conducted on melt-pool characterization in laser welding. However, direct experimental observation of melt-pool characteristics remains a challenge because of the high temperatures in the melt-pool and the difficulty of monitoring the metal vapor in the keyhole. Thus, there is scope for developing more sophisticated experimental techniques. Several models, having varying degrees of sophistication, have been used. Four common shortcomings of many of these models are identified. First, simplifications were used; for instance, the temperature dependence of the thermophysical properties of materials is either neglected or extrapolated for high temperatures. Second, the influence of consideration of the three heat transfer modes, namely, conduction, convection, and radiation, in both the radial and the axial directions in the melt-pool, has received little attention. Third, fluid flow in the melt-pool is considered incompressible and laminar. Fourth, the agreement between model and experimental results is not very good. These observations suggest several areas for future study. For example, models may be improved by taking into account the compressibility

of the vapor in the keyhole and the turbulence of the fluid flow in the melt-pool. In terms of models, multi-scale models, which integrate nanostructures and microstructures of materials with multi-physics macro-scale models, are needed. Additionally, more experimental results are needed on a wide collection of alloys and welding parameters, yielding results that would enhance verification and validation of models.

Acknowledgments

The authors thank the FedEx Institute of Technology, The University of Memphis, Memphis, TN, USA, for partial funding of this work under the DRONES cluster.

References

[1] Lasers — high-power and low-power, Opt. Laser Technol. 3 (1971) 181–185. doi:10.1016/0030-3992(71)90086-7.

[2] J. Mazumder, Laser welding: state of the art review, JOM. (1982).

[3] M.S. Brown, C.B. Arnold, Fundamentals of Laser-Material Interaction and Application to Multiscale Surface Modification, Laser Precis. Microfabr. 135 (2010) 91–120. doi:10.1007/978-3-642-10523-4__4.

[4] J. Mazumder, W.M. Steen, Heat transfer model for cw laser material processing, J. Appl. Phys. 51 (1980) 941–947. doi:10.1063/1.327672.

[5] A. Matsunawa, J.D. Kim, N. Seto, M. Mizutani, Dynamics of keyhole and molten pool in laser welding, J. Laser Appl. (1998).

[6] P. Okon, G. Dearden, K. Watkins, M. Sharp, P. French, Laser Welding of Aluminium Alloy 5083, 21st Int. Congr. Appl. Lasers Electro-Optics. 53 (2002) 1689–1699. doi:10.1017/CBO9781107415324.004.

[7] T. Chande, J. Mazumder, Estimating effects of processing conditions and variable properties upon pool shape, cooling rates, and absorption coefficient in laser welding, J. Appl. Phys. 56 (1984) 1981–1986. doi:10.1063/1.334231.

[8] T. Zacharia, S.A. David, J.M. Vitek, T. Debroy, Heat Transfer during Nd-Yag Pulsed Laser Welding and Its Effect on Solidification Structure of Austenitic Stainless Steels, Metall. Trans. A. 20A (1989) 957–967.

[9] L.X. Yang, X.F. Peng, B.X. Wang, Numerical modeling and experimental investigation on the characteristics of molten pool during laser processing, Int. J. Heat Mass Transf. 44 (2001) 4465–4473. doi:10.1016/S0017-9310(01)00086-2.

[10] K. Abderrazak, S. Bannour, H. Mhiri, G. Lepalec, M. Autric, Numerical and experimental study of molten pool formation during continuous laser welding of AZ91 magnesium alloy, Comput. Mater. Sci. 44 (2009) 858–866.

doi:10.1016/j.commatsci.2008.06.002.

[11] M. Dhahri, J.E. Masse, J.F. Mathieu, G. Barreau, M. Autric, Laser welding of AZ91 and WE43 magnesium alloys for automotive and aerospace industries, Adv. Eng. Mater. 3 (2001) 504–507. doi:10.1002/1527-2648(200107)3:7<504::AID-ADEM504>3.0.CO;2-3.

[12] K.Y. Benyounis, A.G. Olabi, M.S.J. Hashmi, Effect of laser welding parameters on the heat input and weld-bead profile, J. Mater. Process. Technol. 164–165 (2005) 978–985. doi:10.1016/j.jmatprotec.2005.02.060.

[13] R. Morgan, C.J. Sutcliffe, W. O'neill, Density analysis of direct metal laser re-melted 316L stainless steel cubic primitives, J. Mater. Sci. 39 (2004) 1195–1205.

[14] W.M. Steen, Laser Material Processing, First edit, Springer Verlag, London, New York, 1991.

[15] E. Locke, E.D. Hoag, R. Hella, Deep penetration welding with high-power CO2 lasers, Quantum Electron. IEEE J. 8 (1972) 132–135. doi:10.1109/JQE.1972.1076932.

[16] J. Mazumder, An Overview of Melt Dynamics in Laser Processing, in: E.-W. Kreutz, A. Quenzer, D. Schuoecker (Eds.), International Society for Optics and Photonics, 1987: pp. 228–241. doi:10.1117/12.941246.

[17] S.A. David, J.M. Vitek, Correlation between solidification parameters and weld microstructures, Int. Mater. Rev. 34 (1989) 213–245. doi:10.1179/imr.1989.34.1.213.

[18] X. Cao, W. Wallace, C. Poon, Research and progress in laser welding of wrought aluminum alloys. I. Laser welding processes, Mater. Manuf. Process. (2003).

[19] X. Cao, W. Wallace, J.P. Immarigeon, Research and progress in laser welding of wrought aluminum alloys. II. Metallurgical microstructures, defects, and mechanical properties, Mater. Manuf. Process. (2003).

[20] J. Shao, Y. Yan, Review of techniques for on-line monitoring and inspection of laser welding, J. Phys. Conf. Ser. 15 (2005) 101–107. doi:10.1088/1742-6596/15/1/017.

[21] X. Cao, M. Jahazi, J.P. Immarigeon, W. Wallace, A review of laser welding techniques for magnesium alloys, J. Mater. (2006).

[22] L. Liu, D. Ren, F. Liu, A review of dissimilar welding techniques for magnesium alloys to aluminum alloys, Materials (Basel). 7 (2014) 3735–3757. doi:10.3390/ma7053735.

[23] W.M. Steen, Laser surface treatment, Laser Mater. Process. (1991).

[24] C. Chan, J. Mazumder, M.M. Chen, A two-dimensional transient model for convection in laser melted pool, Metall. Trans. A. 15 (1984) 2175–2184. doi:10.1007/BF02647100.

[25] V. V. Semak, A. Matsunawa, The role of recoil pressure in energy balance during laser materials processing, J. Phys. D. Appl. Phys. (1997).

[26] A.P. Mackwood, R.C. Crafer, Thermal modelling of laser welding and related processes: a literature review, Opt. Laser Technol. 37 (2005) 99–115. doi:10.1016/j.optlastec.2004.02.017.

[27] A. Yaghi, A.A. Becker, Weld simulation using finite element methods, (2005).

[28] X. He, Finite element analysis of laser welding: a state of art review, Mater. Manuf. Process. (2012).

[29] J. Svenungsson, I. Choquet, A.F.H. Kaplan, Laser Welding Process - A Review of Keyhole Welding Modelling, Phys. Procedia. 78 (2015) 182–191. doi:10.1016/j.phpro.2015.11.042.

[30] A.M. El-Batahgy, Effect of laser welding parameters on fusion zone shape and solidification structure of austenitic stainless steels, Mater. Lett. 32 (1997) 155–163. doi:10.1016/S0167-577X(97)00023-2.

[31] K.N. Lankalapalli, J.F. Tu, M. Gartner, A model for estimating penetration depth of laser welding processes, J. Phys. D. Appl. Phys. 29 (1996) 1831–1841.

[32] W. Sudnik, D. Radaj, S. Breitschwerdt, W. Erofeew, Numerical simulation of weld pool geometry in laser beam welding, J. Phys. D Appl. Phys. J. Phys. D Appl. Phys. 33 (2000) 662–662.

[33] S. Shanmugam, Numerical and Experimental Investigation of Laser Beam Welding of Aisi 304 Stainless Steel Sheet, Adv. Prod. Eng. Manag. 3 (2008) 93–105.

[34] L. Mei, G. Chen, X. Jin, Y. Zhang, Q. Wu, Research on laser welding of high-strength galvanized automobile steel sheets, Opt. Lasers Eng. 47 (2009) 1117–1124. doi:10.1016/j.optlaseng.2009.06.016.

[35] M.M.A. Khan, L. Romoli, M. Fiaschi, F. Sarri, G. Dini, Experimental investigation on laser beam welding of martensitic stainless steels in a constrained overlap joint configuration, J. Mater. Process. Technol. 210 (2010) 1340–1353. doi:10.1016/j.jmatprotec.2010.03.024.

[36] E. Akman, A. Demir, T. Canel, T. Sinmazçelik, Laser welding of Ti6Al4V titanium alloys, J. Mater. Process. Technol. 209 (2009) 3705–3713. doi:10.1016/j.jmatprotec.2008.08.026.

[37] M. Dhahri, J.E. Masse, J.F. Mathieu, G. Barreau, M. Autric, Laser Welding of AZ91 and WE43 Magnesium Alloys for Automotive and Aerospace Industries, Adv. Eng. Mater. 3 (2001) 504–507. doi:10.1002/1527-2648(200107)3.

[38] Y.J. Quan, Z.H. Chen, X.S. Gong, Z.H. Yu, Effects of heat input on microstructure and tensile properties of laser welded magnesium alloy AZ31, Mater. Charact. 59 (2008) 1491–1497. doi:10.1016/j.matchar.2008.01.010.

[39] H. Al Kazzaz, M. Medraj, X. Cao, M. Jahazi, Nd:YAG laser welding of aerospace grade ZE41A magnesium alloy: Modeling and experimental investigations, Mater. Chem. Phys. 109 (2008) 61–76. doi:10.1016/j.matchemphys.2007.10.039.

[40] N. Ahmed, K.T. Voisey, D.G. McCartney, Investigation into the effect of beam

shape on melt pool characteristics using analytical modelling, Opt. Lasers Eng. 48 (2010) 548–554. doi:10.1016/j.optlaseng.2009.12.013.

[41] R. Fabbro, S. Slimani, I. Doudet, F. Coste, F. Briand, Experimental study of the dynamical coupling between the induced vapour plume and the melt pool for Nd–Yag CW laser welding, J. Phys. D. Appl. Phys. 39 (2006) 394–400. doi:10.1088/0022-3727/39/2/023.

[42] M. Pastor, H. Zhao, T. DebRoy, Continuous waveNd:yttrium–aluminium–garnet laser welding of AM60B magnesium alloys, J. Laser Appl. 12 (2000) 91–100.

[43] R. Ducharmet, K. Williamss, P. Kapadia, J. Dowden, B. Steent, M. Glowackit, The laser welding of thin metal sheets: an integrated keyhole and weld pool model with supporting experiments, J. Phys. D. Appl. Phys. 27 (1994) 1619–1627.

[44] C. Limmaneevichitr, S. Kou, Experiments to simulate effect of Marangoni convection on weld pool shape, Weld. J. 79 (2000) 231s–237s.

[45] P.A.A. Khan, T. Debroy, Alloying element vaporization and weld pool temperature during laser welding of AlSl 202 stainless steel, Metall. Trans. B. 15 (1984) 641–644. doi:10.1007/BF02657284.

[46] H. Ki, J. Mazumder, P.S. Mohanty, Modeling of laser keyhole welding: Part II. simulation of keyhole evolution, velocity, temperature profile, and experimental verification, Metall. Mater. Trans. A. 33 (2002) 1831–1842. doi:10.1007/s11661-002-0191-5.

[47] H. Zhao, T. Debroy, Weld metal composition change during conduction mode laser welding of aluminum alloy 5182, Metall. Mater. Trans. B. 32B (2001) 163–172. doi:10.1007/s11663-001-0018-6.

[48] H. Zhao, T. DebRoy, Pore formation during laser beam welding of die-cast magnesium alloy AM60B-mechanism and remedy, Weld. J. 80 (2001) 204–210.

[49] S. Postma, R.G.K.M. Aarts, J. Meijer, J.B. Jonker, Penetration control in laser welding of sheet metal, J. Laser Appl. 14 (2002) 210. doi:10.2351/1.1493764.

[50] R. Galun, B.L. Mordike, CO 2 Laser Beam Welding of Magnesium-Based Alloys, Weld. J. - New York. (1998) 149–154.

[51] G. Casalino, F. Curcio, F.M.C. Minutolo, Investigation on Ti6Al4V laser welding using statistical and Taguchi approaches, J. Mater. Process. Technol. 167 (2005) 422–428. doi:10.1016/j.jmatprotec.2005.05.031.

[52] M. Mizutani, S. Katayama, A. Matsunawa, Observation of Molten Metal Behavior during Laser Irradiation -Basic Experiment to Understand Laser Welding Phenomena-, 4831 (2003) 208–213.

[53] M.F. Ashby, K.E. Easterling, the Transformation Hardening of Steel Surfaces By Laser Beams-I. Hypo-Eutectoid Steels, Acta Met. 32 (1984) 1935–1948.

[54] J. Dowden, N. Postacioglu, M. Davis, P. Kapadia, A keyhole model in penetration welding with a laser, J. Phys. D. Appl. Phys. 20 (1987) 36–44.

[55] W.M. Steen, J. Dowden, M. Davis, P. Kapadia, A point and line source model of

laser keyhole welding, J. Phys. D. Appl. Phys. 21 (1988) 1255–1260.

[56] M. Beck, P. Berger, F. Dausinger, H. Hugel, Aspects of keyhole/melt interaction in high speed laser welding, in: 8th Int. Symp Gas Flow Chem. Lasers, 1991: pp. 769–774.

[57] A. Kaplan, A model of deep penetration laser welding based on calculation of the keyhole profile A model of deep penetration laser welding based on calculation of the I keyhole profile, J. Phys. D. Appl. Phys. 27 (1994) 1805–1814. doi:10.1088/0022-3727/27/9/002.

[58] C. Lampa, A.F.H. Kaplan, J. Powell, An analytical thermodynamic model of laser welding, J. Phys. D. Appl. Phys. 30 (1997) 1293–1299.

[59] E.H. Amara, A. Bendib, Modelling of vapour flow in deep penetration laser welding, J. Phys. D. Appl. Phys. 35 (2002) 272–280.

[60] R. Fabbro, F. Coste, S. Slimani, F. Briand, Study of keyhole geometry for full penetration Nd-Yag CW laser welding, J. Phys. D. Appl. Phys. 38 (2005) 1881–1887. doi:10.1109/CLEOE.2005.1568435.

[61] F. Tenner, C. Brock, F. Klampfl, M. Schmidt, Analysis of the correlation between plasma plume and keyhole behavior in laser metal welding for the modeling of the keyhole geometry, Opt. Lasers Eng. 64 (2015) 32–41. doi:10.1016/j.optlaseng.2014.07.009.

[62] R. Fabbro, Melt pool and keyhole behaviour analysis for deep penetration laser welding, J. Phys. D. Appl. Phys. 43 (2010) 445501. doi:10.1088/0022-3727/43/44/445501.

[63] N. Postacioglu, P. Kapadia, M. Davis, Upwelling in the liquid region surrounding the keyhole in penetration welding with a laser, J. Phys. D. Appl. Phys. 20 (1987) 340–345.

[64] A. Kar, J. Mazumder, Mathematical modeling of key-hole laser welding, J. Appl. Phys. 78 (1995) 6353–6360. doi:10.1063/1.360686.

[65] X. hu Ye, X. Chen, Three-dimensional modelling of heat transfer and fluid flow in laser full-penetration welding, J. Phys. D. Appl. Phys. 35 (2002) 1049–1056.

[66] J. Mazumder, W.M. Steen, Heat transfer model for cw laser material processing, J. Appl. Phys. 51 (1980) 941–947. doi:10.1063/1.327672.

[67] J. Goldak, A. Chakravarti, M. Bibby, New Finite Element Model for Welding Heat Sources., Metall. Trans. B, Process Metall. 15 B (1984) 299–305. doi:10.1007/BF02667333.

[68] R. Wang, Y. Lei, Y. Shi, Numerical simulation of transient temperature field during laser keyhole welding of 304 stainless steel sheet, Opt. Laser Technol. 43 (2011) 870–873. doi:10.1016/j.optlastec.2010.10.007.

[69] C.W. Hirt, B.D. Nichols, Volume of fluid (VOF) method for the dynamics of free boundaries, J. Comput. Phys. 39 (1981) 201–225. doi:10.1016/0021-9991(81)90145-5.

[70] M. Akbari, S. Saedodin, D. Toghraie, R. Shoja Razavi, F. Kowsari, Experimental and numerical investigation of temperature distribution and melt pool geometry during pulsed laser welding of Ti6Al4V alloy, Opt. Laser Technol. 59 (2014) 52–59. doi:10.1016/j.optlastec.2013.12.009.

[71] M.R. Frewin, D.A. Scott, Finite Element Model of Pulsed Laser Welding, Weld. J. 78 (1999) 15s–22s.

[72] A. De, S.K. Maiti, C.A. Walsh, H.K.D.H. Bhadeshia, Finite element simulation of laser spot welding, Sci. Technol. Weld. Join. 8 (2003) 377–384. doi:10.1179/136217103225005570.

[73] M.M. Collur, A. Paul, T. Debroy, Mechanism of alloying element vaporization during laser welding, Metall. Trans. B. 18 (1987) 733–740. doi:10.1007/BF02672891.

[74] N. Chakraborty, S. Chakraborty, Modelling of turbulent molten pool convection in laser welding of a copper-nickel dissimilar couple, Int. J. Heat Mass Transf. 50 (2007) 1805–1822. doi:10.1016/j.ijheatmasstransfer.2006.10.030.

[75] M.C. Tsai, S. Kou, Marangoni convection in weld pools with a free surface, Int. J. Numer. Methods Fluids. 9 (1989) 1503–1516. doi:10.1002/fld.1650091206.

[76] S. Safdar, A.J. Pinkerton, L. Li, M.A. Sheikh, P.J. Withers, An anisotropic enhanced thermal conductivity approach for modelling laser melt pools for Ni-base super alloys, Appl. Math. Model. 37 (2013) 1187–1195. doi:10.1016/j.apm.2012.03.028.

[77] C.R. HEIPLE, Mechanism for minor element effect on GTA fusion zone geometry, Weld. J. 61 (1982) 975–1025.

[78] G. Tsotridis, H. Rother, E.D. Hondros, Marangoni flow and the shapes of laser-melted pools, Naturwissenschaften. 76 (1989) 216–218. doi:10.1007/BF00627691.

[79] Y. Cheng, X. Jin, S. Li, L. Zeng, Fresnel absorption and inverse bremsstrahlung absorption in an actual 3D keyhole during deep penetration CO 2 laser welding of aluminum 6016, Opt. Laser Technol. 44 (2012) 1426–1436. doi:10.1016/j.optlastec.2011.12.024.

[80] L. Schlessinger, J. Wright, Inverse-bremsstrahlung absorption rate in an intense laser field, Phys. Rev. A. 20 (1979) 1934–1945. doi:10.1103/PhysRevA.20.1934.

[81] G.J. Pert, Inverse bremsstrahlung absorption in large radiation fields during binary collisions-classical theory. II(b). Summed rate coefficients for Coulomb collisions, J. Phys. A. Math. Gen. 9 (1976) 1797–1800.

[82] Y. Zhang, G. Chen, H. Wei, J. Zhang, A novel “sandwich” method for observation of the keyhole in deep penetration laser welding, Opt. Lasers Eng. 46 (2008) 133–139. doi:10.1016/j.optlaseng.2007.08.010.

[83] W. Tan, N.S. Bailey, Y.C. Shin, Investigation of keyhole plume and molten pool based on a three-dimensional dynamic model with sharp interface formulation, J. Phys. D. Appl. Phys. 46 (2013) 55501. doi:10.1088/0022-3727/46/5/055501.

[84] T. Zacharia, S.A. David, J.M. Vitek, T. Debroy, Weld pool development during GTA and laser beam welding of type 304 stainless steel, Part II—experimental correlation, Weld. J. 68 (1989) 510–519.

[85] C.R. Heiple, J.R. Roper, Effect of Selenium on GTAW Fusion Zone Geometry Small additions of selenium to a stainless steel dramatically increase the depth/width ratio of GTA welds, Weld. J. 60 (1981) 143.

[86] S.A. David, T. Debroy, Current issues and problems in welding science., Science. 257 (1992) 497–502. doi:10.1126/science.257.5069.497.

[87] V. V. Semak, J.A. Hopkins, M.H. Mccay, T.D. McCay, Melt pool dynamics during laser welding, J. Phys. D. Appl. Phys. 28 (1995) 2443–2450.

[88] V. V. Semak, G.A. Knorovsky, D.O. MacCallum, On the possibility of microwelding with laser beams, J. Phys. D. Appl. Phys. 36 (2003) 2170.

[89] V. V. Semak, G.A. Knorovsky, D.O. MacCallum, R.A. Roach, Effect of surface tension on melt pool dynamics during laser pulse interaction, J. Phys. D. Appl. Phys. 39 (2006) 590–595. doi:10.1088/0022-3727/39/3/025.

[90] J.-H. Cho, D.F. Farson, J.O. Milewski, K.J. Hollis, Weld pool flows during initial stages of keyhole formation in laser welding, J. Phys. D. Appl. Phys. 42 (2009) 175502. doi:10.1088/0022-3727/42/17/175502.

[91] M. Zhang, G. Chen, Y. Zhou, S. Li, Direct observation of keyhole characteristics in deep penetration laser welding with a 10 kW fiber laser, Opt. Express. 21 (2013) 19997–20004. doi:10.1364/OE.21.019997.

[92] M. Geiger, K.H. Leitz, H. Koch, A. Otto, A 3D transient model of keyhole and melt pool dynamics in laser beam welding applied to the joining of zinc coated sheets, Prod. Eng. 3 (2009) 127–136. doi:10.1007/s11740-008-0148-7.

[93] R. Fabbro, K. Chouf, Dynamical description of the keyhole in deep penetration laser welding, J. Laser Appl. 12 (2000) 142–148. doi:10.2351/1.521924.

[94] S. Basu, T. DebRoy, Liquid metal expulsion during laser irradiation, J. Appl. Phys. 72 (1992) 3317–3322. doi:10.1063/1.351452.

[95] T. Debroy, S.A. David, Physical processes in fusion welding, Rev. Mod. Phys. 67 (1995) 85–112. doi:10.1103/RevModPhys.67.85.

[96] E.H. Amara, R. Fabbro, Modelling of gas jet effect on the melt pool movements during deep penetration laser welding, J. Phys. D. Appl. Phys. 41 (2008) 55503. doi:10.1088/0022-3727/41/5/055503.

[97] R. Fabbro, M. Hamadou, F. Coste, Metallic vapor ejection effect on melt pool dynamics in deep penetration laser welding, J. Laser Appl. 16 (2004) 16–19. doi:10.2351/1.1642633.

[98] R. Fabbro, F. Coste, S. Slimani, F. Briand, Analysis of the various melt pool hydrodynamic regimes observed during Cw Nd-YAG deep penetration laser welding, ICALEO Proc. (2007).

[99] E.H. Amara, R. Fabbro, L. Achab, F. Hamadi, N. Mebani, Modeling of Friction on

Keyhole Walls, in: 23rd Int. Congr. Appl. Lasers Electro-Optics, 2004.

[100] E.H. Amara, R. Fabbro, F. Hamadi, Modeling of the melted bath movement induced by the vapor flow in deep penetration laser welding, J. Laser Appl. 18 (2006) 2. doi:10.2351/1.2164483.

[101] L. Li, D.J. Brookfield, W.M. Steen, Plasma charge sensor for in-process, non-contact monitoring of the laser welding process, Meas. Sci. Technol. 7 (1996) 615–626. doi:10.1088/0957-0233/7/4/019.

[102] P. Norman, H. Engström, A.F.H. Kaplan, Theoretical analysis of photodiode monitoring of laser welding defects by imaging combined with modelling, J. Phys. D. Appl. Phys. 41 (2008). doi:10.1088/0022-3727/41/19/195502.

[103] T.C. Nguyen, D.C. Weckman, D.A. Johnson, H.W. Kerr, High speed fusion weld bead defects, Sci. Technol. Weld. Join. 11 (2006) 618–633. doi:10.1179/174329306X128464.

[104] W. Shimada, S. Hoshinouchi, A Study on Bead Formation by Low Pressure TIG Arc and Prevention of Under-Cut Bead, J. Japan Weld. Soc. 51 (1982) 280–286. doi:10.2207/qjjws1943.51.280.

[105] U. Gratzke, P.D. Kapadia, J. Dowden, J. Kroos, G. Simon, Theoretical approach to the humping phenomenon in welding processes, J. Phys. D. Appl. Phys. 25 (1992) 1640–1647. doi:10.1088/0022-3727/25/11/012.

[106] J. Xie, Dual Beam Laser Welding, Weld. J. 81 (2002) 223s–230s.

[107] M. Beck, P. Berger, F. Dausinger, H. Hugel, Aspects of keyhole/melt interaction in high speed laser welding, in: 8th Int. Symp. Gas Flow Chem. Lasers, Madrid, 1990.

[108] M. Kern, P. Berger, H. Hugel, Magneto-Fluid Dynamic Effects, Weld. J. 79 (2000) 72s.

[109] A. Matsunawa, V. V. Semak, The simulation of front keyhole wall dynamics during laser welding, J.Phys.D: Appl.Phys. 30 (1997) 798–809. doi:10.1088/0022-3727/30/5/013.

[110] Y. Kawahito, M. Mizutani, S. Katayama, S. Steel, Investigation of high-power fiber laser welding phenomena of stainless steel, Trans. JWRI. 36 (2007) 11–16.

[111] Y. Kawahito, M. Mizutani, S. Katayama, High quality welding of stainless steel with 10 kW high power fibre laser, Sci. Technol. Weld. Join. 14 (2009) 288–294. doi:10.1179/136217108X372531.

[112] T. Ilar, I. Eriksson, J. Powell, A. Kaplan, Root Humping in Laser Welding-an Investigation based on High Speed Imaging, Phys. Procedia. 39 (2012) 27–32. doi:10.1016/j.phpro.2012.10.010.

[113] E.H. Amara, R. Fabbro, Modeling of humps formation during deep-penetration laser welding, Appl. Phys. A. 101 (2010) 111–116. doi:10.1007/s00339-010-5768-z>.

[114] S. Pang, L. Chen, J. Zhou, Y. Yin, T. Chen, A three-dimensional sharp interface

model for self-consistent keyhole and weld pool dynamics in deep penetration laser welding, J. Phys. D. Appl. Phys. 44 (2010) 25301. doi:10.1088/0022-3727/44/2/025301.

[115] H. Ki, J. Mazumder, P.S. Mohanty, Modeling of laser keyhole welding: Part I. mathematical modeling, numerical methodology, role of recoil pressure, multiple reflections, and free surface evolution, Metall. Mater. Trans. A. 33 (2002) 1817–1830. doi:10.1007/s11661-002-0190-6.

[116] J. Charles, B. Bonnefois, Super duplex stainless steels: properties and weldability., in: Proc. Conf. Appl. Stainl. Steels, Stockholm, 1992: pp. 1108–1121.

[117] D.J. Kotecki, Ferrite control in duplex stainless steel weld metal., Weld. J. 65 (1986) 273s–278s.

[118] S. Kou, Welding Metallurgy, John Wiley & Sons, Inc., Hoboken, NJ, USA, 2003. doi:10.1002/0471434027.

[119] A. Munitz, Microstructure of Rapidly Solidified Laser Molten AI-4.5 Wt Pct Cu Surfaces, Metall. Mater. Trans. B. 16 (1985) 149–161.

[120] S. Narasimhan, S. Copley, E. Van Stryland, M. Bass, Epitaxial resolidification in laser melted superalloys, IEEE J. Quantum Electron. 13 (1977) 814–814. doi:10.1109/JQE.1977.1069642.

[121] A. Zambon, F. Bonollo, Rapid solidification in laser welding of stainless steels, Mater. Sci. Eng. A. 178 (1994) 203–207. doi:10.1016/0921-5093(94)90544-4.

[122] J.C. Lippold, W.F. Savage, Solidification of Austenitic Stainless Steel Weldments: Part 2—The Effect of Alloy Composition on Ferrite Morphology A transition in ferrite morphology occurs as a function of composition and weld cooling rate, Weld. J. 59 (1980) 48s–58s.

[123] T. Zacharia, S.A. David, J.M. Vitek, T. Debroy, Weld pool development during GTA and laser beam welding of type 304 stainless steel, Part I-Theoretical Analysis, Weld. J. 68 (1989) 499–509.

[124] J.C. Lippold, Solidification Behavior and Cracking Susceptibility of Pulsed-Laser Welds in Austenitic Stainless Steels A shift in solidification behavior under rapid solidification conditions promotes an increase in cracking susceptibility, Weld. J. 73 (1994) 129–139.

[125] V. Kujanpaa, N. Suutala, T. Takalo, T. Moisio, Correlation between solidification cracking and microstructure in austenitic and austenitic-ferritic stainless steel welds., Weld. J. 9 (1979) 55–75.

[126] D.J. Kotecki, T.A. Siewert, WRC-1992 Constitution Diagram for Stainless Steel Weld Metals: A Modification of the WRC-1988 Diagram, Weld. J. 71 (1992) 171–178.

[127] J.A. Brooks, M.I. Baskes, F.A. Greulich, Solidification modeling and solid-state transformations in high-energy density stainless steel welds, Metall. Trans. A. 22 (1991) 915–926. doi:10.1007/BF02659001.

[128] S.L. Lu, M. Qian, H.P. Tang, M. Yan, J. Wang, D.H. StJohn, Massive transformation in Ti–6Al–4V additively manufactured by selective electron beam melting, Acta Mater. 104 (2016) 303–311. doi:10.1016/j.actamat.2015.11.011.

[129] M.J. Perricone, J.N. Dupont, T.D. Anderson, C. V. Robino, J.R. Michael, An Investigation of the Massive Transformation from Ferrite to Austenite in Laser-Welded Mo-Bearing Stainless Steels, Metall. Mater. Trans. A. 42 (2011) 700–716. doi:10.1007/s11661-010-0433-x.

[130] C. D'amato, M. Fenech, S. Abela, J.C. Betts, J. Buhagiar, Autogenous Laser Keyhole Welding of AISI 316LTi, Mater. Manuf. Process. 25 (2010) 1269–1277. doi:10.1080/10426914.2010.490862.

[131] F. Mirakhorli, F.M. Ghaini, M.J. Torkamany, Development of Weld Metal Microstructures in Pulsed Laser Welding of Duplex Stainless Steel, J. Mater. Eng. Perform. 21 (2012) 2173–2176. doi:10.1007/s11665-012-0141-3.

[132] S.S. Babu, J.W. Elmer, J.M. Vitek, S.A. David, Time-resolved X-ray diffraction investigation of primary weld solidification in Fe-C-Al-Mn steel welds, Acta Mater. 50 (2002) 4763–4781. doi:10.1016/S1359-6454(02)00317-8.

[133] Y. Nakao, K. Nishimoto, W.P. Zhang, Effects of Rapid Solidification by Laser Surface Melting on Solidification Modes and Microstructures of Stainless Steels :, Trans. Japan Weld. Soc. 19 (1988) 100–106.

[134] P.S. Mohanty, J. Mazumder, Solidification behavior and microstructural evolution during laser beam—material interaction, Metall. Mater. Trans. B. 29 (1998) 1269–1279. doi:10.1007/s11663-998-0050-x.

[135] S.A. David, S.S. Babu, J.M. Vitek, Welding : Solidification and Microstructure, JOM. (2003) 14–20.

[136] G.G. Roy, J.W. Elmer, T. DebRoy, Mathematical modeling of heat transfer, fluid flow, and solidification during linear welding with a pulsed laser beam, J. Appl. Phys. 100 (2006) 34903. doi:10.1063/1.2214392.

[137] Y.F. Tzeng, Effects of operating parameters on surface quality for the pulsed laser welding of zinc-coated steel, J. Mater. Process. Technol. 100 (2000) 163–170. doi:10.1016/S0924-0136(99)00470-7.

[138] M. Rappaz, S.A. David, J.M. Vitek, L.A. Boatner, Development of microstructures in Fe−15Ni−15Cr single crystal electron beam welds, Metall. Trans. A. 20 (1989) 1125–1138. doi:10.1007/BF02650147.

[139] S.A. David, J.M. Vitek, Laser in metallurgy, in: Conf. Proc. Metall. Soc. AIME, New York, 1981.

[140] T.F. Kelly, M. Cohen, J.B. Sande, Rapid solidification of a droplet-processed stainless steel, Metall. Trans. A. 15 (1984) 819–833. doi:10.1007/BF02644556.

[141] J.A. Siefert, S.A. David, Weldability and weld performance of candidate austenitic alloys for advanced ultrasupercritical fossil power plants, Sci. Technol. Weld. Join. 19 (2014) 271–294. doi:10.1179/1362171814Y.0000000197.

[142] B. Hu, I.M. Richardson, Mechanism and possible solution for transverse solidification cracking in laser welding of high strength aluminium alloys, Mater. Sci. Eng. A. 429 (2006) 287–294. doi:10.1016/j.msea.2006.05.040.

[143] R. Rai, J.. W. Elmer, T.A. Palmer, T. DebRoy, Heat transfer and fluid flow during keyhole mode laser welding of tantalum, Ti–6Al–4V, 304L stainless steel and vanadium, J. Phys. D. Appl. Phys. 40 (2007) 5753–5766. doi:10.1088/0022-3727/40/18/037.

[144] D.T. Swift Hook, A.E.F. GICK, Penetration Welding with Lasers, Weld. J. (1973) 492.

[145] J.G. Andrews, D.R. Atthey, Hydrodynamic limit to penetration of a material by a high-power beam, J. Phys. D. Appl. Phys. 9 (1976) 2181–2194. doi:10.1088/0022-3727/9/15/009.

[146] P.G. Klemens, Heat balance and flow conditions for electron beam and laser welding, J. Appl. Phys. 47 (1976) 2165–2174. doi:10.1063/1.322866.

[147] J. Dowden, M. Davis, P. Kapadia, Some aspects of the fluid dynamics of laser welding, J. Fluid Mech. 126 (1983) 123. doi:10.1017/S0022112083000075.

[148] P.S. Wei, C.Y. Ho, Axisymmetric Nugget Growth During Resistance Spot Welding, J. Heat Transfer. 112 (1990) 309. doi:10.1115/1.2910377.

[149] J. Kroos, U. Gratzke, G. Simon, Towards a self-consistent model of the keyhole in penetration laser beam welding, J. Phys. D. Appl. Phys. 26 (1993) 474–480. doi:10.1088/0022-3727/26/3/021.

[150] X.H. Ye, X. Chen, Three-dimensional modelling of heat transfer and fluid flow in laser full-penetration welding, J. Phys. D. Appl. Phys. 35 (2002) 313. doi:10.1088/0022-3727/35/10/313.

[151] H. Zhao, T. DebRoy, Macroporosity free aluminum alloy weldments through numerical simulation of keyhole mode laser welding, J. Appl. Phys. 93 (2003) 10089–10096. doi:10.1063/1.1573732.

[152] R. Rai, T. DebRoy, Tailoring weld geometry during keyhole mode laser welding using a genetic algorithm and a heat transfer model, J. Phys. D. Appl. Phys. 39 (2006) 1257–1266. doi:10.1088/0022-3727/39/6/037.

[153] R. Rai, G.G. Roy, T. DebRoy, A computationally efficient model of convective heat transfer and solidification characteristics during keyhole mode laser welding, J. Appl. Phys. 101 (2007) 54909. doi:10.1063/1.2537587.

[154] W. Sudnik, D. Radaj, W. Erofeew, Computerized simulation of laser beam welding, modelling and verification, J. Phys. D. Appl. Phys. 29 (1996) 2811–2817. doi:10.1088/0022-3727/29/11/013.

[155] F.M. Ghaini, M.J. Hamedi, M.J. Torkamany, J. Sabbaghzadeh, Weld metal microstructural characteristics in pulsed Nd: YAG laser welding, Scr. Mater. 56 (2007) 955–958. doi:10.1016/j.scriptamat.2007.02.019.

[156] K. Kadoi, A. Fujinaga, M. Yamamoto, K. Shinozaki, The effect of welding

conditions on solidification cracking susceptibility of type 310S stainless steel during laser welding using an in-situ observation technique, Weld. World. 57 (2013) 383–390. doi:10.1007/s40194-013-0023-9.

[157] W. Tan, Y.C. Shin, Multi-scale modeling of solidification and microstructure development in laser keyhole welding process for austenitic stainless steel, Comput. Mater. Sci. 98 (2015) 446–458. doi:10.1016/j.commatsci.2014.10.063.

[158] S.K. Dhua, D. Mukerjee, D.S. Sarma, Effect of cooling rate on the as-quenched microstructure and mechanical properties of HSLA-100 steel plates, Metall. Mater. Trans. A. 34 (2003) 2493–2504. doi:10.1007/s11661-003-0009-0.

[159] D. Thomas, Increased magnesium usage: not just due to density, Automot. Eng. 99 (1991) 47.

[160] H. Baker, Magnesium and Magnesium Alloys, ASM international, Materials Park, OH, 1999.

[161] J.D. Shearouse III, B.A. Mikucki, The Origin of Microporosity in Magnesium Alloy A291, (1994).

[162] L. Griffing, Metals and Their Weldability, in: Weld. Handb., American Welding Society, Miami, FL, 1972.

[163] B. Irving, Blank Welding Forces Automakers to Sit Up and Take Notice, Weld. J. 71 (1991) 39–45.

[164] P.A. Hilton, Optical and Quantum Electronics, Opt. Quantum Electron. 27 (1995) 1127–1147.

[165] H. Zhao, D. White, T. DebRoy, Current issues and problems in laser welding of automotive aluminium alloys, Int. Mater. Rev. 44 (1999) 238–266.

[166] M. Courtois, M. Carin, P. Le Masson, S. Gaied, M. Balabane, A complete model of keyhole and melt pool dynamics to analyze instabilities and collapse during laser welding, J. Laser Appl. 26 (2014) 42001. doi:10.2351/1.4886835.

[167] C. Kim, L.S. Weinman, Porosity formation in laser surface melted aluminum alloys, Scr. Metall. 12 (1978) 57–60. doi:10.1016/0036-9748(78)90227-2.

[168] H. Zhao, W. Niu, B. Zhang, Y. Lei, M. Kodama, T. Ishide, Modelling of keyhole dynamics and porosity formation considering the adaptive keyhole shape and three-phase coupling during deep-penetration laser welding, J. Phys. D. Appl. Phys. 44 (2011) 485302. doi:10.1088/0022-3727/44/48/485302.

[169] M. Courtois, M. Carin, P. Le Masson, S. Gaied, M. Balabane, A new approach to compute multi-reflections of laser beam in a keyhole for heat transfer and fluid flow modelling in laser welding, J. Phys. D. Appl. Phys. 46 (2013) 505305. doi:10.1088/0022-3727/46/50/505305.

[170] W.I. Cho, S.J. Na, C. Thomy, F. Vollertsen, Numerical simulation of molten pool dynamics in high power disk laser welding, J. Mater. Process. Technol. 212 (2012) 262–275. doi:10.1016/j.jmatprotec.2011.09.011.

[171] W.I. Cho, S.J. Na, M.H. Cho, J.S. Lee, Numerical study of alloying element

distribution in CO2 laser-GMA hybrid welding, Comput. Mater. Sci. 49 (2010) 792–800. doi:10.1016/j.commatsci.2010.06.025.

[172] W. Sudnik, D. Radaj, W. Erofeew, Computerized simulation of laser beam weld formation comprising joint gaps, J. Phys. D. Appl. Phys. 31 (1998) 3475–3480. doi:10.1088/0022-3727/31/24/011.

[173] M.M.A. Khan, L. Romoli, M. Fiaschi, G. Dini, F. Sarri, Experimental design approach to the process parameter optimization for laser welding of martensitic stainless steels in a constrained overlap configuration, Opt. Laser Technol. 43 (2011) 158–172. doi:10.1016/j.optlastec.2010.06.006.

[174] S.H. Wang, M.D. Wei, L.W. Tsay, Tensile properties of LBW welds in Ti–6Al–4V alloy at evaluated temperatures below 450 °C, 2003. doi:10.1016/S0167-577X(02)01074-1.

[175] H.R. Shercliff, M.F. Ashby, The prediction of case depth in laser transformation hardening, Metall. Trans. A. 22 (1991) 2459–2466. doi:10.1007/BF02665012.

[176] P.H. Steen, P. Ehrhard, A.S. Ssler, Depth of Melt-Pool and Heat-Affected Zone in Laser Surface Treatments, Metall. Mater. Trans. A. 25 (1994).

[177] N. Sonti, M.F. Amateau, Finite-Element Modeling of Heat Flow in Deep-Penetration Laser Welds in Aluminum Alloys, Numer. Heat Transf. Part A Appl. 16 (1989) 351–370. doi:10.1080/10407788908944721.

[178] N. Sonti, Influence of Process Parameters on Laser Weld Characteristics in Aluminum Alloys, 1988.

Appendix

Several experimental and modeling studies have been performed to understand the influence of process parameters on melt-pool and keyhole features. This Appendix contains summaries of a number of these studies.

Chande and Mazumder [7] evaluated the influence of process parameters on the melt-pool shape and cooling rates. They used a finite difference model for the heat source and assumed a quasi-steady state model and observed that when a surface reflectivity is very high, there is no melting; however, as surface melting occurs, surface reflectivity variation has no influence on other process parameters. Therefore, in their model, at the temperatures higher than the melting temperature, the surface reflectivity is considered zero. They concluded that the depth of the penetration is more affected than the width of

the weld by the absorption of laser energy in the keyhole. Lankalapalli et al. [31] presented a two-dimensional heat conduction model (heat conduction in the axial direction is neglected) to estimate the dependence of penetration depth on process parameters. They obtained the depth of penetration by equating the conducted heat in the substrate to the absorbed laser power.

The interdependency between the melt-pool and the keyhole has been investigated. Ducharme et al. [43] presented an integrated model of laser welding, taking into account the conditions in the keyhole as well as in the melt-pool, interactively. These authors investigated the influence of process parameters on melt-pool shape. Whether penetration was full, partial or blind, the melt-pool shape was different. However, their model is applicable only for full penetration. They concluded that a change in process parameters has more influence on the length of the melt-pool than on its width or shape.

To simulate the laser penetration welding process, Sudnik et al. [154] considered the keyhole, the melt-pool, and the solid substrate as a single nonlinear thermodynamic continuum and divided the whole process to submodels for laser beam, plasma formation, radiation absorption, vapor channel, melt-pool, and solid substrate. This allowed them to calculate the keyhole and melt-pool geometries and temperature distribution, as well as energy losses due to, for example, reflection, vaporization, and radiation. In a later contribution, Sudnik et al. [32] enhanced this model by suggesting a correlation between the depth and the length of the melt-pool. They added the consideration of heat transport due to the moving flow in the radial direction. In the case of a constant welding speed with a varying laser power, they suggested a linear correlation between the depth and the length of the melt-pool. These authors also investigated laser welding of overlap joints

[172] and suggested a low welding speed in cases of larger gap widths so that there would be time for the heat to expand through the gap more uniformly.

Butt-welding is a technique used to connect parts that are nearly parallel and do not overlap. Benyounis et al. [12] investigated laser butt-welding and developed linear and quadratic-fitted polynomial equations for predicting the heat input and the weld-bead geometry. They asserted that achieving the maximum penetration is possible by using the maximum laser power with a focused beam while the welding speed is minimum. They confirmed that the most important factors affecting the welded zone width are the welding speed and the laser focal point position. Shanmugam et al. [33] carried out experiments in which they obtained excellent weld bead geometry by selecting an effective combination of input parameters and radiating the laser beam with different angles to the specimen surface.

To better understand the behavior of steel during the welding process, Mei et al. [34] constructed a setup to avoid most of the defects, such as pores and cracks in the HAZ by optimizing the process parameters. They also determined various mechanical properties of the alloy and the welded joints. Based on the results of these tests, they confirmed that both the yield strength and the tensile strength of the welded joints are higher than those of the base metal. They stated that by moving the focal point position down to the depth, melt-pool depth increases at first and, then, decreases. To understand the effects of laser power, welding speed, and fiber diameter on bead geometry and mechanical properties of the weld, Khan et al. [35] conducted an experimental investigation of laser beam welding in a constrained overlap configuration. They found that welding speed and laser power are the most significant factors that influence weld bead geometry. By increasing the

energy density input, the bead profile shape changes from conical to cylindrical. In another study, Khan et al. [173] presented an experimental design approach to process parameter optimization. They developed a set of mathematical models to obtain the graphical optimization of the results, and thus, the optimal parameters.

The low density, excellent high-temperature mechanical properties, and good corrosion resistance of Ti and its alloys have led to successful applications of these materials in a variety of fields, such as the medical, aerospace, automotive, petrochemical, nuclear and power generation industries [51,174]. Fusion welding of Ti has been performed principally using inert gas-shielded arc and high-energy beam welding processes. Laser welding of Ti-6Al-4V alloy is widely used in aerospace and other applications. Casalino et al.[51] investigated laser welding of Ti-6Al-4V alloy using either lap or butt configurations and obtained the process parameters that lead to welds with the minimal number of imperfections. A pulsed and continuous wave mode laser has been used to weld Ti alloys. In pulse-mode laser welding, the most important parameter affecting the penetration depth is the peak power of the pulsed laser [36]. If it is too high, it creates vapors on the surface of the material, preventing the laser beam from reaching the material and the penetration depth remains constant. Therefore, for increasing the penetration depth while preventing creation of vapor craters, the peak power should be kept constant and the pulse duration increased. These researchers illustrated the relationship between peak power, HAZ width, and melt-pool width: the higher the peak power, the higher is the transfer of heat energy to the keyhole walls, and the higher is the proportion between the HAZ width and the melt-pool width [36]. In order to determine the influence of the heat input on the quality of the welded joint, Quan et al. [38] carried

out experiments and showed that by increasing the heat input, the widths at the top and at the bottom of the weld become are about equal and more craters and pores are created. Combining various models and concepts, such as multiple reflections of laser beam in the keyhole, Al-Kazzaz et al. [39] calculated the geometry of keyhole and weld profiles as well as the temperature gradient in the melt-pool.

Shercliff and Ashby [175] developed a model involving both Gaussian and non-Gaussian heat sources. This enhanced model is applicable for all practical beam speeds. They also presented process diagrams, in a combined form called a “Master Diagram”, for rectangular heat sources so that process variables could be selected to achieve optimum results. Steen et al. [176] presented a simple relation between the penetration depth and the process parameters using a one-dimensional conduction balance without radiative heat transfer. They assumed that the material properties are constant for all temperature ranges and claimed that the state of the convection in the melt-pool does not affect the prediction of the depth of the pool. Ahmed et al. [40] used three heat sources to investigate the effect of heat source on the melt-pool shape in laser welding of Inconel 625. The heat sources were a single circular Gaussian beam and two superimposed multiple Gaussian heat sources forming a rectangular beam and one made up of three laser beams and the other of ten beams. The melt-pool profiles modeled using rectangular beams agreed with the experimental results, considering the dependence on the scanning speed. These profiles have a top-hat shape at higher speeds and a crescent shape at lower speeds, as is seen experimentally.

Chan et al. [24] used non-dimensional forms of the energy, continuity, and momentum equations and found the highest fluid velocity and the solidification start

position at the edge of the beam due to the maximum temperature gradient at this point. The width-to-depth ratio of the melt-pool increases with increase in Pr. The increase of this ratio with increase of the surface tension number was not uniform; specifically, it increased up to surface tension number of 55,000 and then it decreased. To evaluate the shape of the melt-pool, Sonti and Amateau [177] solved a non-linear heat conduction model using FEA and calculated the temperature distribution in the melt-pool. The results were comparable the results of the experiments that Sonti [178] had carried out to evaluate the influence of the process parameters on laser welding of Al alloys.

3. Size Effects on Geometrical Accuracy for Additive Manufacturing of Ti-6Al-4V ELI Parts

3.1 Introduction

Among various types of manufacturing processes for different applications based on material and design, Additive Manufacturing (AM) offers several advantages such as design and manufacturing process consolidations, manufacturing of complex structures, and customization. Still, the geometrical accuracy of the parts produced by this method is questionable when dealing with high tolerances and very small features, often requiring post-AM subtractive manufacturing. Furthermore, the mismatch between as-designed and as-manufactured geometry of AM can lead to the inconsistency in the mechanical properties of additively manufactured parts [1, 2]. Powder bed fusion (PBF) AM is perhaps the most widely adopted AM technique for metallic part manufacturing in various industrial sectors such as aerospace, biodevice, and automobile [3–5]. PBF is based on spreading a thin layer of metal powders and scanning the part geometry using a moving laser (direct metal laser sintering, DMLS) or electron beam (EBM) in a prescribed scan pattern. Repeating this process in successive layers generates the designed three-dimensional geometry. The curing zone, material properties such as melting point, conductivity, and thermal expansion coefficient, the overall temperature of the part during PBF, which is a function of the size and shape of the geometry, build platform temperature, PBF process parameters, powder physical properties such as tap density and size distribution are along the parameters affecting the dimensional accuracy of PBF-AM process. This study focuses on the dimensional accuracy of DMLS as a PBF-AM technique for Ti-6Al-4V ELI material.

Two more factors, i.e. part orientation and part location on the build platforms, are added to the above-mentioned parameters as the dominant factors controlling the accuracy and resolution of features using a study in the polymer PBF process [6]; these factors become especially important for those geometries with significant overhanging. Combined effect of build angle and part position was studied in [7]. Many studies have been performed to determine the dimensional accuracy of various additively manufactured parts with different geometries. Childs and Juster [8] carried out one of the first investigations in this area in 1994 and compared the resolution limits of different additive manufacturing techniques, including selective laser sintering, photopolymerization, laminated object manufacturing, and fused deposition modeling. Senthilkumaran et al. [9] studied nylon specimens (polyamide 12) with different lengths to examine the nature of shrinkage occurring during the selective laser sintering process and reported different shrinkage behaviors in different directions. Weiss et al. [10] proposed an interpolation method to estimate the minimum feature size, which is printable using nylon in the selective laser sintering process. Meisel and Williams [11] designed a series of experiments to determine the key parameters, which affect the constraints in the Polyjet material process. Moylan et al. [12, 13] produced a test artifact to evaluate the performance of six different additive manufacturing systems, including DMLS (stainless steel), selective laser sintering (polymer), EBM (titanium), Fused Deposition Modeling (FDM), stereolithography, and binder jetting. They used the results to evaluate how the measurement results could be used to improve different AM techniques.

In laser-based AM processes of metals, process parameters such as laser power, scan speed, and scan spacing change the characteristics and geometry of the melt-pool[14]. Khorasani et al. [15] manufactured a Ti-6Al-4V prosthetic acetabular shell and examined the possible fabrication limitations. They found more than 1% inaccuracy in the AM parts. Charles et al. [16] used a 3D Systems ProX® DMP 320 machine to correlate different process parameters, including laser power, scan speed, and scan spacing to the dimensional accuracy of DMLS for Ti6Al4V ELI parts containing different overhanging angles. The effect of powder reuse is investigated in [17]. Zhang et al. [18] introduced the scan strategy, track width, and solidification shrinkage as other important factors governing the horizontal dimensional accuracy in DMLS of Ti-6Al-4V parts. Han et al. [19] showed scan strategy has more effect on the surface roughness of the side surfaces rather than the top surface, thus more influence on dimensional accuracy in the horizontal direction rather than the build direction.

To evaluate the accuracy and precision of AM parts, and compare it with subtractive manufacturing (SM) systems, Braian et al. [5] produced two geometric objects using five different AM machines and one SM machine. They observed the most consistent results in SM parts presenting tolerance of <0.050 mm, while among the AM systems, the highest overall precision was observed in CoCr parts, with an overall precision below 0.050 mm. Kirsch et al. [20] carried out a dimensional accuracy study on gas turbine microchannel designs of an aircraft engine. They used different materials, including CoCr, Inconel 718, and Hastelloy-X, and reported geometrical differences as much as 18% using the same material, and 30% when a different material was used. Kruth et al. [21] demonstrated the possibilities of five different DMLS systems for producing

functional metal components using a bronze alloy and steel materials. Delgado et al. [22] used a bronze-based metal powder and an EOS M250 machine to examine the repeatability of DMLS.

Bagheri et al. [23] evaluated DMLS-fabricated porous microarchitecture and introduced a compensation strategy, reducing the morphology mismatch between as-designed and as-manufactured geometries. To optimize the robustness and controllability of the production of DMLS porous Ti-6Al-4V structures, Bael et al. [20] aimed to reduce the mismatch between the designed and manufactured morphological and mechanical properties. They manufactured porous Ti-6Al-4V structures with different pore sizes, analyzed them using microfocus X-ray computed tomography (micro-CT) image analysis, and obtained empirical correlation functions, using which the discrepancies between the manufactured features and the designs were reduced by more than 80%. Although the dimensional accuracy of PBF process has been studied for features with different sizes, including small features in porous structures, there is no work in literature that comprehensively investigates the size and geometry dependence of these dimensional inconsistencies.

In this work, the size and geometry dependence of dimensional accuracy are comprehensively investigated for DMLS-manufactured Ti-6Al-4V ELI features. A significant effort is made to eliminate and separate the effect of global shrinkage, laser curing zone, and partially fused powders from the size and geometry dependent dimensional inconsistency during the DMLS process. Furthermore, the inconsistency of the dimensions within a feature as well as for features located at different positions on the build platform is studied. Our design of dimensional features includes holes, gaps, walls,

squares, tubes, and rods with different sizes. Based on the measurements, a mathematical model is proposed to predict the size and geometry dependent dimensional inconsistencies. Finally, the proposed model is tested by DMLS manufacturing of two spinal cages and comparing their measured dimensional inconsistencies to the model predictions.

3.2 Experimental Methods

All the DMLS manufacturing, characterizations, and measurements of this study were performed in the Metal Additive Manufacturing Laboratory (University of Memphis, Memphis, TN), in which temperature and humidity are kept at 23±3°C and 30±5%, respectively. For DMLS of all the designs, an EOS M290 machine with a layer thickness of 30 µm under Argon inert gas was used. The laser power of 280 W, laser speed of 1200 mm/s, hatch distance of 0.14 mm, and 5 mm-width stripe exposure pattern was used for scanning the cross-sections of the considered geometries while the laser power was decreased to 150 W and laser speed was increased to 1250 mm/s to scan the outer contour of the cross-sections. The build platform temperature, recoating speed, and differential pressure were 35 °C, 150 mm/s, and 0.6 mbar, respectively.

To account for the global shrinkage of Ti-6Al-4V ELI in the DMLS process, 0.263 % x-axis and 0.376 % y-axis material-dependent scaling factors were utilized. Using these materials-dependent scaling factors provided the means of study the geometry and size-dependent shrinkage during the DMLS process for small features. Furthermore, the beam offset was set to 0.099 mm to account for the half diameter of the curing zone beyond the outer boundaries of the manufactured geometries.

Table 4 shows the chemical composition of the Ti-6Al4V ELI powders, which were purchased from EOS and a GilSonic UltraSiever GA-8 was used to determine their size distribution. Powder flowability, tap density, and apparent density were measured using a Qualtech Hall Flow Meter and a Qualtech Tap Density Meter, respectively. Figure 4 shows the morphology of the Ti-6Al-4V ELI powders used in the experiments. Table 5 summarizes the powders physical measurements as-received from EOS and used for manufacturing of the designed parts. The used powder was a mix of as-received and previously used powders. Both apparent and tap density of the used powders were slightly higher than the as-received powders reflecting the increased amount of smaller size powders due to prior DMLS processes. In contrast, the flowability of the used powders was slightly lower than the as-received powders, perhaps due to the change in the shape of the powders from near-spherical shapes to more irregular shapes during prior DMLS processes. Nevertheless, Table 5 shows that these changes are negligible in our used powders for all the manufacturing in this study.

Table 4. The chemical composition of the Ti-6Al-4V ELI powders

Element	Al	V	O	N	C	H	Fe	Y	Other elements	Ti
Wt.%	5.5 – 6.5	3.5 – 4.5	0.13	0.05	0.08	0.015	0.25	0.005	0.4	Bal.

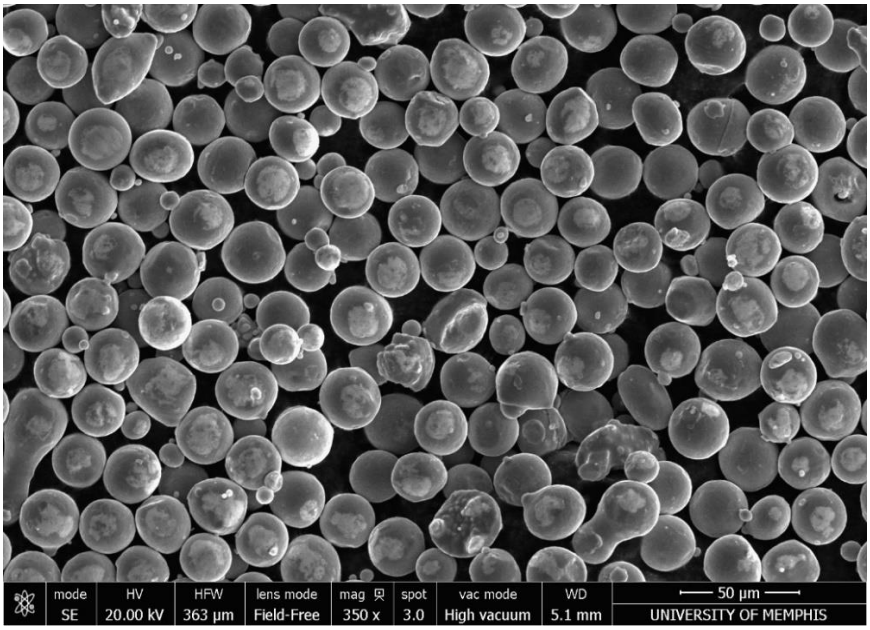

Figure 4. morphology of the Ti-6Al-4V ELI powders used in the experiments

Table 5. Physical characterizations of as-received and used Ti6Al4V-ELI powders.

	As-Received	Used
Apparent Density	2.36 (g/cm^3)	2.41(g/cm^3)
Tap Density	2.70 (g/cm^3)	2.86 (g/cm^3)
Hall Flowability	25.00 (s/50g)	24.14 (s/50g)
Particle Size (µm)	Weight (g/100g)	
>60	1.09	0.25
≤60>53	2.85	1.85
≤53>45	13.87	10.92
≤45>38	31.07	34.42
≤38>32	30.11	29.05
≤32>25	11.98	13.56
≤25>20	5.20	5.77
≤20	3.21	3.57
Total Recovered	99.38	99.39
Average Size* (µm)	34.36±4.13	33.49±4.40

* Calculated based on particles below a sieve size

Figure 5 shows the top view of the designed geometric features and images of the corresponding DMLS-manufactured parts. Both geometrical and position accuracy and their size dependence are considered in the design of the experiments. There are geometric features such as square thickness (ST), rod diameter (RD), wall thickness (WT), and tube thickness (TT) with different sizes to investigate the size effects on the dimensional accuracy of DMLS-manufactured parts. Furthermore, there are geometric features such as channel diameter (CD), vertical gap (VG), and diagonal gap (DG) (0° and 45° with respect to the recoater blade, respectively) to study the position accuracy of DMLS-manufactured parts. As it can be seen in the figure, the geometric features are fabricated on a 25 mm by 25 mm and a polygon with the long edges of 25 mm. Five sets of each design are manufactured to the height of 5 mm located at four corners and at the center of the build plate. The nominal dimensions of these features are provided in Table 6. The dimensions of the features are designed according to the size range of features of some spinal cages so that the results and the proposed model will be applicable to actual parts in the industry, particularly the medical industry.

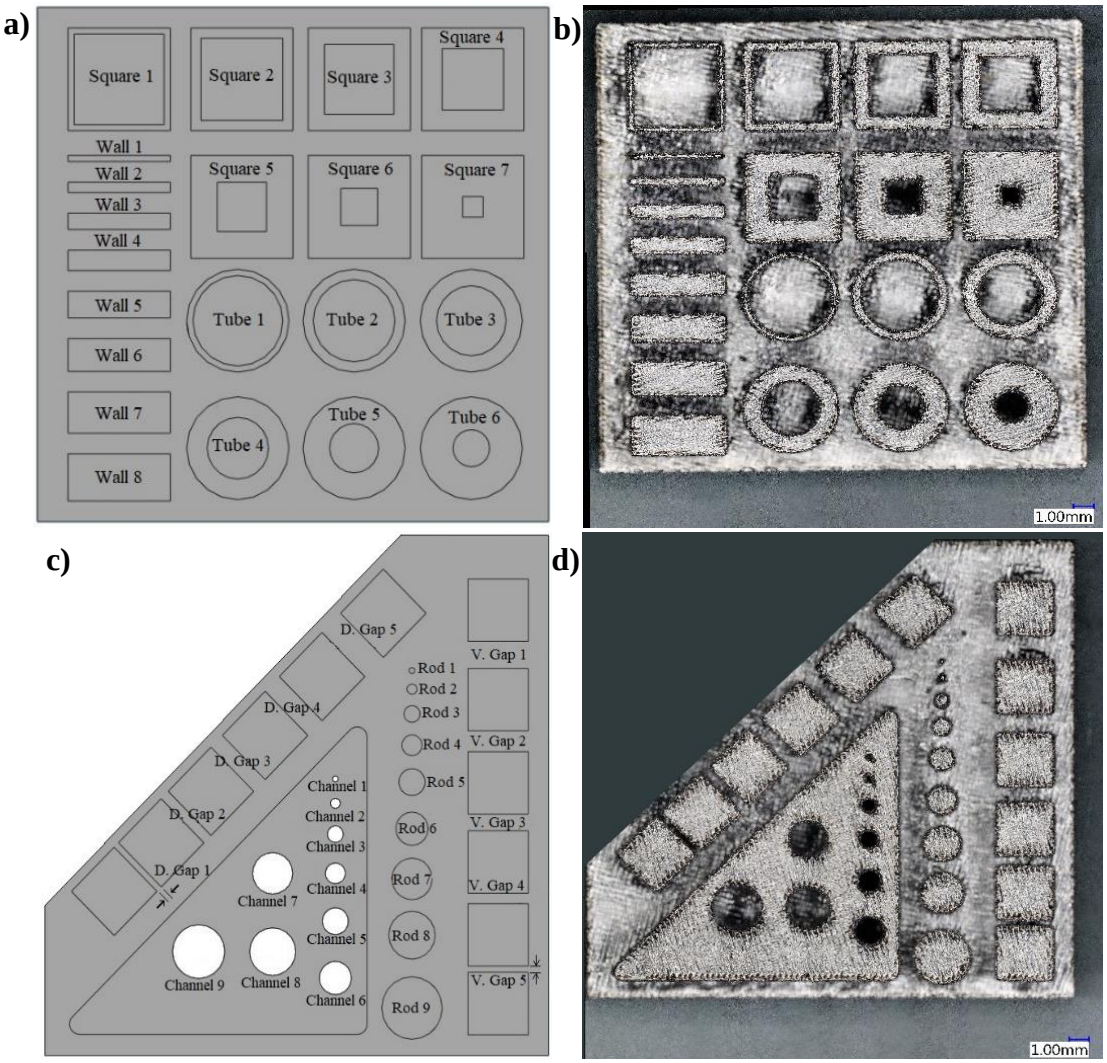

Figure 5. The designed geometric features (a and c) and snapshots of the DMLS-manufactured parts (b and d)

A VHX-6000 Keyence digital microscope is used for all the dimensional measurements of the designed geometric features. The practice to determine the dimensional features for each sample using the digital microscope is shown in Figure 6. Only fully melted material is considered in the dimensional measurements and the size of the partially fused powders attached to the considered feature is ignored. The feature measurements of the part are repeated sufficient times and the average and standard

deviation within that feature are reported in a blue color throughout this article. The blue color is used to distinguish between the standard deviation due to dimensional inconsistency in each feature and the inconsistency between the average measurements between the five parts located at the corners and at the center of the build platform. The latter standard deviations are shown in black.

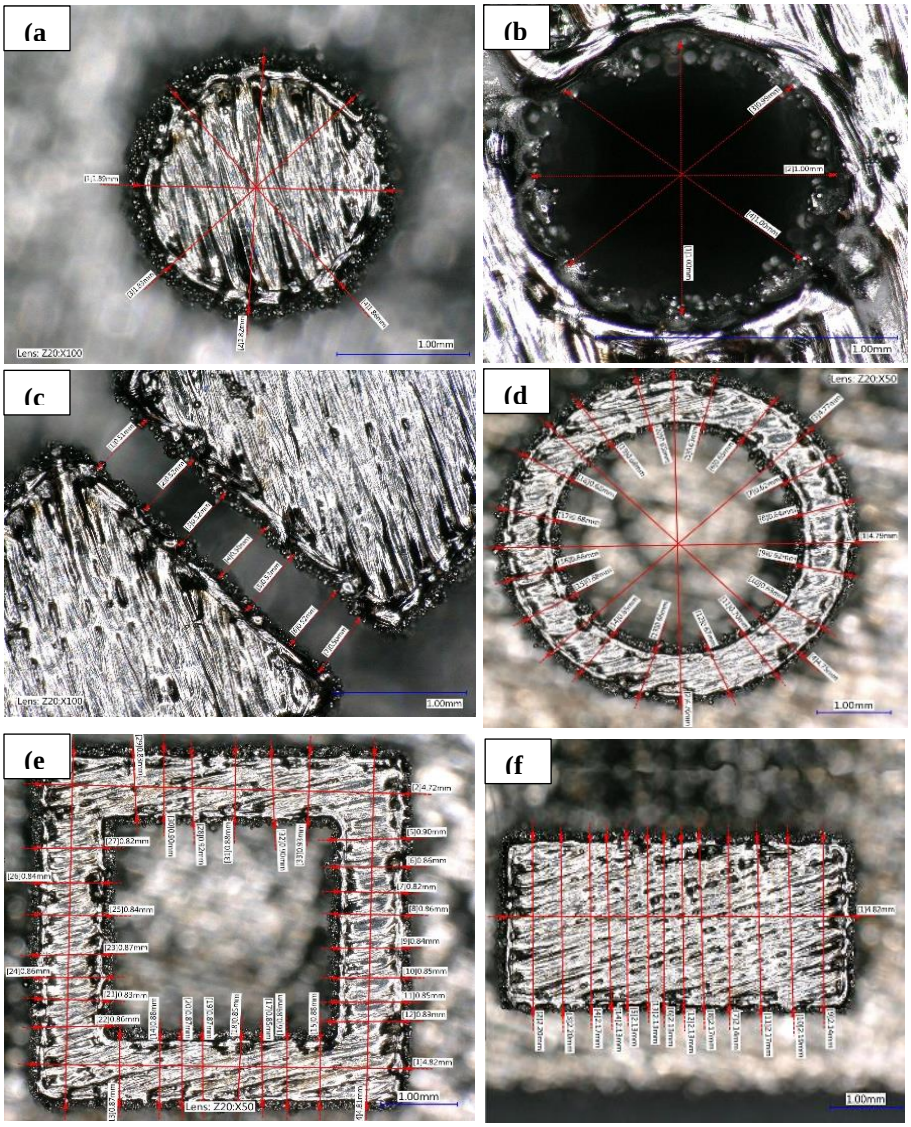

Figure 6. An example of the practice in the measurements of the geometric features: (a) RD=1.85±0.03, (b) CD=1.00±0.00, (c) DG=0.51±0.01, (d) TT=0.66±0.02, (e) ST=0.87±0.03, (f) WT=2.16±0.03

3.3 Results and Discussion

The measured dimensional features for all the five sets of DMLS-manufactured designs are reported in Table 6. The first column lists the names of the features and the five repetitions of each feature. The reported standard deviations in Table 6 reveals that the dimensional accuracy of the DMLS-manufactured features is independent of the location of the part on the build platform; i.e. the uncertainty in the measurements within the features is in the same range (0.01-0.04 mm) of the uncertainty in the measurements for features located at different locations on the build platform. Furthermore, the DMLS-manufactured thicknesses (RD, WT, ST, and TT) are smaller than their nominal sizes for all the cases and the deviation increases by increasing the size of the feature, converging to an approximately fixed value regardless of the geometry (0.1-0.15 mm). Since caliper measurements are used for determining the global shrinkage scaling factors, the 0.1-0.15 mm deviation for sufficiently large features (~>3.0 mm) denotes the difference between the caliper and digital microscope measurements. This difference is due to the partially fused powders attached to the bulk material. In other words, this deviation for sufficiently large features can be eliminated by adjusting the x and y scaling factors.

Table 6. The measured dimensional features for the designs shown in Figure 5

Nominal	0.3(mm)	0.5(mm)	0.8(mm)	1.0(mm)	1.3(mm)	1.6(mm)	2.0(mm)	2.3(mm)	3.0(mm)
RD-1	0.24±0.02[1]	-[2]	0.73±0.02	0.91±0.01	1.22±0.02	1.49±0.01	1.91±0.01	2.19±0.02	2.89±0.01
RD-2	-	-	0.72±0.01	0.89±0.03	1.21±0.02	1.50±0.02	1.90±0.02	2.18±0.02	2.82±0.01
RD-3	0.23±0.01	0.37±0.02	0.66±0.01	0.89±0.01	1.15±0.02	1.43±0.02	1.81±0.02	2.12±0.00	2.82±0.02
RD-4	-	-	0.68±0.02	0.85±0.01	1.16±0.04	1.43±0.03	1.85±0.02	2.15±0.02	2.82±0.02
RD-5	0.24±0.01	0.40±0.01	0.74±0.03	0.95±0.01	1.23±0.04	1.51±0.05	1.85±0.03	2.17±0.01	2.83±0.04
Average	0.24±0.00[3]	0.39±0.02	0.71±0.03	0.90±0.03	1.19±0.03	1.47±0.03	1.86±0.04	2.16±0.02	2.84±0.03
Nominal	0.3(mm)	0.5(mm)	0.8(mm)	1.0(mm)	1.3(mm)	1.6(mm)	2.0(mm)	2.3(mm)	2.6(mm)
CD-1	0.32±0.04	0.51±0.03	0.85±0.01	1.05±0.01	1.31±0.01	1.55±0.02	1.98±0.01	2.25±0.03	2.51±0.01
CD-2	0.31±0.02	0.56±0.03	0.85±0.02	1.03±0.02	1.33±0.04	1.56±0.01	1.94±0.02	2.25±0.01	2.50±0.03
CD-3	0.32±0.01	0.54±0.01	0.84±0.03	1.04±0.02	1.33±0.01	1.57±0.02	1.97±0.01	2.26±0.02	2.52±0.01
CD-4	0.30±0.02	0.50±0.02	0.81±0.03	1.03±0.01	1.31±0.01	1.58±0.01	1.92±0.01	2.22±0.01	2.53±0.01
CD-5	0.34±0.02	0.52±0.02	0.78±0.02	1.03±0.01	1.32±0.03	1.61±0.03	1.96±0.01	2.28±0.01	2.55±0.01
Average	0.32±0.01	0.53±0.02	0.83±0.03	1.04±0.01	1.32±0.01	1.57±0.02	1.95±0.02	2.25±0.02	2.52±0.02
WT-1	0.20±0.03	0.37±0.03	0.69±0.03	0.87±0.04	1.15±0.03	1.48±0.03	1.84±0.03	2.13±0.03	
WT-2	0.19±0.02	0.37±0.03	0.66±0.03	0.87±0.03	1.15±0.03	1.46±0.03	1.85±0.04	2.15±0.02	
WT-3	0.20±0.03	0.41±0.02	0.70±0.02	0.85±0.04	1.16±0.03	1.45±0.04	1.86±0.03	2.14±0.02	
WT-4	0.18±0.03	0.38±0.03	0.69±0.03	0.90±0.01	1.17±0.03	1.46±0.03	1.83±0.02	2.15±0.03	
WT-5	0.17±0.02	0.38±0.03	0.68±0.02	0.87±0.03	1.17±0.02	1.46±0.03	1.86±0.03	2.16±0.03	
Average	0.19±0.01	0.38±0.01	0.68±0.01	0.87±0.02	1.16±0.01	1.46±0.01	1.85±0.01	2.15±0.03	
ST-1	0.18±0.03	0.39±0.03	0.65±0.03	0.86±0.02	1.18±0.03	1.45±0.03	1.85±0.03		
ST-2	0.20±0.04	0.39±0.03	0.69±0.03	0.86±0.04	1.16±0.03	1.48±0.03	1.85±0.03		
ST-3	0.20±0.02	0.46±0.03	0.70±0.02	0.86±0.03	1.20±0.02	1.46±0.01	1.85±0.03		
ST-4	0.19±0.04	0.38±0.03	0.68±0.03	0.90±0.04	1.15±0.04	1.44±0.03	1.82±0.04		
ST-5	0.21±0.03	0.40±0.03	0.71±0.02	0.88±0.03	1.15±0.03	1.47±0.03	1.88±0.03		
Average	0.20±0.01	0.40±0.03	0.69±0.02	0.87±0.02	1.17±0.02	1.46±0.01	1.85±0.02		
TT-1	0.23±0.02	0.43±0.03	0.68±0.04	0.86±0.02	1.16±0.02	1.44±0.02			

TT-2	0.25±0.02	0.45±0.02	0.71±0.02	0.88±0.01	1.17±0.02	1.46±0.02
TT-3	0.25±0.02	0.43±0.01	0.72±0.02	0.90±0.03	1.17±0.02	1.49±0.02
TT-4	0.22±0.04	0.38±0.04	0.67±0.03	0.85±0.01	1.14±0.02	1.44±0.04
TT-5	0.21±0.01	0.45±0.05	0.72±0.02	0.92±0.02	1.22±0.01	1.50±0.01
Average	0.23±0.02	0.43±0.03	0.70±0.02	0.88±0.03	1.17±0.03	1.47±0.02
DG-1	0.34±0.02	0.50±0.02	0.78±0.02	1.00±0.01	1.29±0.02	
DG-2	0.30±0.01	0.50±0.01	0.80±0.01	1.00±0.02	1.31±0.02	
DG-3	0.30±0.01	0.50±0.01	0.80±0.00	1.00±0.00	1.31±0.02	
DG-4	0.35±0.01	0.54±0.02	0.85±0.02	1.00±0.02	1.30±0.03	
DG-5	0.30±0.01	0.51±0.01	0.80±0.01	1.01±0.01	1.38±0.01	
Average	0.32±0.02	0.51±0.02	0.81±0.02	1.00±0.00	1.32±0.03	
VG-1	0.31±0.02	0.51±0.01	0.80±0.01	0.99±0.01	1.29±0.01	
VG-2	0.32±0.03	0.53±0.02	0.83±0.01	1.03±0.02	1.32±0.02	
VG-3	0.31±0.01	0.50±0.01	0.80±0.02	1.00±0.02	1.30±0.01	
VG-4	0.34±0.03	0.51±0.02	0.83±0.02	1.05±0.02	1.32±0.02	
VG-5	0.31±0.01	0.51±0.01	0.81±0.01	1.02±0.02	1.30±0.01	
Average	0.32±0.01	0.51±0.01	0.81±0.01	1.02±0.02	1.31±0.01	

1 Shows the standard deviation for the repeated measurements of a feature as demonstrated in Figure 3.

2 The features DMLS-process was unsuccessful for an unknown reason.

3 Shows the standard deviation for geometric features manufactured at the four corners and at the center of the build platform.

The deviation of the channel diameter (CD) from its nominal size is small and approximately independent of its size. The majority of the deviation of the channels is due to the shrinkage of the surrounding area. Thus, a hole can be considered as a large thickness wherein the effect of the dimension of the hole on its deviation from the nominal size is negligible. The deviations of the vertical and diagonal gaps (VG and DG) from their nominal sizes are also due to the shrinkages of the two walls at the ends of the gaps. Therefore, VG and DG are larger than their nominal sizes and the error is

approximately constant (0.01-0.02 mm) regardless of the size of the gap due to the fact that the two walls have a constant thickness for all the gaps.

In order to further study the size dependence of shrinkage for the designed thicknesses, the percent errors between the nominal sizes of the features with various thicknesses with respect to the DMLS-manufactured dimensions are plotted in Figure 7.

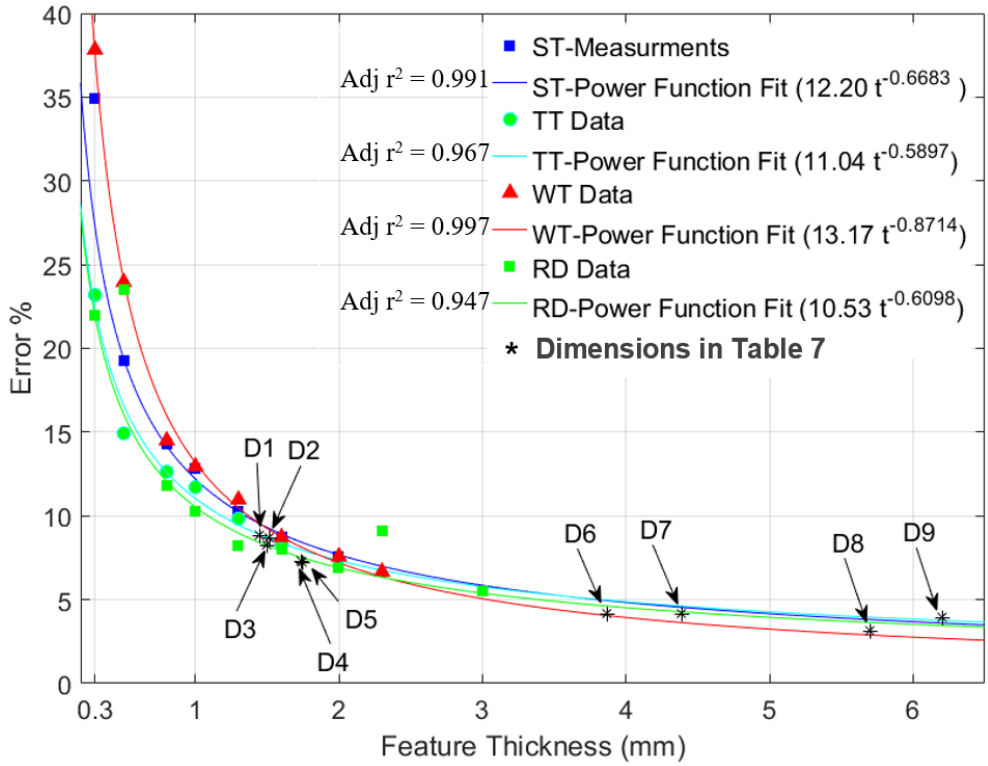

Figure 7. Plot of geometrical errors versus the feature thickness

All the deviations in Figure 7 follow a similar trend of decreasing with increasing of the feature thickness. For features larger than ~1 mm, the differences between the curves for square, wall, tube, and cylinder thicknesses are insignificant. For instance, in 0.3 mm features, the difference between the curves for walls and circles is 37.8 – 23.2 = % 14.6, which is % 63.1 of the total error for 0.3 mm thick circles, whereas, this difference for the same features with 1.3 mm thickness is 10.9 – 9.8 = % 1.1, which is % 11.6 of the total

error for 1.3 mm thick circles. This indicates that the dimensional accuracy of DMLS-manufactured features larger than ~1 mm is approximately geometry independent. This observation indicates that size-dependent shrinkage during the cooling of parts in DMLS is the major source of error in dimensional accuracy of features larger than 1 mm while for the features smaller than 1 mm, the shrinkage is both geometry- and size-dependent.

We propose to formulate the size dependence of dimensional percent errors in DMLS-manufactured features with a polynomial function

$$\textit{Dimensional Error (\%)} = a\, t^{b} \qquad (3.1)$$

where t is the thickness of the feature, and a and b are parameters depending on geometry, process parameters, and material (The value of b is a negative number.). These polynomial functions for the process parameters, material, and considered geometries in this study are shown with solid lines in Figure 7 along with their functions.

To demonstrate the versatility and application of the proposed polynomial fitting at Eq. (3.1) to predict the size dependence of the shrinkage in DMLS, two sizes of spinal cages are manufactured that contain various dimensional features (D1-D9) listed in Table 7. After manufacturing the spinal cages, the dimensions D1-D9 were measured and their percent errors from their corresponding nominal dimensions are listed in Table 7 and shown with black asterisks in Figure 7. It is apparent that these measurements are in close agreement with the polynomial fitting functions. Therefore, these curves can be used to account for the dimensional error of DMLS-manufactured parts.

Table 7. Nominal and actual thicknesses for the features within spinal cages

Feature	D1	D2	D3	D4	D5	D6	D7	D8	D9
Nominal thickness	1.45	1.5	1.52	1.74	1.75	3.87	4.4	5.7	6.21
Actual thickness	1.32 ±0.00	1.38 ±0.01	1.39 ±0.01	1.61 ±0.01	1.62 ±0.01	3.71 ±0.01	4.21 ±0.01	5.52 ±0.01	5.97 ±0.01
Error percentage	8.83	8.20	8.68	7.26	7.20	4.13	4.15	3.09	3.90

3.4 Conclusion

Various geometric features with different thicknesses and sizes were designed and manufactured to investigate the effect of size and geometry, as well as the location on the build platform, on the geometrical accuracy of DSLM-manufactured Ti-6AL-4V ELI parts. The manufactured features were measured using digital microscopy and compared with their nominal dimensions. For holes and gaps, only a negligible deviation from the nominal size was found showing the size independence of the geometrical error in these features. Results for various geometries such as walls, squares, tubes, and rods with different sizes, showed that decreasing the feature size decreases the absolute error value, whereas, the error percentage increases with decreasing the feature size. While all the geometric features follow this trend, a stronger size dependence of the error was observed for walls and squares. The geometry dependence of the error diminishes for features larger than 1 mm and the size dependence of the error converges to a fixed value for sufficiently large features, demonstrating size-dependent shrinkage during DMLS as the possible cause of these dimensional inconsistencies. The polynomial function $a\ t^{-b}$ is proposed to describe the size dependence of the dimensional error in the DMLS process. a and b are parameters depending on geometry, material, and DMLS process parameters. This function is used to successfully predict the dimensional error in the DMLS manufacturing of two spinal cages. Therefore, these functions can be used to account for

these errors in DMLS manufacturing by design change or by adjusting DMLS scaling factors. Finally, comparing the measurements of the features manufactured at different locations on the build platform, showed that the dimensional inaccuracy is not a function of the location of the parts on the build platform.

Acknowledgments

This material is based upon work supported by Medtronic Sofamor Danek USA, Inc. under a Master Research Agreement. BF would like to thank Mr. Joshua Redmond Felipe (UG Biomedical Engineering, University of Memphis) for his help with the digital microscope measurements.

References

1. Parthasarathy J, Starly B, Raman S, Christensen A (2010) Mechanical evaluation of porous titanium (Ti6Al4V) structures with electron beam melting (EBM). J Mech Behav Biomed Mater 3:249–259. https://doi.org/10.1016/J.JMBBM.2009.10.006
2. Hollander DA, von Walter M, Wirtz T, et al (2006) Structural, mechanical and in vitro characterization of individually structured Ti–6Al–4V produced by direct laser forming. Biomaterials 27:955–963. https://doi.org/10.1016/J.BIOMATERIALS.2005.07.041
3. Ozden S, Ekici R, Nair F (2007) Investigation of impact behaviour of aluminium based SiC particle reinforced metal–matrix composites. Compos Part A Appl Sci Manuf 38:484–494. https://doi.org/10.1016/J.COMPOSITESA.2006.02.026
4. Seabra M, Azevedo J, Araújo A, et al (2016) Selective laser melting (SLM) and topology optimization for lighter aerospace componentes. Procedia Struct Integr 1:289–296. https://doi.org/10.1016/J.PROSTR.2016.02.039
5. Braian M, Jönsson D, Kevci M, Wennerberg A (2018) Geometrical accuracy of metallic objects produced with additive or subtractive manufacturing: A comparative in vitro study. Dent Mater 34:978–993. https://doi.org/10.1016/j.dental.2018.03.009
6. Allison J, Sharpe C, Seepersad CC (2017) A Test Part for Evaluating the Accuracy and Resolution of a Polymer Powder Bed Fusion Process. J Mech Des 139:100902. https://doi.org/10.1115/1.4037303
7. Del Re F, Scherillo F, Contaldi V, et al (2019) Mechanical properties characterisation of AlSi10Mg parts produced by laser powder bed fusion additive

manufacturing. Int J Mater Res 110:436–446. https://doi.org/10.3139/146.111761

8. Childs THC, Juster NP (1994) Linear and Geometric Accuracies from Layer Manufacturing. CIRP Ann 43:163–166. https://doi.org/10.1016/S0007-8506(07)62187-8

9. Senthilkumaran K, Pandey PM, Rao PVM (2009) Influence of building strategies on the accuracy of parts in selective laser sintering. Mater Des 30:2946–2954. https://doi.org/10.1016/j.matdes.2009.01.009

10. Weiss B, Diegel O, Storti D, Ganter M (2018) A process for estimating minimum feature size in selective laser sintering. Rapid Prototyp J 24:436–440. https://doi.org/10.1108/RPJ-01-2017-0001

11. Meisel N, Williams C (2015) An Investigation of Key Design for Additive Manufacturing Constraints in Multimaterial Three-Dimensional Printing. J Mech Des 137:111406. https://doi.org/10.1115/1.4030991

12. Moylan S, Slotwinski J, Cooke A, et al (2014) An Additive Manufacturing Test Artifact. J Res Natl Inst Stand Technol 119:429–59. https://doi.org/10.6028/jres.119.017

13. S.Moylan, J. Slotwinski, A. Cooke, K. Jurrens MAD (2012) PROPOSAL FOR A STANDARDIZED TEST ARTIFACT FOR ADDITIVE. In: Solid Freeform Fabrication Symposium. pp 902–920

14. Fotovvati B, Wayne SF, Lewis G, Asadi E (2018) A Review on Melt-Pool Characteristics in Laser Welding of Metals. Adv Mater Sci Eng 2018:. https://doi.org/10.1155/2018/4920718

15. Khorasani AM, Gibson I, Goldberg M, Littlefair G (2017) Production of Ti-6Al-4V acetabular shell using selective laser melting: Possible limitations in fabrication. Rapid Prototyp J 23:110–121. https://doi.org/10.1108/RPJ-11-2015-0159

16. Charles A, Elkaseer A, Mueller T, et al (2018) Effect of process Parameters on Dimensional accuracy of Down-facing surfaces in Selective Laser Melting of Ti6Al4V. In: Advancing Precision in Additive Manufacturing. Berkeley, California

17. Del Re F, Contaldi V, Astarita A, et al (2018) Statistical approach for assessing the effect of powder reuse on the final quality of AlSi10Mg parts produced by laser powder bed fusion additive manufacturing. Int J Adv Manuf Technol 97:2231–2240. https://doi.org/10.1007/s00170-018-2090-y

18. Zhang L, Zhang S, Zhu H, et al (2018) Horizontal dimensional accuracy prediction of selective laser melting. Mater Des 160:9–20. https://doi.org/10.1016/j.matdes.2018.08.059

19. Han J, Wu M, Ge Y, Wu J (2018) Optimizing the structure accuracy by changing the scanning strategy using selective laser melting. Int J Adv Manuf Technol 95:4439–4447. https://doi.org/10.1007/s00170-017-1503-7

20. Kirsch KL, Snyder JC, Stimpson CK, et al (2017) Repeatability in Performance of

Micro Cooling Geometries Manufactured with Laser Powder Bed Fusion. 53rd AIAA/SAE/ASEE Jt Propuls Conf 1–14. https://doi.org/10.2514/6.2017-4706

21. Kruth J-P, Vandenbroucke B, Vaerenbergh J Van, Mercelis P (2005) Benchmarking of different SLS/SLM procceses as rapid manufacturing techniques. In: Int. Conf. Polymers & Moulds Innovations (PMI). Gent, Belgium, pp 1–7

22. Delgado J, Ciuarana J, Reguant C, Cavallini B (2009) Innovative developements in design and manufacturing. In: 4Th international conference on advanced research and rapid prototyping. Leiria, Portugal, pp 349–353

23. Bagheri ZS, Melancon D, Liu L, et al (2017) Compensation strategy to reduce geometry and mechanics mismatches in porous biomaterials built with Selective Laser Melting. J Mech Behav Biomed Mater 70:17–27. https://doi.org/10.1016/j.jmbbm.2016.04.041

4. Process-Property-Geometry Correlations for Additively Manufactured Ti–6Al–4V Sheets

4.1 Introduction

Additive Manufacturing (AM) technologies have provided sustainable production routes for metals, particularly, precious metals such as titanium-based alloys [1]. There are several advantages related to this technology, namely design freedom, reduction in raw material consumption, reduced inventory management need, etc. [2]. However, extending the application of AM to critical components requires a deeper understanding of the process-properties-geometry correlation in additively manufactured components. Direct metal laser sintering (DMLS) is one of the most widely adopted AM techniques to manufacture metallic components in various industrial sectors such as aerospace, biodevice, and automobile [1,3,4]. DMLS is based on spreading a thin layer of metal powders and scanning the part geometry using a moving laser in a prescribed scan pattern and repeating this process layer-by-layer on top of each other. As a result, DMLS-manufactured parts experience a cyclic thermal history which is a function of location in the manufactured geometry and DMLS process parameters. Therefore, the mechanical performance of DMLS-manufactured parts varies by the location in the geometry and the feature size [5]. Understanding this variation and its correlation to material microstructure and defects as well as to the thermal history provides a better understanding of the DMLS process and methods to improve the DMLS process parameters. Furthermore, the process-property-geometry correlations can feed to geometry optimization methodologies for AM such as those currently used to reduce component weight and improve performance [6]. One such an important correlation for DMLS-manufactured parts is the

process-mechanical performance-geometry correlation that is the aim of the current study.

Transferability and robustness of mechanical testing data to the actual component performance require that the mechanical testing data be independent of its geometry. This is valid for traditionally manufactured materials because of their uniform microstructure except for smaller size specimens. For smaller size specimens, geometry dependencies of mechanical testing results have been observed by numerous researchers due to change in the state of stress and increase in the size of defects compared to the volume of the gauge section; e.g. thicknesses from 250 µm [7] or even about 2 µm [8] and 0.5 µm [9] to several millimeters [7,10–13]. Decreasing specimen thickness leads to decreasing the flow stress when the ratio of specimen thickness to grain size is smaller than a critical value; e.g. 20 µm for Fe [14]. The strength of Hercules 3501-6 thermosetting epoxy resin is shown to be dependent on specimen size, as well [7]. That was an increase in the tensile strength with decreasing the gauge section volume. The reason can be attributed to the transition from plane strain to plane stress by decreasing the thickness of the specimens and to the lower probability of having larger flaws in smaller cross sections. Moreover, the smaller specimens have a lower probability of having larger flaws. This size dependency is also observed in thick film specimens. A general trend of increasing Young's modulus and decreasing the ductility with increasing the gauge length in thick films of Ti–6Al–4V alloy and Fe-based metallic glass is reported [11]. Furthermore, an increase in ductility of less than 0.5 mm-thick copper specimens was reported with decreasing the gauge length and increasing the thickness [10]. Kashaev et al. [15]

obtained higher values of elongation for micro-tensile specimens rather than those of standard specimens for Inconel 625, Inconel 718 and Ti-6Al-4V.

Comparing the mechanical properties of steel miniature tensile specimens with those of standard-sized specimens resulted in observing a decrease in tensile strength with decreasing the cross-sectional area [16]. However, an optimum specimen cross-section can be introduced to have the tensile properties correspondent to those of standard-sized specimens. By conducting tensile tests on steel specimens, Akbary et al. [17] observed that the specimen geometry has an insignificant influence on the elastic strain of the material. This was in line with Strnadel and Brumek's [18] results declaring that Yield Strength (S_y), Ultimate Tensile Strength (S_u), and uniform elongation of the plate and cylindrical steel specimens are independent of size. However, post-necking elongation increases with increasing the specimen size. Kumar et al. [19] found no agreement or logical trend in the S_y and elongation at break values for three tested materials, i.e. 20MnNiMo55, CrMoV, and SS304 LN. They also found that the S_y, S_u, and uniform elongation data almost stabilized corresponding to a thickness for the tested materials. However, the total elongation of all the specimens kept increasing with increasing the thickness [20]. Overall, it can be concluded that the tensile strength of materials is geometry-dependent, and it varies with changes in the specimen geometry especially for smaller sizes. However, two different factors are contributing to this geometry dependency, i.e. change in the state of stress in specimen and material microstructure variation with size including defects.

The study of tensile test specimen size dependency of the mechanical properties is also brought to the AM. Foehring et al. [21] evaluated the tensile behavior of additively

manufactured Ti-6Al-4V, printed in two different orientations and using two different layer thicknesses, focusing on the qualitative relationship between microstructure and tensile properties of the specimens. They observed a greater strength for the additively manufactured Ti-6Al-4V compared to conventionally produced material and attributed it to the acicular, or needlelike, grain structure formed during AM process. Reduction of the tensile strength by heat treating was also confirmed by their experiments, as well as an increase in elongation, when the direction of the applied load was perpendicular to the AM build orientation. They reported no influence of layer thickness on strength or ductility of the investigated material. To investigate the effect of the gauge length on the mechanical properties, Karnati et al. [22] fabricated custom-design tensile specimens with gauge lengths of 25.4 mm, 7.6 mm, and 3 mm out of two types of stainless steel, i.e. hot rolled-annealed 304 and 304L, and carried out tensile tests using custom self-aligning grips. A drawback of the specimen designs was that the holes in the specimen grip sections might induce work hardening during drilling/reaming. The bulk material results were consistent, whereas, the additively manufactured results showed a material property variation, which could be due to the differences in size. Since specimens were built to size, different defect distribution could be attributed to different sizes of AM specimens. Moreover, AM specimens with different sizes undergone different solidification dynamics, thus having different microstructures. However, there is no work in literature to differentiate between the geometry (due to the change in the state of stress) dependency and material dependency (due to DMLS process) of DMLS-manufactured metals. Furthermore, variable elongation at break can alter the tensile strength measurements, which can be avoided by constraining $L_0/A_o^{1/2}$ wherein L_0 is gauge length

and A_0 is the cross section area for specimen [23]. The current paper presents the study to consider these issues.

In this paper, we investigate mechanical performance, microhardness, porosity, and microstructure of square sheets of 84 mm with thicknesses ranging from 0.5 mm to 1.6 mm manufactured using DMLS and traditional manufacturing. Specimen with different geometries are cut from these sheets using wire electric discharging (EDM) to minimize the cutting effects and represent "in component" properties, which are properties that can be deployed direct into design of components. First, we present the powder characterization results and a discussion on the effect of powder re-using. Second, we present the results of experiments on traditionally manufactured sheets to determine the specimen geometry effect on the mechanical response of Ti-6Al-4V sheets, allowing specimen geometry-independent study of thickness effects on DMLS-manufactured sheets. Third, we investigate the effect of sheet thickness and the orientation of specimen with the build platform on the mechanical response of DMLS-manufactured sheets. Forth, we study the effect of specimen distance from the free edge followed by the effect of specimen height from the build platform. Finally, we present the microhardness variation with the thickness and height of DMLS-manufactured sheets. In all the sections, we provide discussions on the correlation of mechanical performance and material microstructure, porosity, Oxygen content, as well as DMLS process parameters and thermal history.

4.2 Experimental methods

All the DMLS manufacturing and powder characterizations of this study were performed in the Metal Additive Manufacturing Laboratory (University of Memphis, Memphis, TN), in which temperature and humidity are kept at 23±3 °C and 30±5 %, respectively. The Ti-6Al-4V powders were purchased from EOS and a GilSonic UltraSiever GA-8 was used to determine their size distribution. Powder flowability, tap density, and apparent density were measured using a Qualtech Hall Flow Meter and a Qualtech Tap Density Meter, respectively.

For DMLS of all the designs, an EOS M290 machine under Argon inert gas was used to manufacture square sheets of 84 mm with thicknesses of 0.5 mm, 0.8 mm, 1.0 mm, 1.3 mm, and 1.6 mm. The layer thickness of 30 µm, laser power of 280 W, laser speed of 1200 mm/s, hatch distance of 0.14 mm, and 5 mm-width stripe exposure pattern was used for scanning the cross-sections of the sheets while the laser power was decreased to 150 W and laser speed was increased to 1250 mm/s to scan the outer contour of the cross-sections with two contours; i.e. one at the boundaries of the cross-section and one 200 µm inside of the boundary. The build platform temperature, recoating speed, and differential pressure were 37 °C, 150 mm/s, and 0.6 mbar, respectively. However, the build platform temperature was raised to 45±3 °C during manufacturing due to the heating of the build platform by laser exposure. To account for the global shrinkage in the DMLS process, 0.263 % x-axis and 0.376 % y-axis scaling factors were utilized in the designs. Furthermore, the beam offset was set to 99 µm to account for the half diameter of the curing zone beyond the outer boundaries of the manufactured geometries. Moreover, sheets of Ti-6Al-4V with thicknesses of 0.5 mm, 0.8 mm, 1.0 mm, 1.3 mm,

1.6 mm, 2 mm, and 2.3 mm were obtained from TIMET as traditionally manufactured sheets in this study. All traditionally manufactured sheets were annealed for 30 minutes at 760 °C and then air cooled while all DMLS-manufactured sheets were used as-built.

For tensile testing, specimens with various sizes are used from each thickness to study the effect of specimen size as well as sheet thickness. There are three series of specimens named T, G, and W, in each of which one of the three geometries making the gauge section slab is kept constant (thickness in T series, gauge length in G series, and width in W series). The two other geometrical parameters are subjected to $G/(WT)^{1/2} = 10.20$ constraint to mitigate the specimen size effects on elongation at break [23]; the ratio was determined based on the ratio for ASTM E8-E8M sub-size specimen. Table 8 presents the dimensions of the gauge section for all the specimens. To minimize the cutting effects, a Mitsubishi MV2400-S wire EDM machine with two levels of coarse and fine finishing was employed to cut all the samples. Specimens were cut out from the sheets in $\theta = 0°$ (horizontal), 15°, 30°, 45°, 60°, 75°, and 90° (vertical) orientation with the build platform as illustrated in Figure 8, while making sure that their gage sections are at the middle height of the sheets. The horizontal specimens were cut out from the sheets at various heights to also investigate the effect of height. In addition, the vertical specimens were cut out from the sheets at different distances from the free edges to study the effect of the distance from the free surface, as well. A Shimadzu Autograph AGS-X universal testing system with a load cell capacity of 20 kN equipped with a TRViewX digital video extensometer was employed to carry out the tensile tests. Loading was always applied in a strain-controlled mode at the constant strain rate of 0.001 s^{-1}.

Table 8. The dimensions of the tensile specimens in mm.

Specimen	G	W	T
T-1	6.25	0.75	0.5
T-2	8.07	1.25	0.5
T-3	9.55	1.75	0.5
T-4	10.83	2.25	0.5
T-5	11.97	2.75	0.5
T-6	13.01	3.25	0.5
W-1	13.01	3.25	0.5
W-2	16.46	3.25	0.8
W-3	18.40	3.25	1.0
W-4	20.98	3.25	1.3
W-5	23.27	3.25	1.6
W-6	27.90	3.25	2.3
G-1	20.98	8.45	0.5
G-2	20.98	5.28	0.8
G-3	20.98	4.23	1.0
G-4	20.98	3.25	1.3
G-5	20.98	2.64	1.6

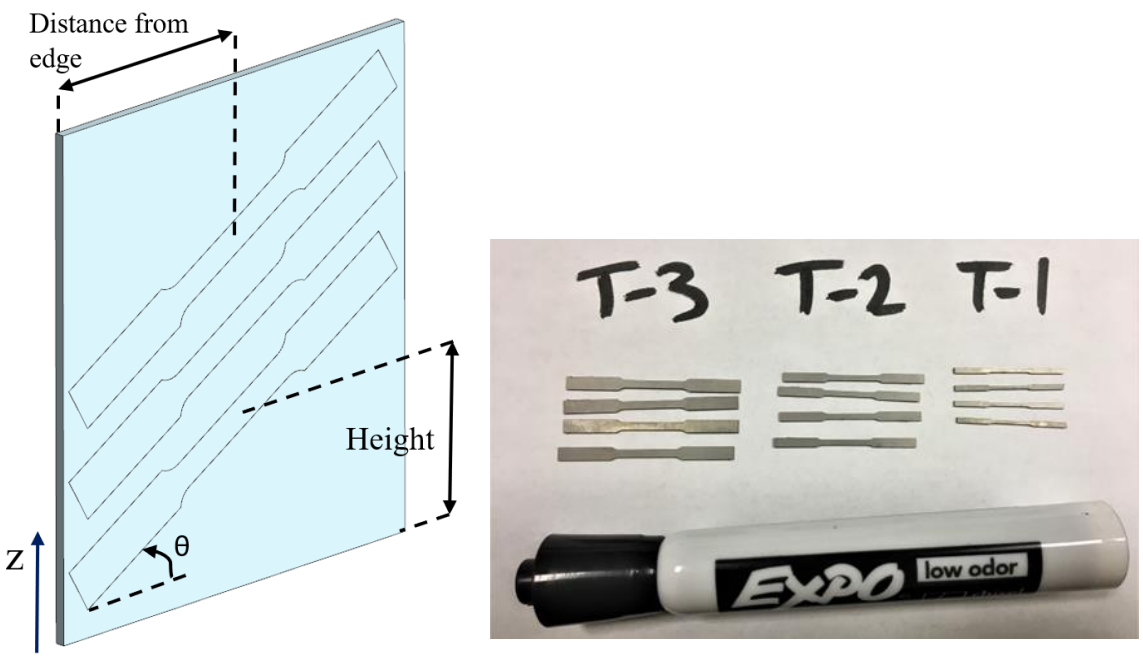

Figure 8. Schematic of the tensile test specimens (left) and Illustration of T-1, T-2, and T-3 specimens (right).

For microstructure and microhardness characterizations, pieces of the sheets were cut using wire EDM, mounted in Phenolic powder using a Leco PR-32 automatic pneumatic mounting press, and polished using a Struers Rotoforce-4 polishing setup in three levels. For plane grinding, a diamond abrasive plate with the size of 220 μm was used with water as coolant for 4 minutes. For fine grinding, a 9 μm diamond abrasive plate was employed with DiaPro Allergorag with the size of 9 μm as a suspension for 7 minutes. For the polishing step, an abrasive plate of colloidal silica suspension in size of 0.04 μm was used, and OP-S* (90% OP-S, 10% H_2O_2) was employed as a lubricant for this step.

A Shimadzu HMV-G Microhardness Tester with Vickers indenter was utilized for microhardness testing. The tests were conducted on a rectangular pattern, having 27 points on each sample for indentation. The average value of these 27 indentations on each sample is used as the value representing the microhardness of the sample. The same samples were used for porosity measurement using a Keyence digital microscope VHX-6000.

The samples prepared for microstructural analysis were mounted and polished using the same method explained above. Then, the samples were etched using Kroll's reagent (AKA Kroll's etch) for 15 seconds. Microstructural images were captured using a Keyence optical digital microscope (OM) VHX-6000 and a NOVA NANO field emission scanning electron microscope (SEM). To achieve better conductivity and better image qualities under SEM, the samples were coated with Pu-Au with a thickness of 5 nm.

The Oxygen (O), Nitrogen (N), and Hydrogen (H) content in powders and DMLS-manufactured parts are measured using Bruker's G-8 Galileo instrument while Bruker's

G-4 Icarus instrument was used for Carbon (C) content determination. For O content measurements in the DMLS-manufactured parts, four 1 mm by 3 mm rectangular bars were fabricated vertically with the same height as the sheets and samples were cut at different heights for analysis.

4.3 Results

4.3.1 Powder Characterization

Table 9 summarizes the physical measurements of the as-received and used powders for manufacturing of the designed parts. The used powder was a mix of as-received and previously used powders. Both apparent and tap density of the used powders were slightly higher than the as-received powders reflecting the increased amount of smaller powders due to prior DMLS processes. In contrast, the flowability of the used powders was slightly lower than the as-received powders, perhaps due to the change in the shape of the powders from near-spherical to more irregular shapes during prior DMLS processes. Nevertheless, Table 9 shows that these changes are negligible in our used powders for all the manufacturing in this study. The size distribution of as-received and used powders are shown in

Table 10.

Table 9. Physical characterizations of as-received and used Ti-6Al-4V powders.

	As-Received	Used
Apparent Density	2.36 (g/cm^3)	2.41(g/cm^3)
Tap Density	2.70 (g/cm^3)	2.86 (g/cm^3)

Hall Flowability	25.00 (s/50g)	24.14 (s/50g)

Table 10. Size distribution of as-received and used Ti-6Al-4V powders.

Particle Size (μm)	Weight (g/100g)	
	As-Received	Used
>60	1.09	0.25
≤60>53	2.85	1.85
≤53>45	13.87	10.92
≤45>38	31.07	34.42
≤38>32	30.11	29.05
≤32>25	11.98	13.56
≤25>20	5.20	5.77
≤20	3.21	3.57
Total Recovered	99.38	99.39
Average Size*	34.36±4.13	33.49±4.40

* Calculated based on particles below a sieve size

Figure 9 shows the surface morphology of the used Ti-6Al-4V powders. It can be seen that overall, they have the spherical shape with fine satellites attached to some of them due to prior DMLS process and/or their production process. There are also some voids on the surface of powders, which are resulted from the atomization process during the manufacturing of powders. Additionally, we can see some non-spherical powders, which can be due to the partial melting/splitting of powders in prior DMLS process.

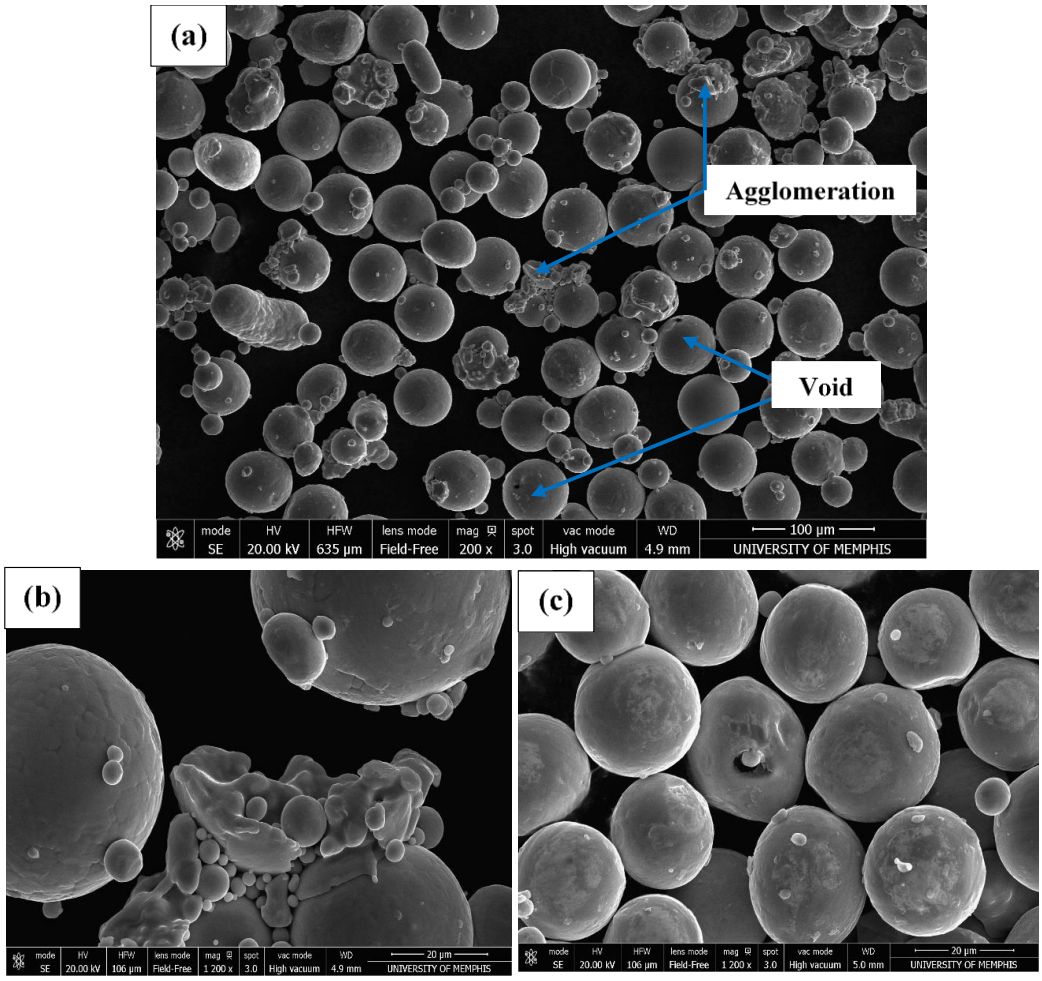

Figure 9. SEM images of the used Ti-6Al-4V powders: (a) Surface morphology, (b) Example of powder agglomeration due to prior DMLS process, and (c) Example of voids in powders.

The Ti-6AL-4V powders nominal contents of ONH-C elements are listed in the second column of Table 11. To evaluate the effect of powder re-using and manufacturing environment on these powders, ONH-C contents in both as-received and used powders were measured. These measurements were repeated for three samples of powders and are listed in the third and fourth columns of Table 11. Although negligible, all the elemental contents are slightly higher than their nominal values which may be due to humidity pick

up (for OH), air exposure (for N), or contamination from the powder container (for C). Furthermore, the variation of OH content in as-received and used powders are within their standard deviations. The content of N increases by powder re-using; however, the N content measurements also show the biggest percentile standard deviations. Therefore, the variation of ONH-C between as-received and used powders are considered insignificant.

Table 11. Nominal, as-received, and used ONH-C elemental contents in Ti-6Al-4V powders.

Element	Nominal	As-Received	Used
O	<1300 (ppm)	1511±132* (ppm)	1634±76 (ppm)
N	<50 (ppm)	90±54 (ppm)	168 ±17 (ppm)
H	<12 (ppm)	28±2 (ppm)	30±3 (ppm)
C	<80 (ppm)	81±10 (ppm)	78±9 (ppm)

* Average and standard deviation for three reputations of the measurement.

4.3.2 Tensile Properties of Ti-6Al-4V Sheets

The stress-strain curves of traditionally manufactured T, G, and W series specimens are presented in Figure 24(a-c) in Appendix, respectively. The stress-strain curves shown in these figures are the averages of at least three tests per specimen. These curves clearly show that elongation at break is approximately constant 12-17 % for all the specimens due to a constant ($L_0/A_0^{1/2}$) = 10.20 ratio used in their designs. Having the same elongation at break for all the specimens allows us to investigate the effects of the thickness of the sheets and specimen geometry on yield stress (S_y) and ultimate tensile strength (S_u).

Figure 25 in the Appendix shows the stress-strain curves of G-1 to G-5 specimens (averaged in all the orientations). Figure 26 in the Appendix shows the stress-strain curves of G-1 to G-5 specimens cut in different orientations where the gauge section mid-points coincide with the half of the maximum height of DMLS-manufactured sheets. Similar to the stress-strain curves for traditionally manufactured sheets, these stress-strain curves are the averages of at least three tests per specimen. The stress-strain curves for the G-1 to G-5 specimens cut horizontally ($\alpha = 0°$) at different heights are presented in Figure 27. The stress-strain curves for G-2, G-3, and G-5 specimens cut vertically ($\alpha = 90°$) at different distances from the free edges of the sheets are presented in Figure 28 in the Appendix.

4.3.3 Microhardness Testing

The variations of microhardness versus the height of the DMLS-manufactured Ti-6Al-4V sheets with thicknesses of 0.5 mm, 1.0 mm, 1.3 mm, and 1.6 mm are presented in Figure 10. The microhardness of DMLS-manufactured sheets varies in 357 to 387 HV (kg/mm^2) range depending on the thickness and the height of the sheet, while the microhardness of traditionally manufactured sheets is independent of the sheet thickness and location and are measured as 317 HV (kg/mm^2).

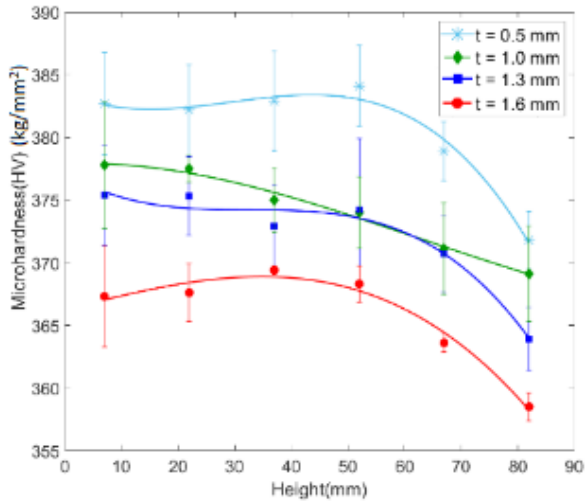

Figure 10. Microhardness variation versus height in DMLS-manufactured Ti-6Al-4V sheets.

4.4 Discussion

4.4.1 Traditionally Manufactured Ti-6Al-4V Sheets

The variation of S_y and S_u with respect to G/T ratio for all the traditionally manufactured specimens are presented in Figure 11(a-b). The results of the T series specimens show the highest standard deviations due to their small volume of the gauge section, making the effects of random defects on the results considerable [24]. Both S_y and S_u follow similar trends for all the three series of specimens, i.e. increase or decrease by increasing G/T ratio. For T series specimens, S_y and S_u decrease by increasing G/T ratio. This increment in S_y and S_u is due to the change of the state of stress from plane strain to plane stress in the gauge section under uniaxial tensile loading [25].

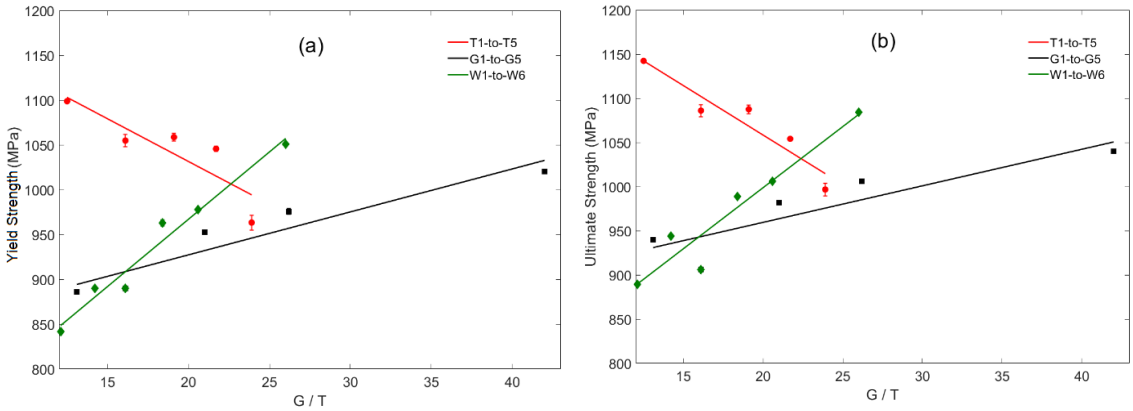

Figure 11. Variations of yield strength (a) and ultimate tensile strength (b) of traditionally manufactured Ti-6Al-4V sheets with respect to G/T ratio. The solid lines are a fitted line to the data and the vertical bars show the standard deviation of each data point

Since one of the variables in the W and G series is their thickness, their behavior is somehow more complicated than the T series, in which the thickness is constant. Traditionally manufactured sheets contain a hardened surface due to their manufacturing process (e.g. cold-rolling) [26,27], which is to a roughly constant depth regardless of the sheet thickness. Therefore, as the thickness of the sheets decreases, it is expected to observe increment in both S_y and S_u because of an increase in the volume ratio of the hardened surface with respect to the total gauge section volume. However, since all the T series specimens have the same thickness of 0.5 mm, the variation of their S_y and S_u is caused only by the geometry of the specimens rather than their manufacturing process.

Therefore, an empirical model for the effect of the geometry of specimen on S_y and S_u can be derived by fitting a line to these data in the T series. The effect of the manufacturing process (material microstructure) on these sheets will be proportional to their thicknesses. Consequently, an empirical equation can be used to roughly describe

the specimen geometry and material manufacturing process for traditionally manufactured sheets

$$\sigma = [\sigma_1^0 + a_1 (G/T)]_{Geom} + [\sigma_2^0 + a_2 (1/T)]_{Mat} \tag{4.1}$$

where σ_1^0, σ_2^0, a_1, and a_2 are empirical model parameters. Such an empirical model can be used to describe the effects of specimen geometry on the mechanical response of DMLS-manufactured sheets if both DMLS manufacturing results in the same microstructure as traditional manufacturing. Figure 12 shows the optical and SEM images of the microstructure of traditionally manufactured sheets. The microstructure consists of equiaxed α with homogenously distributed β at the grain boundaries of α which is due to annealing of the cold rolled sheets at 760 °C for 30 minutes followed by cooling in air. This microstructure is completely different from the martensitic microstructure of DMLS-manufactured sheets, which will be comprehensively discussed in the next sections.

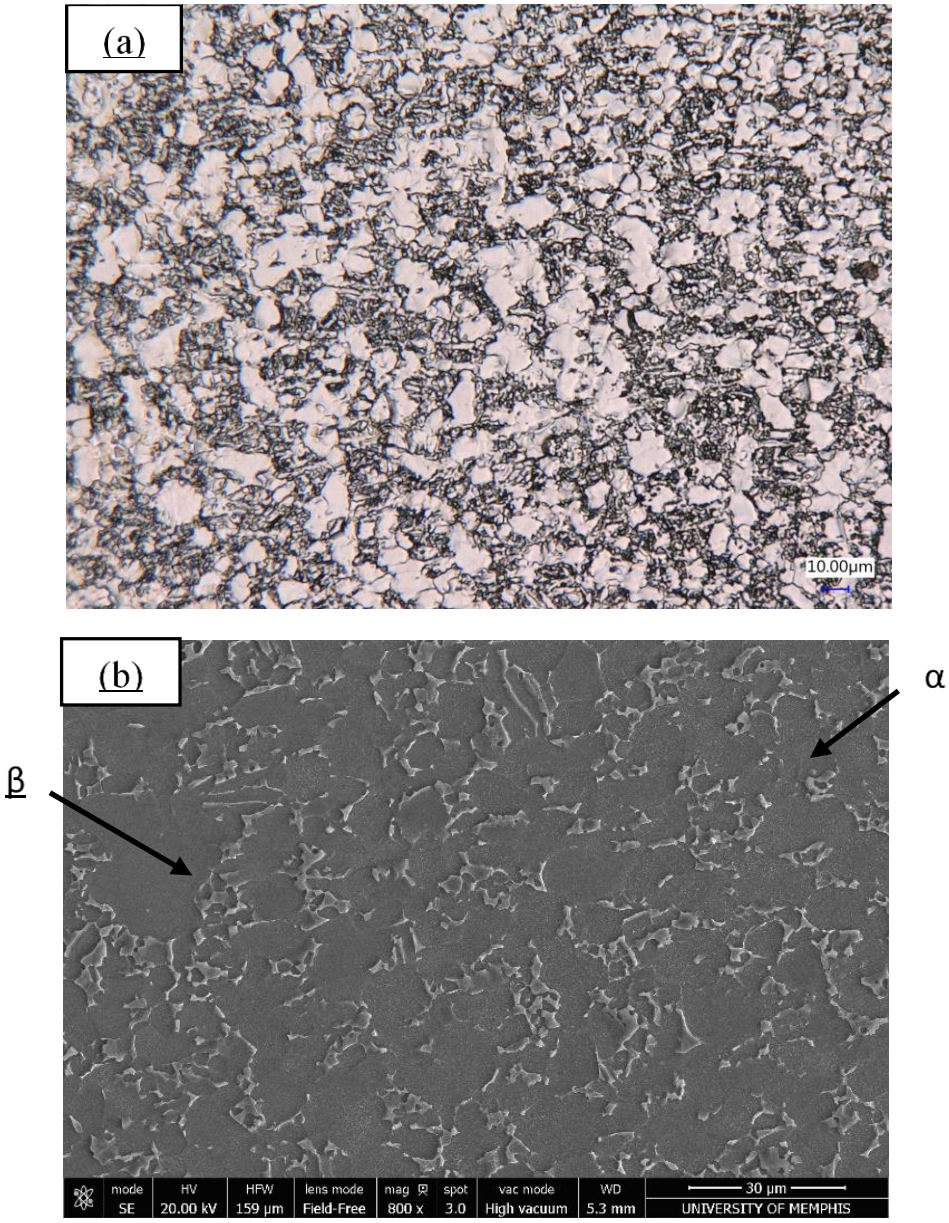

Figure 12. The OM (a) and SEM (b) images of microstructure of traditionally manufactured sheets with thickness of 1.6 mm.

Therefore, to eliminate the effect of surface hardening (material microstructure) on the mechanical behavior of the specimens only the geometry-dependent portion of the S_y and S_u variations are used as the benchmark for the study of the specimen size effect on the mechanical response of DMLS-manufactured sheets. This will allow us to study the

DMLS process effect (material microstructure) on the mechanical response of the sheets independent from the specimen geometry effect. Such variations are the fitted lines to S_u and S_y versus G/T ratio for the T series which include only a constant increase of S_u and S_y due to the surface hardening of a sheet with 0.5 mm-thickness

$$\begin{aligned} S_u &= [1282.3 - 11.196(G/T)]_{Geom}, \\ S_y &= [1222.2 - 9.537(G/T)]_{Geom}. \end{aligned} \tag{4.2}$$

4.4.2 Tensile Properties of DMLS-Manufactured Ti-6Al-4V Sheets

4.4.2.1 Effect of Specimen Size and Orientation

For DMLS-manufactured sheets, G-5 specimen sizes are used because these specimens showed an insignificant standard deviation of the measured S_y and S_u for traditionally manufactured sheets (see Figure 11). In addition, G series specimens are shorter in length compared to some of the W series specimens, reducing their manufacturing time while allowing to investigate the effect of sheet thickness. Similar to the stress-strain curves for traditionally manufactured sheets, these stress-strain curves are the averages of at least three tests per specimen. It is interesting to note the waviness of the curves in the stress-strain curves (Appendix figures) after yielding in all the DMLS-manufactured specimens in this study where the amplitude of the waviness increases as the specimens G/T ratio decreases. Further, the amount of the waviness in traditionally manufactured specimens are negligible compared to the DMLS-manufactured specimens. We offer a possible explanation to this behavior by considering the increased cracks nucleation and propagation rates in DMLS-manufactured sheets due to their fully martensitic microstructure and lower elongation at break, as we will discuss the microstructures of the DMLS-manufactured sheets later in details. Since the tensile testing is performed under constant strain rate mode, the slower force adjustment speed of

the test frame compared to the cracks nucleation and propagation rates (i.e. failure rate) causes the amount of the stress decrease before it abruptly increases to keep the strain rate constant.

Figure 13 (a-c) shows the variation of S_y, S_u, and elongation at break with respect to G/T ratio for these specimens. The elongation at break for all the specimens varies in the range of 4-7 % because ($L_0/A_0^{1/2}$) ratio is constant for all the specimens. This is significantly lower than the 12-17 % elongation at break that was observed for traditionally manufactured sheets which is due to the rapid solidification in the DMLS process turning the microstructure of DMLS-manufactured sheets to fully martensitic microstructure [28]. Observation of a specific trend in the variations of elongation at break versus G/T ratio is not possible due to the high standard deviations of elongation at break between different tests of the same specimen size as it has been reported previously by other authors [21].

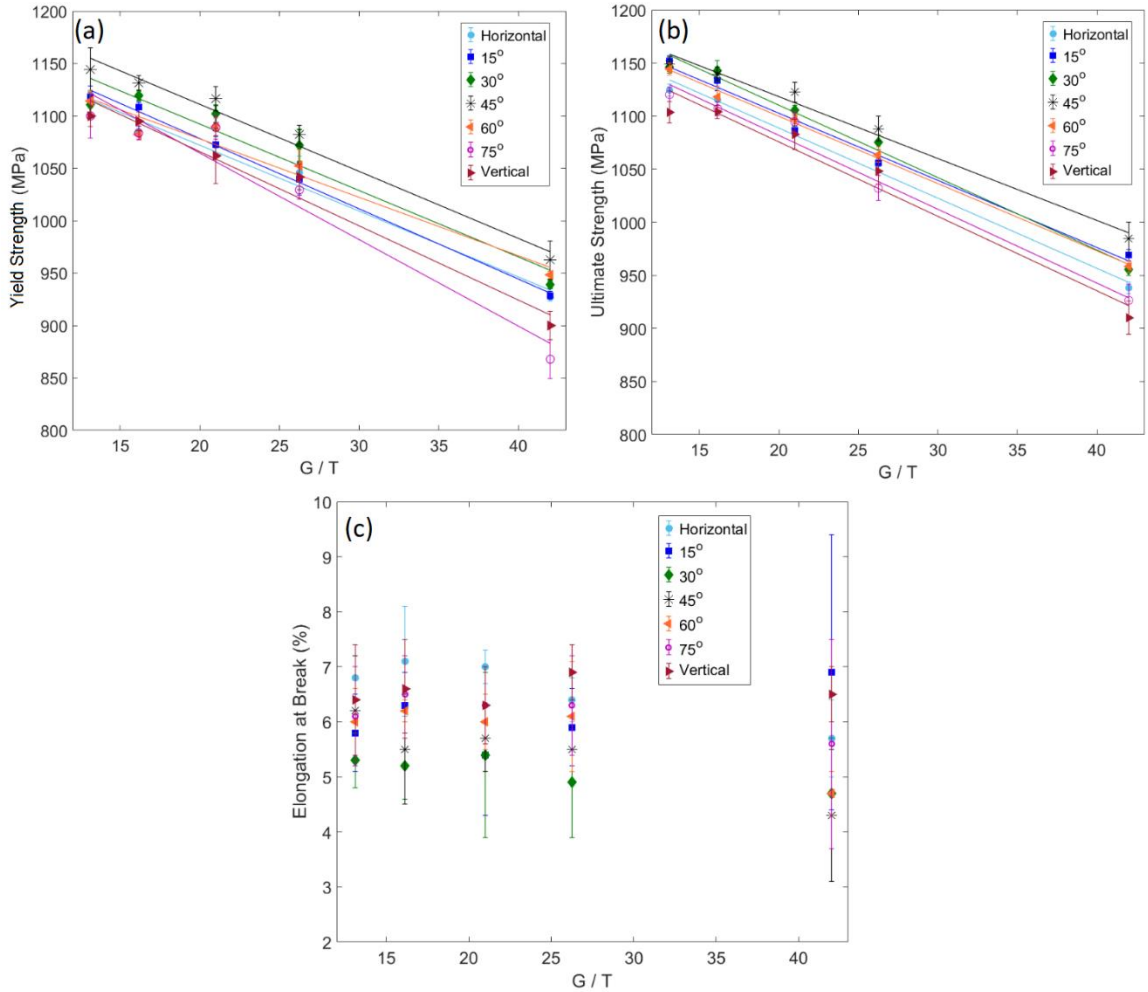

Figure 13. (a) Yield strength, (b) ultimate tensile strength, and (c) elongation at break variations versus G/T ratio for DMLS-manufactured sheets.

Moreover, both S_y and S_u monotonically decrease by increasing the G/T ratio for all the orientations. This is consistent with the specimen geometry effect on S_y and S_u, which was observed for the traditionally manufactured specimens (Eq. 4.2). Similar to the Eq. (4.2), linear equations can be fitted for these data and averaged over all the orientations to represent the specimen geometry effect for DMLS-manufactured sheets as

$$\begin{aligned} UTS &= 1227.9_{\pm 9.6} - 6.557_{\pm 0.391}(G/T), \\ S_y &= 1213.5_{\pm 17.3} - 6.660_{\pm 0.777}(G/T), \end{aligned} \quad \text{For DMLS-manufactured sheets,} \tag{4.3}$$

where the standard deviation is for the variation with respect to orientation. Since the geometry dependency of S_u and S_y is independent of the manufacturing process of the sheets, subtracting Eq. (4.3) from Eq. (4.2) provides the material-dependent variation of S_y and S_u for DMLS-manufactured sheets

$$\begin{aligned} UTS &= [54.4_{\pm 9.6} - 34.8_{\pm 8.1}(1/T)]_{Mat}, \\ S_y &= [8.7_{\pm 17.3} - 60.4_{\pm 16.3}(1/T)]_{Mat}, \quad \text{For DMLS-manufactured sheets.} \end{aligned} \tag{4.4}$$

Therefore, Eq. (4.4) represents the effect of sheet thickness on S_u and S_y in the DMLS process that is a decrease with decreasing the sheet thickness. This behavior can be attributed to overheating of thinner sheets due to three factors. The First factor is the two-contour scan strategy on the boundaries of the part cross-sections after stripe hatching of each layer. Using the simplified equation for absorbed energy [29]

$$E = P / vh \tag{4.5}$$

The absorbed energy is calculated as 1.667 J/mm^2 and 0.600 J/mm^2 for stripe hatching and contours, respectively. As the thickness of the sheets decreases, the middle portion of the cross-section is exposed to additional contour scanning on top of the hatching. The second factor is related to 5 mm-stripe width process parameter that decreases the cooling time between the lines scanning within the stripe for thinner sheets. Therefore, the just-laser-scanned line within the stripe is at a higher temperature when the adjacent line is exposed to laser causing additional absorption of energy for thinner sheets. Consequently, the total absorbed energy for thinner sheets increases, causing more defects in these sheets due to overheating [30]. The third factor is related to the cooling rate variation by the thickness of the sheets. Thinner sheets have smaller cross-sections which are the areas of the conduction cooling channel to previous layers of the sheet and to the build platform. Since conduction, compared to convection to powder bed and

irradiation, is the most significant cooling mechanism in the DMLS process [31], the thinner sheets cool down slower contributing to additional overheating of these sheets. The existence of additional defects in thinner samples is evident by comparing the optical images of sheets with a layer thickness of 0.5 mm shown in Figure 14(a,c,e) with their counterparts for the sheet thickness of 1.6 mm shown in Figure 15(a,c,e). It should be noted here that the higher defect content in thinner sheets can be compensated for by decreasing stripe width or scan strategy that may require changing other DMLS parameters too.

The measured surface porosities at the middle height of the sheets are presented in the third column of Table 12. Surface porosity has a linear relationship with respect to the inverse of the sheet thickness

$$Surface\ Porosity\ (\%) = 0.352(1/T) - 0.1588. \tag{4.6}$$

The plot of surface porosity versus S_u and S_y is presented in Figure 16. Both S_y and S_u decrease linearly by increasing surface porosity. Since surface porosity may not be a quantitative indicator of the volume porosity in the DMLS-manufactured sheets, these equations can be only used to provide an estimation for S_y and S_u variation based on surface porosity measurements.

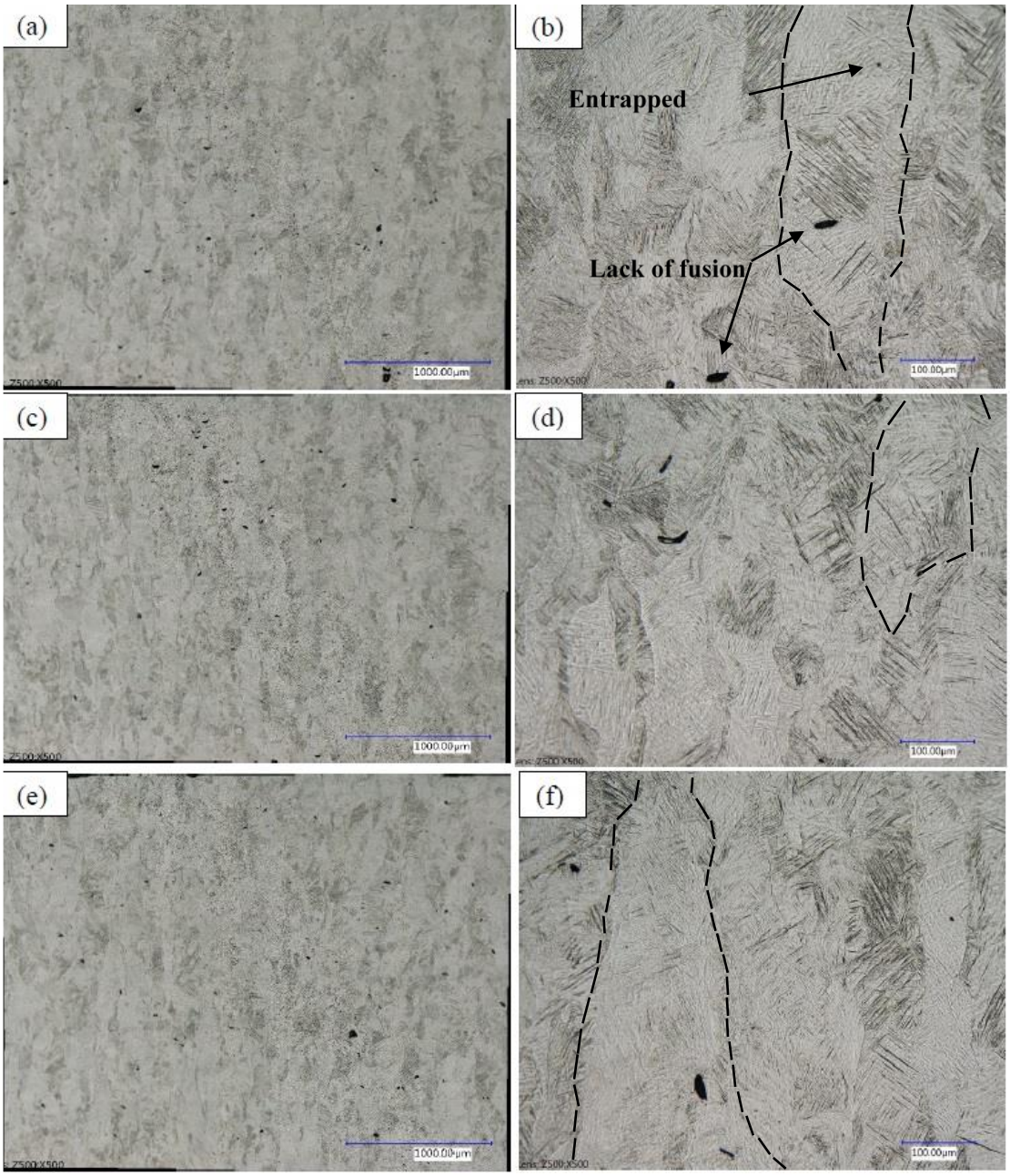

Figure 14. Optical images of DMLS-manufactured sheets with thickness of 0.5 mm at different heights, (a,b) 7 mm, (c,d) 37 mm, (e,f) 82 mm.

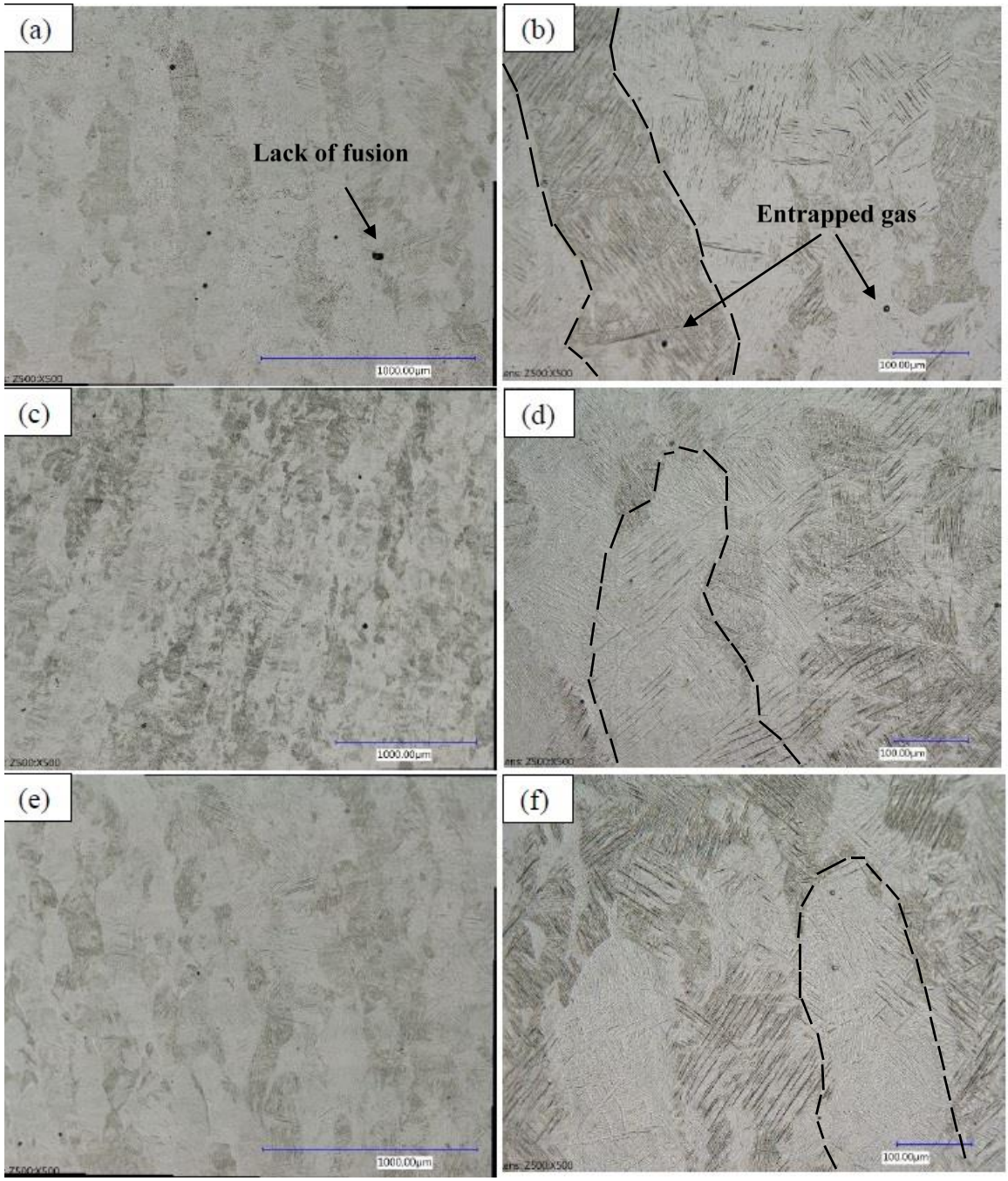

Figure 15. Optical images of DMLS-manufactured sheets with thickness of 1.6 mm at different heights, (a,b) 7 mm, (c,d) 37 mm, (e,f) 82 mm.

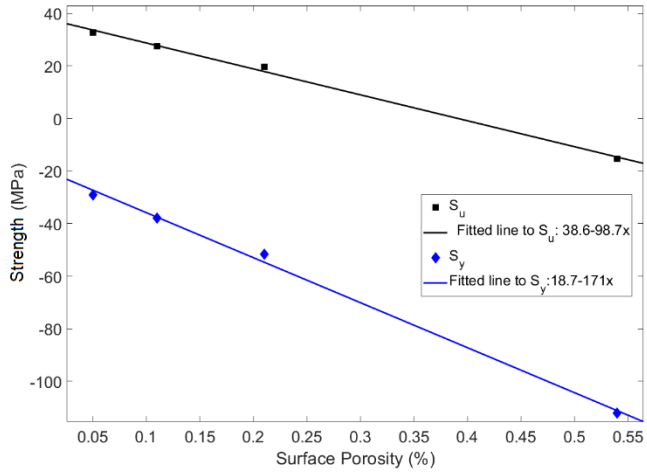

Figure 16. Variation of Su and Sy versus surface porosity. Surface porosity variation is due to the change in the thickness of the sheets (Eq.4.6).

The variations of S_u and S_y and elongation at break with respect to the orientation (θ) are presented in Figure 17(a) and Figure 17(b), respectively, by averaging the variation of these quantities for all the five specimens (G-1 to G-5). Since the variations of S_y and S_u with respect to G/T ratio is linear, their average variation with respect to θ provides the variation of all the specimens with θ. A reverse correlation between the variation of elongation at break and tensile strength is observed in accordance with the previously observed behavior for martensitic materials; i.e. as S_y and S_u increase/decrease, elongation at break decreases/increases [32,33]. Moreover, the specimens cut in 30°-45° orientations have the highest S_y and S_u while having the lowest elongation at break. Perhaps, this behavior can be explained as the competition between two factors in the DMLS process. One factor is related to the existence of lack of fusion (LOF) and entrapped gas defects; see Figure 14 and Figure 15. While the entrapped gas defects are spherical or semi-spherical, LOFs have sharp edges and elongated at the direction of the layers and perpendicular to the build direction (shown by z-axis on Figure 14 and Figure

15) due to the layer-wise nature of the DMLS [34,35]. Figure 18 shows the SEM images of a 0.5 mm-thick sheet at the height of 7 mm to illustrate the LOF and entrapped gas defects. Therefore, LOF act as the crack initiation sites under tension [36], making the horizontal plane (vertical specimens) as the orientation, perpendicular to which the weakest specimens lay, and the vertical plane (horizontal specimen) as the orientation related to the strongest specimens. The other factor is concerned with the prior β grain morphology; see Figure 14 and Figure 15. Prior β grains are elongated in the z-direction, wherein martensite is formed inside of each grain due to the high cooling rates during the DMLS [22]. Since there is a direct relationship between the width of the prior β grains and tensile strength of Ti-6Al-4V alloy [37], S_u and S_y have the maximum values for the vertical specimens and the minimum values for the horizontal ones, only considering the β grain morphology. Therefore, the competition between the LOF orientation factor and the β grain morphology results in the observed trend in Figure 17.

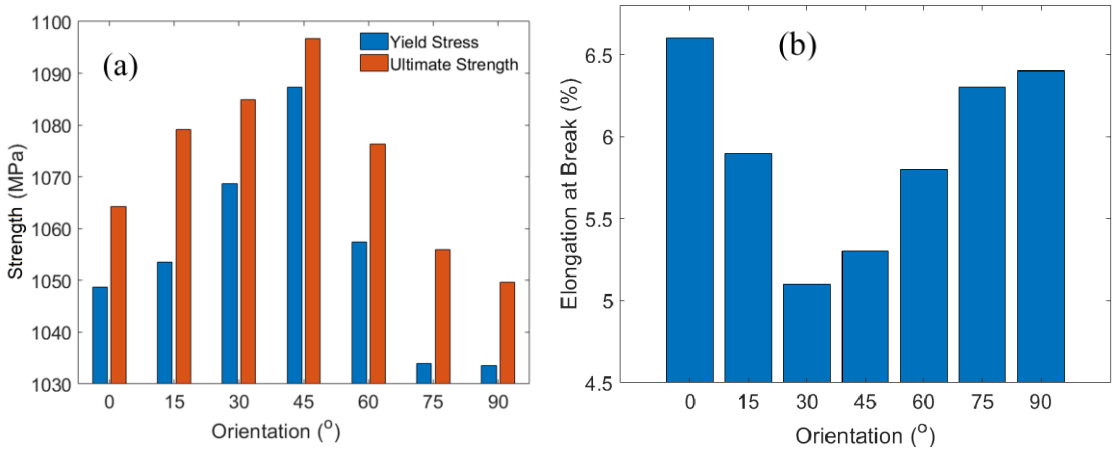

Figure 17. (a) Tensile strength and (b) Elongation at break of DMLS-manufactured samples cut in different orientations with respect to the build platform.

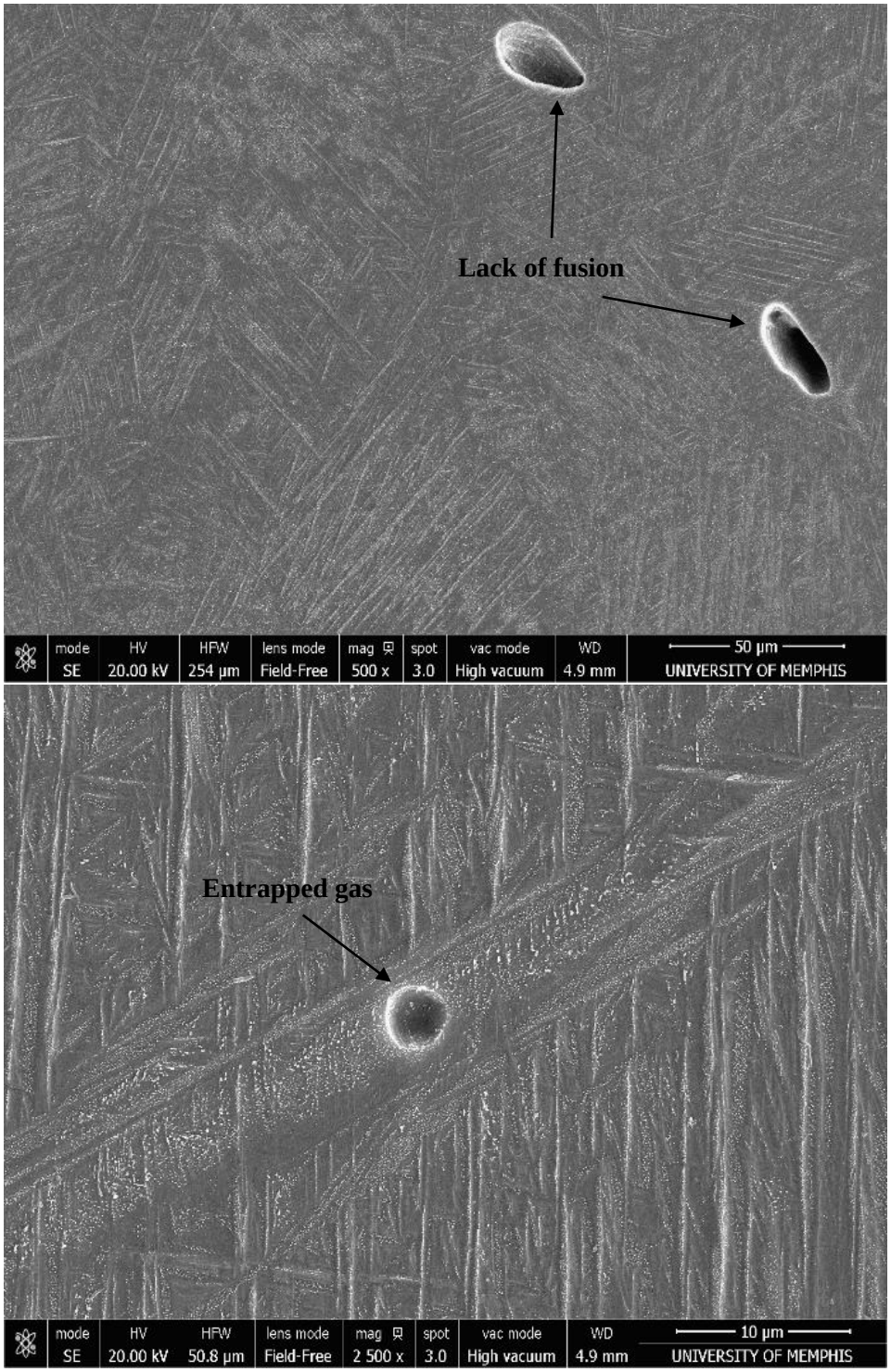

Figure 18. SEM images of 0.5 mm sheet at the height of 7 mm showing different types of defects.

4.4.2.2 Effect of Height

Figure 19 shows the variations of S_u and S_y versus height for G-1 to G-5 specimens cut horizontally ($\alpha = 0°$) at different heights. Regardless of the thickness of the sheets, both S_y and S_u slightly decrease to a minimum value, around the height of 20-30 mm and then slightly increase to the height of 40-50 mm followed by more severe decrement with the further increment of the height.

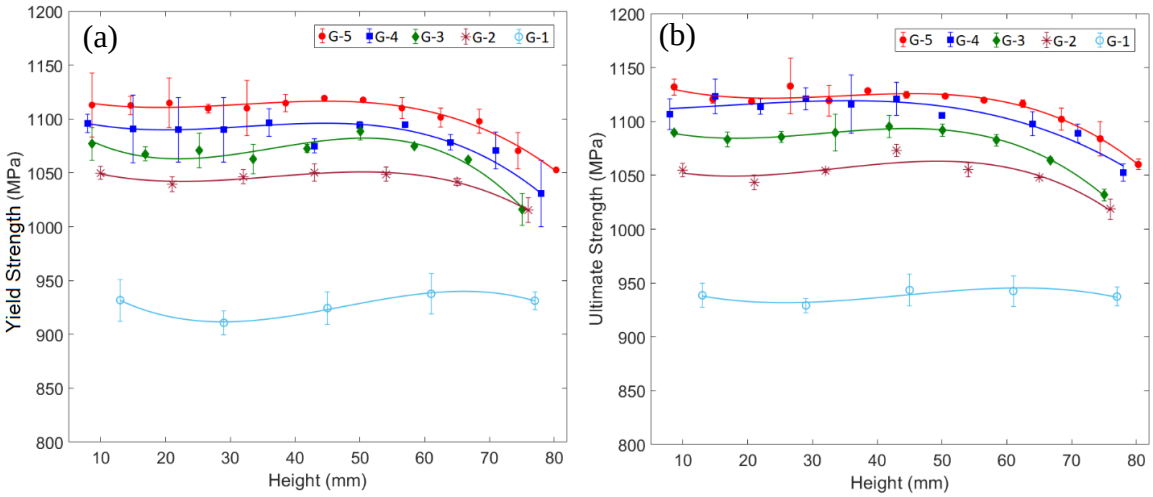

Figure 19. Variations of (a) Sy and (b) Su versus the height of DMLS-manufactured sheets.

The observed trends for Su and Sy variations versus height may be explained by investigating the variations of surface porosity and prior β grain width versus height similar to the discussion presented for the results showed in Figure 17. The average surface porosity (the last row of Table 12) slightly increases by the height variation from 7 mm to 37 mm followed by a more severe increment for the height of 82 mm that is consistent with the trend observed for the S_y and S_u variations. As it was mentioned in the prior discussions, porosity increment is associated with the overheating during the DMLS process. In this case, as the height increases, the distance from the build platform as the

heat sink for major conduction cooling mechanism increases. Therefore, because of the lower cooling rates at higher heights, the current layer has a higher temperature when the next layer is scanned, causing the overheating of the layer, thus increased porosities. It should be noted that this problem can be compensated for by decreasing the energy input of the DMLS process for higher heights or increasing the dwell time between the scanning of consecutive layers.

Table 12. Surface porosity of DMLS-manufactured sheets at different heights.

Thickness	Height		
	7 mm	37 mm	82 mm
0.5 mm	0.48 %	0.54 %	0.91 %
1.0 mm	0.18 %	0.21 %	0.25 %
1.3 mm	0.06 %	0.11 %	0.09 %
1.6 mm	0.12 %	0.05 %	0.11 %
Average	$0.21_{\pm 0.002}$	$0.23_{\pm 0.002}$	$0.34_{\pm 0.0034}$

The prior β grain width was measured for all of the optical images presented in Figure 14 and Figure 15, and their variations with respect to the height are presented in Figure 20. The average prior β grain width remains constant to the height of 37 mm followed by a significant increment to the height of 82 mm. The increment of prior β grain width with height has been reported previously for electron beam-manufactured Ti-6Al-4V rectangular plates [37]. Therefore, the cumulative effect of the surface porosity and variation in prior β grain width explains the trend observed in Figure 19 for S_y and S_u variations versus height. In the end, it is also interesting to discuss the build platform temperature variation with respect to the current height of the sheets (manufacturing time). Although the build platform temperature was set at 37 °C for the DMLS of the

sheets, the build platform temperature rapidly raised to about 48 °C due to the inserted energy by the laser beam. This variation of the build platform temperature confirms that the most significant cooling mechanism of the parts during the DMLS process is cooling through the build platform as it has been widely reported in the literature [31]; the build platform temperature increment may be avoided by increasing the dwell time as it was mentioned previously. However, the build platform temperature was gradually decreased to about 43 °C after reaching the height of about 40 mm and it remained constant till the end of the process. This behavior suggests that the heat conduction/convection to the surrounding powder increases as the lateral surface of the sheets increases and the heat conduction to the build platform takes longer, where both of them are caused by increasing the height of the sheets. Thus, larger portions of the heat dissipate through the conduction/convection of the side surfaces of the sheets changing the major cooling direction from perpendicular to the build platform to a slightly inclined angle. Since the prior β grains are expected to elongate in the cooling direction, these grains will be elongated in angles smaller than 90° increasing the width of the grains for horizontal specimens at higher heights. Adding to this matter is the formation of larger prior β grains at higher heights due to slower cooling rates that justifies the measurements presented in Figure 20 for the variation of prior β grains width with the variation of height.

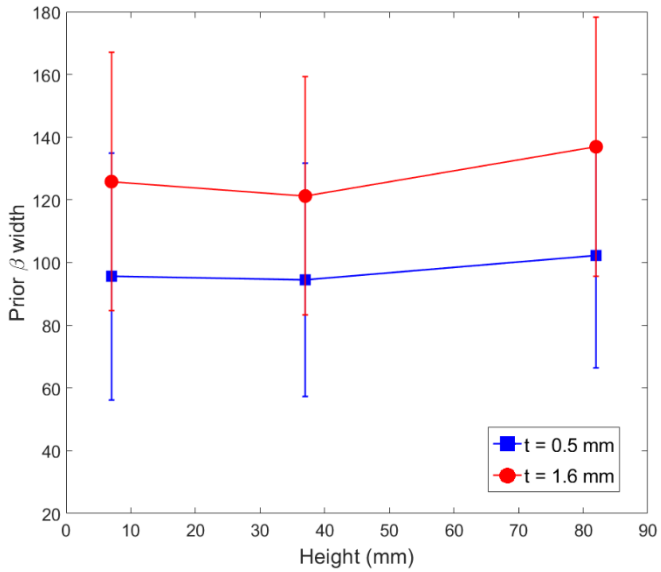

Figure 20. Prior β grain width variation versus height in DMLS-manufactured Ti-6Al-4V sheets.

The variations of microhardness versus the height of the DMLS-manufactured Ti-6Al-4V sheets with thicknesses of 0.5 mm, 1.0 mm, 1.3 mm, and 1.6 mm were presented in Figure 10. The microhardness of DMLS-manufactured sheets varies in 357 to 387 HV (kg/mm^2) range depending on the thickness and the height of the sheet, while the microhardness values of traditionally manufactured sheets are independent of the sheet thickness and location and are measured as 316.5 HV (kg/mm^2). Observation of higher microhardness values for DMLS-manufactured Ti-6Al-4V with martensitic microstructure compared to traditionally manufactured sheets with α+β microstructure is consistent with previous findings in the literature [38,39]. For DMLS-manufactured sheets, microhardness variations by increasing the height show a similar trend as the variations of S_y and S_u with height (Figure 19), while microhardness decreases by increasing the thickness of the sheets in contradiction for the trend observed for S_y and S_u (Figure 10).

The microhardness variations cannot be directly correlated to the variation of the prior β grain width or surface porosity because of the indentation size length scale difference with these features [40]. Rather the microhardness variation may be attributed to the decomposition of α′ to α and β, increasing the size of β nanoparticles, and/or the formation of soft orthorhombic α″ during the DMLS process. The SEM images of the samples cut out from heights of 7 mm, 37 mm, and 82 mm from DMLS-manufactured Ti-6Al-4V sheets with thicknesses of 0.5 mm and 1.6mm are presented in Figure 21. The martensite α′ consisting of primary α′, secondary α′, and tertiary α′ is the dominant phase during the solidification. The nanoparticles that can be seen in these figures are inferred as the β phase nanoparticles [41]. Comparing the left and right images in each row of this figure, the formation of more β nanoparticles for the thinner sheet and its increment by increasing the height are observed. Table 13 shows the measured β surface fraction of these images for a quantitative comparison. β nanoparticles surface fraction is significantly higher in the 0.5 mm-thick sheet compared to the 1.6 mm-thick one. Therefore, increasing the volume fraction of β nanoparticles results in increasing the microhardness in accordance with prior findings for the effect of β volume fraction on the microhardness of Ti-6Al-4V alloy [40].

Table 13. β surface fraction at different heights of two sheets with different thicknesses

Thickness	Height		
	7 mm	37 mm	82 mm
0.5 mm	10.55 %	12.24 %	12.78 %
1.6 mm	1.49 %	1.63 %	11.34 %

Increasing the height from 7 mm to 37 mm for the 1.6 mm-thick sheet results in a slight change of the microstructure consisting of α′ and β nanoparticles distributed between the α′ laths. However, increasing the height to 82 mm results in the formation of large amounts of β nanoparticles; this is more severe in the thicker sheet. However, the increment of the β nanoparticles surface fraction inversely correlates with the microhardness despite our observation for sheets with different thicknesses. This phenomenon may be attributed to the decomposition of α′ to α and β and/or the formation of soft orthorhombic α″ phase during slower cooling [42]. Formation of soft orthorhombic α″ has been found to decrease hardness in martensitic Ti-6Al-4V alloy during the heat treatment [43]. The same group also observed decreasing the microhardness in spite of increment in the β volume fraction. They identified decreasing concertation of vanadium in the β phase during the cooling as the cause of transformation to soft orthorhombic α″. However, detecting the precipitation of α″ is a very challenging task by the transition electron microscopy (TEM) and also not detectable by X-ray diffraction (XRD) due to their low concentration [42].

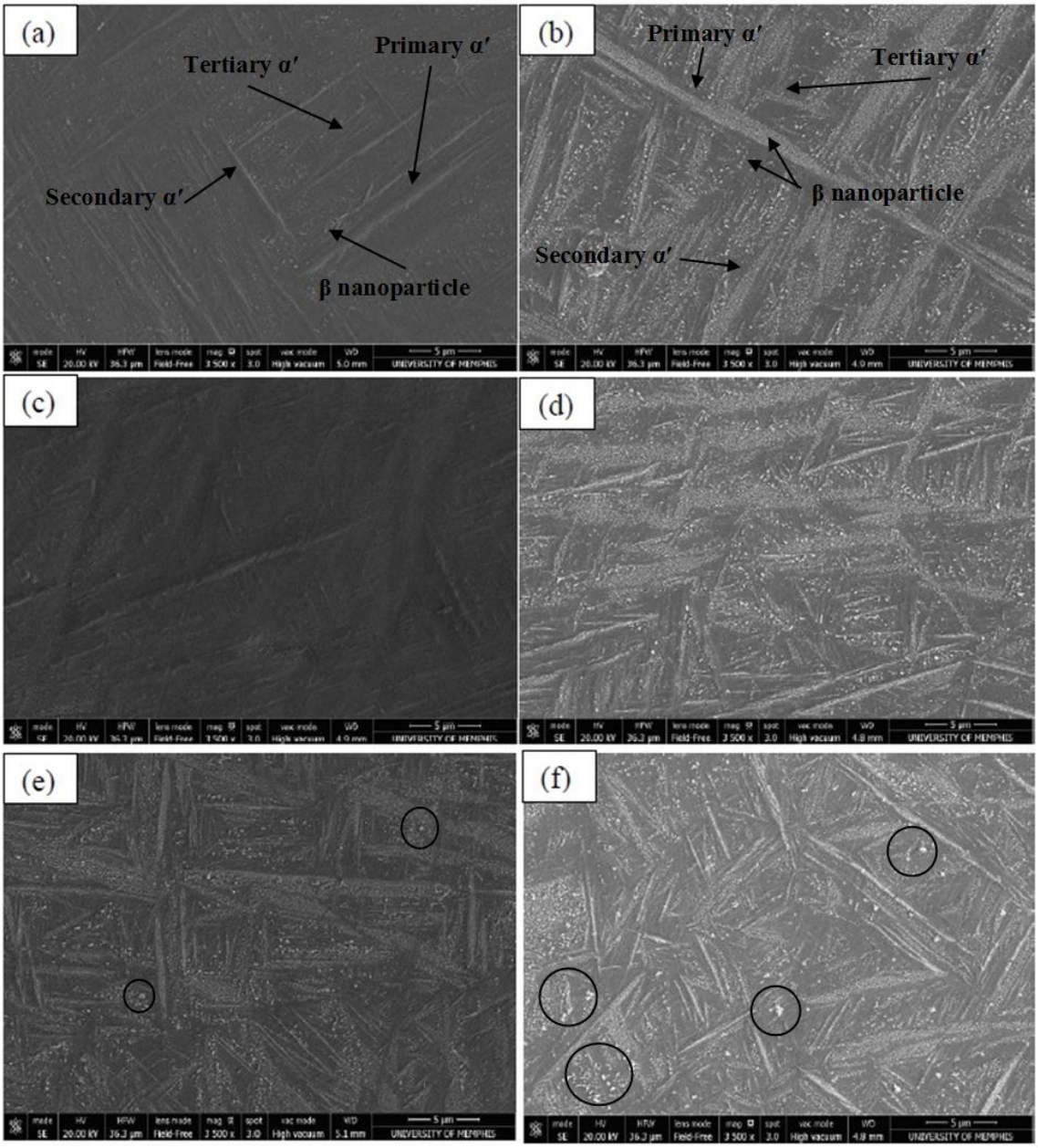

Figure 21. SEM images for samples cut from heights of 7 mm, 37 mm, and 82 mm from DMLS-manufactured Ti-6Al-4V sheets with thicknesses of (a,c,e) the 0.5 mm and (b,d,f) the 1.6 mm.

To further understand the decomposition of α′ to α and β, the oxygen content variation versus height in DMLS-manufacturing of Ti-6Al-4V sheets is measured (Figure 22). The oxygen content is increasing exponentially with the height perhaps due to longer

exposure of the material at high temperature to a low amount of Oxygen in the Argon inert gas (100-150 ppm) due to slower cooling and overheating at higher heights. Since Oxygen is α stabilizer, more α and less β nanoparticles are formed at higher heights during the decomposition of α′ which results in the microhardness decrement with the height increment [40].

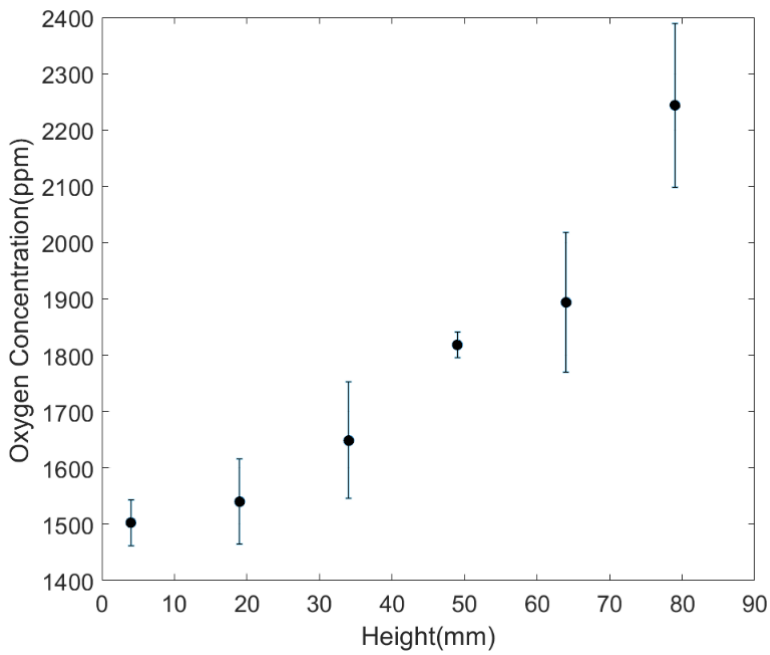

Figure 22. Oxygen content variation versus height in DMLS-manufacturing of Ti-6Al-4V sheets.

4.4.2.3 Effect of Distance from the Edge

The yield stress and ultimate tensile strength of G-2, G-3, and G-5 specimens cut vertically (α = 90°) at different distances from the free edges are plotted in Figure 23. The results show insignificant variations of both S_y and S_u with respect to their distance from the edges. This behavior is expected for DMLS-manufactured sheets as the thermal history of the material has an insignificant variation with the distance from the edges, i.e.

heat conduction to the build platform and convection through the side free surfaces are uniform at each layer except at the vicinity of the edges.

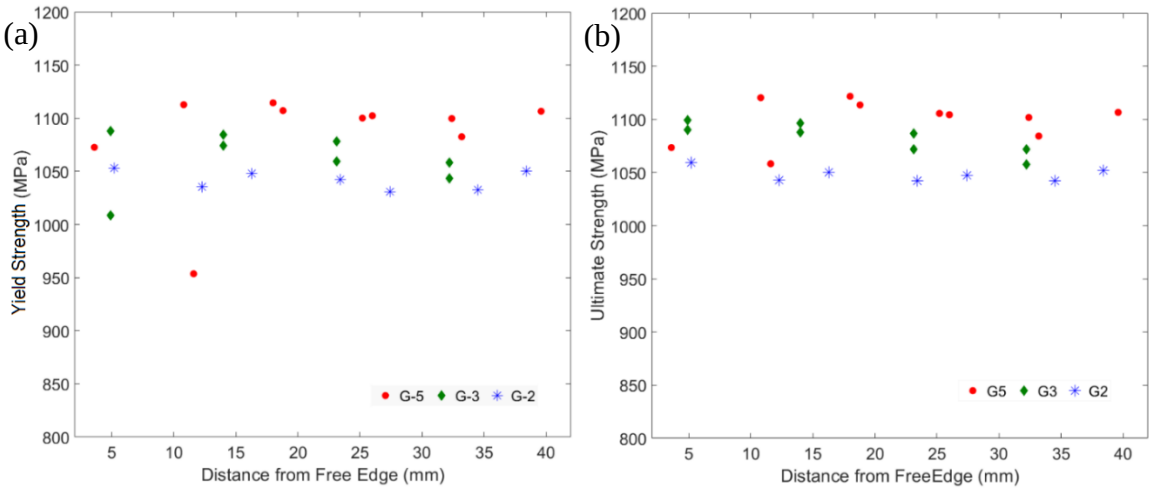

Figure 23. Variations of (a) Sy and (b) Su versus the distance from free edge of DMLS-manufactured Ti-6Al-4V sheets.

4.5 Conclusion

The effect of thickness, orientation, distance from free edges, and height on tensile mechanical properties and microhardness of DMLS-manufactured sheets and their correlation to material microstructure and thermal history as dictated by DMLS process parameters are investigated. More than 300 mechanical tensile tests were performed to provide statistically meaningful conclusions about the variations of these properties. By studying the traditionally manufactured sheets, we proposed a model to describe and isolate the effect of specimen geometry from the effect of the material/manufacturing process on the mechanical properties of Ti-6Al-4V sheets that is further used in the study of DMLS-manufactured sheets, leading to the following conclusions:

- Both S_y and S_u monotonically decrease by increasing the G/T ratio for all the orientations. The material-dependent variation of S_y and S_u for DMLS-

manufactured sheets are derived using the geometry-dependent behavior of traditionally manufactured sheets.

- Porosity is increased with decreasing the sheet thickness, due to lower cooling rates and accumulation of more heat in the thinner sheets, causing gas trapped porosity due to overheating.
- Testing specimens in different orientations resulted in obtaining a trend in the values of S_u and S_y that is an increase from 0° to 30°-45° and then a decrease with more increasing the orientation angle from 45° to 90° such that the highest and lowest values of S_u and S_y were at 30°-45° and 90°, respectively. Moreover, the maximum and minimum elongations at break found to be for the specimens cut at 0° and 30°-45°, respectively. This behavior is attributed to the competition between two factors in the DMLS process, namely the defect orientation factor and the β grain width factor.
- The variations of S_u and S_y versus height showed that regardless of the thickness of the sheets, both S_y and S_u slightly decrease and then slightly increase to the height of 40-50 mm followed by more severe decrement with the further increment of the height. This behavior is attributed to the increase in the porosity and prior β grain width with increasing height, which is affected by cooling mechanisms of the sheets during the process.
- Tensile testing of the samples cut vertically (90°) by different distances from the free edge showed that the distance from the free edge has no significant effect on the mechanical properties of the DMLS-manufactured thin sheets since the

heat conduction to the build platform and convection through the side of the free surfaces are uniform at each layer.

- Microhardness variations by increasing the height show a similar trend as the variations of S_y and S_u with height, while microhardness decreases by increasing the thickness of the sheets in contradiction with the trend observed for S_y and S_u. The variation of microhardness is attributed to the decomposition of α′ to α and β, increasing the size of β nanoparticles, and/or the formation of the soft orthorhombic α″ during the DMLS process.
- The oxygen content is increasing exponentially with the height due to longer exposure of the material at high temperature to a low amount of Oxygen in the Argon inert gas (100-150 ppm) because of the slower cooling rates at higher heights.

Acknowledgments

This material is based upon work under a Master Service Agreement sponsored by Medtronic Sofamor Danek USA, Inc.

References

[1] M. Seabra, J. Azevedo, A. Araújo, L. Reis, E. Pinto, N. Alves, R. Santos, J. Pedro Mortágua, Selective laser melting (SLM) and topology optimization for lighter aerospace componentes, Procedia Struct. Integr. 1 (2016) 289–296. doi:10.1016/J.PROSTR.2016.02.039.

[2] M. Attaran, The rise of 3-D printing: The advantages of additive manufacturing over traditional manufacturing, Bus. Horiz. 60 (2017) 677–688. doi:10.1016/J.BUSHOR.2017.05.011.

[3] S. Ozden, R. Ekici, F. Nair, Investigation of impact behaviour of aluminium based SiC particle reinforced metal–matrix composites, Compos. Part A Appl. Sci. Manuf. 38 (2007) 484–494. doi:10.1016/J.COMPOSITESA.2006.02.026.

[4] M. Braian, D. Jönsson, M. Kevci, A. Wennerberg, Geometrical accuracy of metallic objects produced with additive or subtractive manufacturing: A comparative in vitro study, Dent. Mater. 34 (2018) 978–993. doi:10.1016/j.dental.2018.03.009.

[5] B.E. Carroll, T.A. Palmer, A.M. Beese, Anisotropic tensile behavior of Ti-6Al-4V

components fabricated with directed energy deposition additive manufacturing, Acta Mater. 87 (2015) 309–320. doi:10.1016/j.actamat.2014.12.054.

[6] N. Shamsaei, A. Yadollahi, L. Bian, S.M. Thompson, An overview of Direct Laser Deposition for additive manufacturing; Part II: Mechanical behavior, process parameter optimization and control, Addit. Manuf. 8 (2015) 12–35. doi:10.1016/J.ADDMA.2015.07.002.

[7] E.M. Odom, D.F. Adams, Specimen size effect during tensile testing of an unreinforced polymer, J. Mater. Sci. 27 (1992) 1767–1771. doi:10.1007/BF01107202.

[8] T. Tsuchiya, O. Tabata, J. Sakata, Y. Taga, Specimen size effect on tensile strength of surface-micromachined polycrystalline silicon thin films, J. Microelectromechanical Syst. 7 (1998) 106–113. doi:10.1109/84.661392.

[9] D. Kiener, W. Grosinger, G. Dehm, R. Pippan, A further step towards an understanding of size-dependent crystal plasticity: In situ tension experiments of miniaturized single-crystal copper samples, Acta Mater. 56 (2008) 580–592. doi:10.1016/J.ACTAMAT.2007.10.015.

[10] Y.H. Zhao, Y.Z. Guo, Q. Wei, T.D. Topping, A.M. Dangelewicz, Y.T. Zhu, T.G. Langdon, E.J. Lavernia, Influence of specimen dimensions and strain measurement methods on tensile stress–strain curves, Mater. Sci. Eng. A. 525 (2009) 68–77. doi:10.1016/J.MSEA.2009.06.031.

[11] A.V. Sergueeva, J. Zhou, B.E. Meacham, D.J. Branagan, Gage length and sample size effect on measured properties during tensile testing, Mater. Sci. Eng. A. 526 (2009) 79–83. doi:10.1016/J.MSEA.2009.07.046.

[12] D.S. Gianola, C. Eberl, Micro- and nanoscale tensile testing of materials, JOM. 61 (2009) 24–35. doi:10.1007/s11837-009-0037-3.

[13] J.K. Algardh, T. Horn, H. West, R. Aman, A. Snis, H. Engqvist, J. Lausmaa, O. Harrysson, Thickness dependency of mechanical properties for thin-walled titanium parts manufactured by Electron Beam Melting (EBM)®, Addit. Manuf. 12 (2016) 45–50. doi:10.1016/J.ADDMA.2016.06.009.

[14] S. Miyazaki, K. Shibata, H. Fujita, Effect of specimen thickness on mechanical properties of poltcrystalline aggregated with various grain sizes, Acta Metall. 27 (1978) 855–862.

[15] N. Kashaev, M. Horstmann, V. Ventzke, S. Riekehr, N. Huber, Comparative study of mechanical properties using standard and micro-specimens of base materials Inconel 625, Inconel 718 and Ti-6Al-4 v, J. Mater. Res. Technol. 2 (2013) 43–47. doi:10.1016/j.jmrt.2013.03.003.

[16] D.R. Malpally, Uncertainty Analysis of Mechanical Properties From Miniature Tensile Testing of High Strengh Steels, 2014.

[17] F. Hajy Akbary, M.J. Santofimia, J. Sietsma, Elastic Strain Measurement of Miniature Tensile Specimens, Exp. Mech. 54 (2014) 165–173. doi:10.1007/s11340-013-9785-7.

[18] B. Strndel, J. Brumek, Effect of Tensile Test Spcimene Size on Ductility of R7T Steel, Metal. 5 (2013) 2–7.

[19] K. Kumar, A. Pooleery, K. Madhusoodanan, R.N. Singh, J.K. Chakravartty, B.K. Dutta, R.K. Sinha, Use of miniature tensile specimen for measurement of mechanical properties, Procedia Eng. 86 (2014) 899–909. doi:10.1016/j.proeng.2014.11.112.

[20] K. Kumar, A. Pooleery, K. Madhusoodanan, R.N. Singh, A. Chatterjee, B.K. Dutta, R.K. Sinha, Optimisation of thickness of miniature tensile specimens for evaluation of mechanical properties, Mater. Sci. Eng. A. 675 (2016) 32–43. doi:10.1016/j.msea.2016.08.032.

[21] D. Foehring, H.B. Chew, J. Lambros, Characterizing the tensile behavior of additively manufactured Ti-6Al-4V using multiscale digital image correlation, Mater. Sci. Eng. A. 724 (2018) 536–546. doi:https://doi.org/10.1016/j.msea.2018.03.091.

[22] J.W.N. S. Karnati, I. Axelsen, F. F. Liou, Investigation of Tensile Properties of Bulk and Slm Fabricated 304L Stainless Steel Using Various Gage Length Specimens, Solid Free. Fabr. (2016) 13.

[23] Standard Test Methods for Tension Testing of Metallic Materials, Annual boo, A. S. T. M., 2004.

[24] H. Wei, G.D. Hibbard, G. Palumbo, U. Erb, The effect of gauge volume on the tensile properties of nanocrystalline electrodeposits, Scr. Mater. 57 (2007) 996–999. doi:10.1016/J.SCRIPTAMAT.2007.08.008.

[25] A.C. Mackenzie, J.W. Hancock, D.K. Brown, On the influence of state of stress on ductile failure initiation in high strength steels, Eng. Fract. Mech. 9 (1977) 167–188. doi:10.1016/0013-7944(77)90062-5.

[26] J.W. Liu, Q.P. Cao, L.Y. Chen, X.D. Wang, J.Z. Jiang, Shear band evolution and hardness change in cold-rolled bulk metallic glasses, Acta Mater. 58 (2010) 4827–4840. doi:10.1016/J.ACTAMAT.2010.05.018.

[27] M. Stolpe, J.J. Kruzic, R. Busch, Evolution of shear bands, free volume and hardness during cold rolling of a Zr-based bulk metallic glass, Acta Mater. 64 (2014) 231–240. doi:10.1016/J.ACTAMAT.2013.10.035.

[28] B. Vrancken, L. Thijs, J.P. Kruth, J. Van Humbeeck, Microstructure and mechanical properties of a novel β titanium metallic composite by selective laser melting, Acta Mater. 68 (2014) 150–158. doi:10.1016/j.actamat.2014.01.018.

[29] L. Thijs, F. Verhaeghe, T. Craeghs, J. Van Humbeeck, J.-P. Kruth, A study of the microstructural evolution during selective laser melting of Ti–6Al–4V, Acta Mater. 58 (2010) 3303–3312. doi:10.1016/J.ACTAMAT.2010.02.004.

[30] G. Kasperovich, J. Haubrich, J. Gussone, G. Requena, Correlation between porosity and processing parameters in TiAl6V4 produced by selective laser melting, Mater. Des. 105 (2016) 160–170. doi:10.1016/J.MATDES.2016.05.070.

[31] I.A. Roberts, C.J. Wang, R. Esterlein, M. Stanford, D.J. Mynors, A three-

dimensional finite element analysis of the temperature field during laser melting of metal powders in additive layer manufacturing, Int. J. Mach. Tools Manuf. 49 (2009) 916–923. doi:10.1016/J.IJMACHTOOLS.2009.07.004.

[32] F. Li, Z. Wang, X. Zeng, Microstructures and mechanical properties of Ti6Al4V alloy fabricated by multi-laser beam selective laser melting, Mater. Lett. 199 (2017) 79–83. doi:10.1016/j.matlet.2017.04.050.

[33] L.Y. Chen, J.C. Huang, C.H. Lin, C.T. Pan, S.Y. Chen, T.L. Yang, D.Y. Lin, H.K. Lin, J.S.C. Jang, Anisotropic response of Ti-6Al-4V alloy fabricated by 3D printing selective laser melting, Mater. Sci. Eng. A. 682 (2017) 389–395. doi:10.1016/j.msea.2016.11.061.

[34] M. Simonelli, Y.Y. Tse, C. Tuck, Materials Science & Engineering A Effect of the build orientation on the mechanical properties and fracture modes of SLM Ti – 6Al – 4V, Mater. Sci. Eng. A. 616 (2014) 1–11. doi:10.1016/j.msea.2014.07.086.

[35] B. Fotovvati, N. Namdari, A. Dehghanghadikolaei, Fatigue performance of selective laser melted Ti6Al4V components: State of the art, Mater. Res. Express. 6 (2018) 12002.

[36] M. Simonelli, Y.Y. Tse, C. Tuck, Effect of the build orientation on the mechanical properties and fracture modes of SLM Ti-6Al-4V, Mater. Sci. Eng. A. 616 (2014) 1–11. doi:10.1016/j.msea.2014.07.086.

[37] D.A. Hollander, M. Walter, T. Wirtz, R. Sellei, B. Schmidt-Rohlfing, O. Paar, H.-J. Erli, Structural, mechanical and in vitro characterization of individually structured Ti–6Al–4V produced by direct laser forming, Biomaterials. 27 (2006) 955–963. doi:10.1016/J.BIOMATERIALS.2005.07.041.

[38] A. Khorasani, I. Gibson, M. Goldberg, G. Littlefair, On the role of different annealing heat treatments on mechanical properties and microstructure of selective laser melted and conventional wrought Ti-6Al-4V, Rapid Prototyp. J. 23 (2017) 295–304. doi:10.1108/RPJ-02-2016-0022.

[39] M. Shunmugavel, A. Polishetty, Microstructure and Mechanical Properties of Wrought and Additive Manufactured Ti-6Al-4 V Cylindrical Bars, Procedia Technol. 20 (2015) 231–236. doi:10.1016/J.PROTCY.2015.07.037.

[40] H. Sharma, D. Parfitt, A.K. Syed, D. Wimpenny, E. Muzangaza, G. Baxter, B. Chen, A critical evaluation of the microstructural gradient along the build direction in electron beam melted Ti-6Al-4V alloy, Mater. Sci. Eng. A. 744 (2019) 182–194. doi:10.1016/J.MSEA.2018.12.016.

[41] H. Ali, L. Ma, H. Ghadbeigi, K. Mumtaz, In-situ residual stress reduction, martensitic decomposition and mechanical properties enhancement through high temperature powder bed pre-heating of Selective Laser Melted Ti6Al4V, Mater. Sci. Eng. A. 695 (2017) 211–220. doi:10.1016/J.MSEA.2017.04.033.

[42] S.Q. Wu, Y.J. Lu, Y.L. Gan, T.T. Huang, C.Q. Zhao, J.J. Lin, S. Guo, J.X. Lin, Microstructural evolution and microhardness of a selective-laser-melted Ti–6Al–4V alloy after post heat treatments, J. Alloys Compd. 672 (2016) 643–652. doi:10.1016/J.JALLCOM.2016.02.183.

[43] Q. Huang, X. Liu, X. Yang, R. Zhang, Z. Shen, Q. Feng, Specific heat treatment of selective laser melted Ti–6Al–4V for biomedical applications, Front. Mater. Sci. 9 (2015) 373–381. doi:10.1007/s11706-015-0315-7.

Appendix

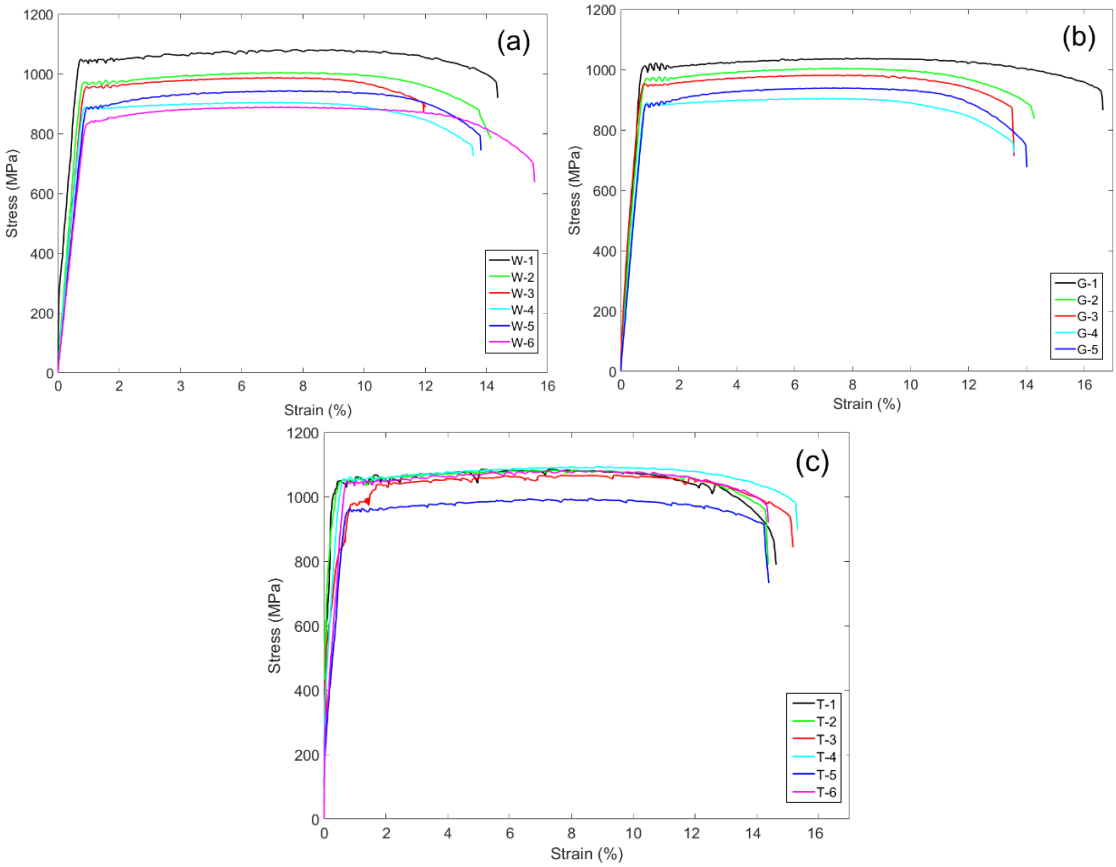

Figure 24 Stress-strain curves of traditionally manufactured Ti-6Al-4V sheets for specimens in (a) W=3.25 mm series, (b) G=20.98 mm series, (c) T=0.5 mm series.

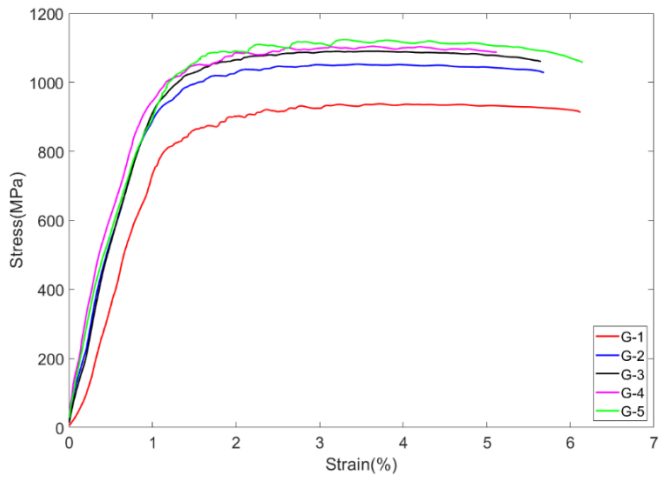

Figure 25 Stress-strain curves of DMLS-manufacture Ti-6Al-4V sheets of different sizes.

Each curve is an average of the related size in all the orientations.

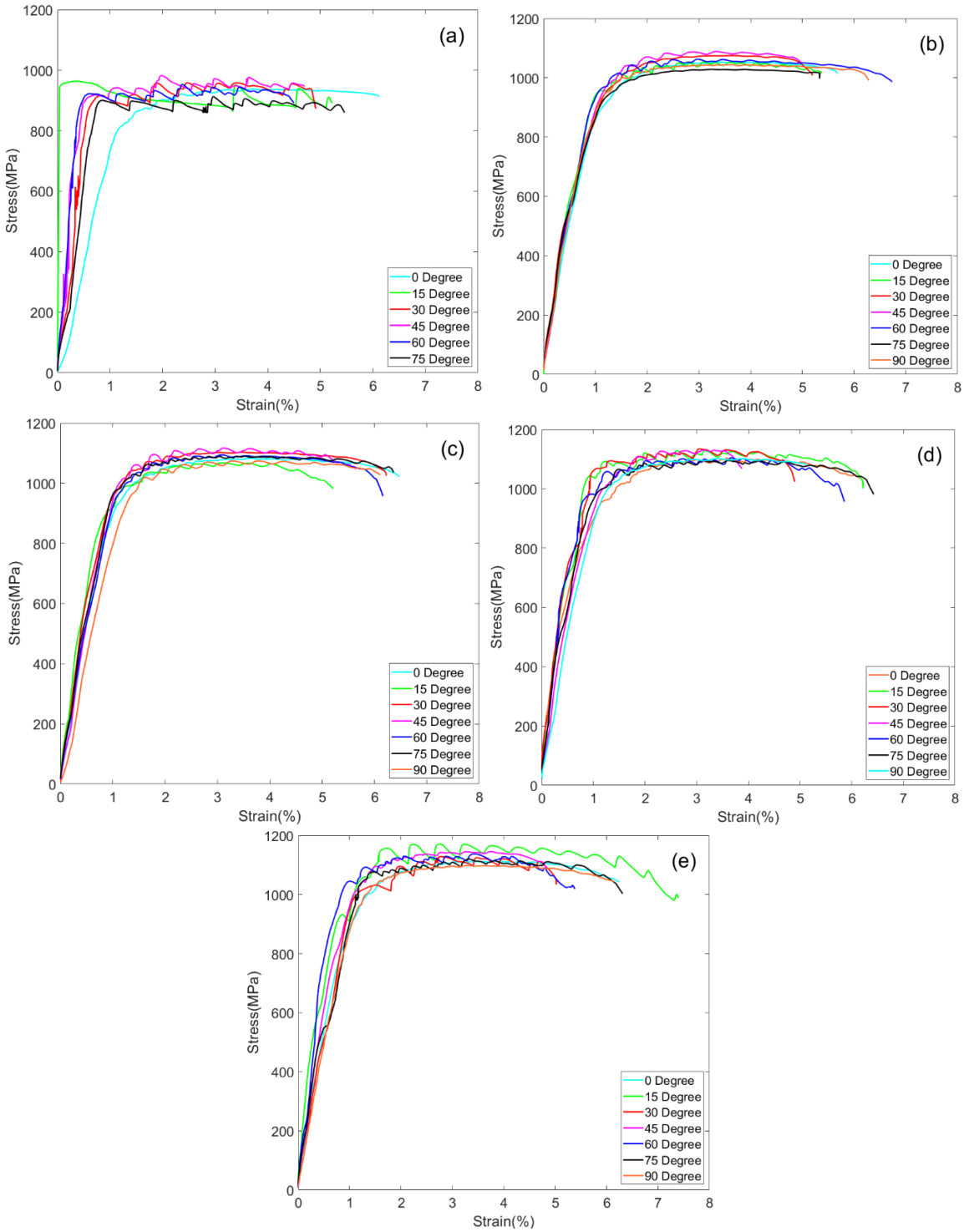

Figure 26 Stress-strain curves of DMLS-manufacture Ti-6Al-4V sheets: (a) G-2, (b) G-3, and (c) G-4 (d) G-5 cut in different orientations with respect to the build platform.

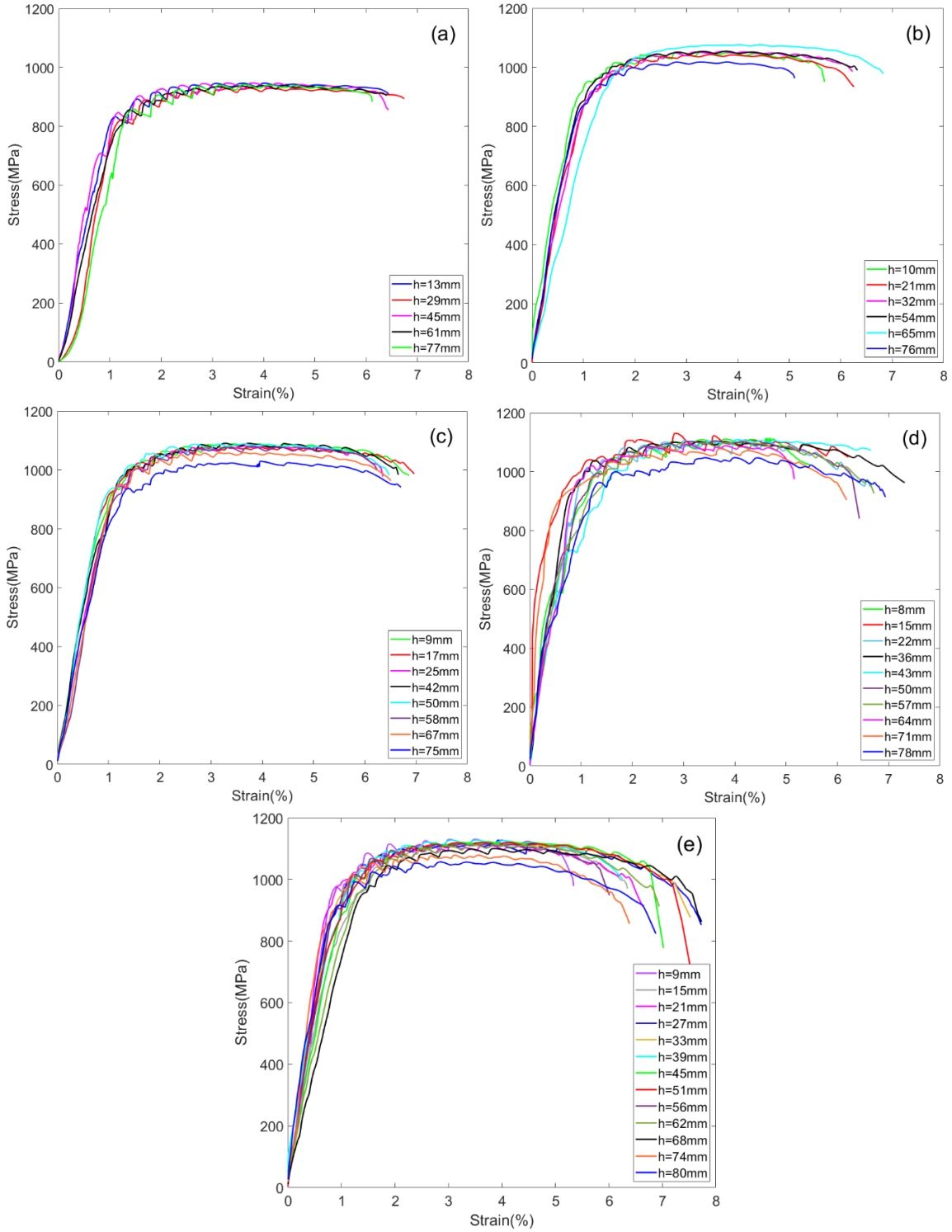

Figure 27 Stress-stress curves of horizontal samples of DMLS-manufacture Ti-6Al-4V sheets: (a) G-1, (b) G-2, (c) G-3, (d) G-4, and (e) G-5 cut at different heights.

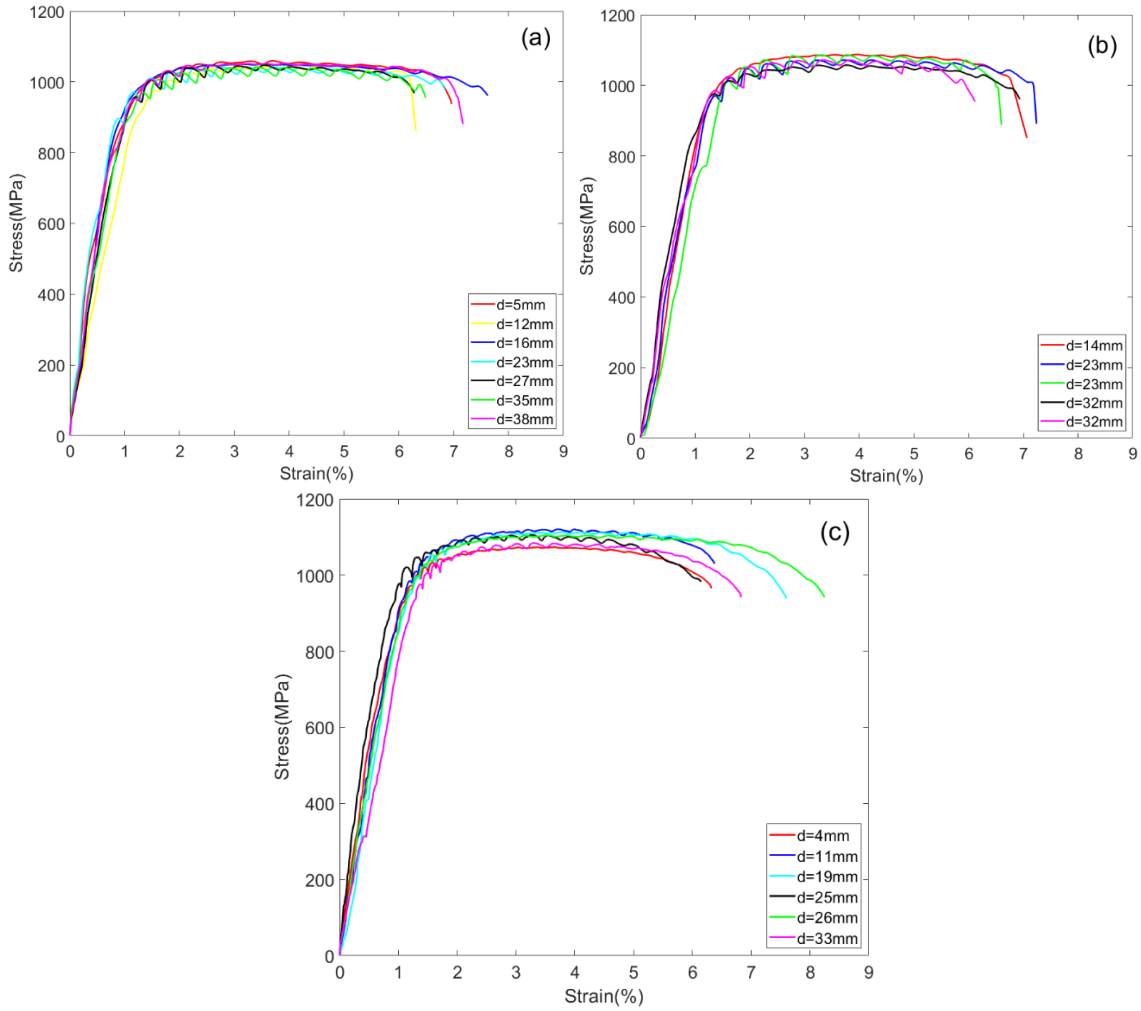

Figure 28 Stress-strain curves of vertical samples of DMLS-manufacture Ti-6Al-4V sheets: (a) G-2, (b) G3, and (c) G-5 cut from different distances from the sheet edge.

5. Application of Taguchi, Response Surface, and Artificial Neural Networks Toward Optimizing the Processing Parameters for Direct Metal Laser Sintering of Ti-6Al-4V Alloy

5.1 Introduction

Direct metal laser sintering (DMLS) is a widely adopted powder bed fusion (PBF) additive manufacturing (AM) methodology to manufacture high-performance metallic parts with complex geometries via selective laser scanning of thin layers of metal powders successively on top of each other. DMLS and other PBF methodologies offer extensive opportunities to alter the microstructure and subsequently to enhance the mechanical properties of the products by designing targeted processing strategies [1]. Unfortunately, the correlations between process parameters and the response are too complicated to fully understand, as DMLS is a multi-physics and multi-scale process, which includes thermo-mechanical coupling at the macroscale [2], laser-material interaction at the microscale [3], and melt-pool characteristics at the mesoscale [4]. Numerous research studies have been devoted to investigating the correlations between the DMLS process parameters and various properties of the fabricated parts such as surface quality, internal porosity, and mechanical performance [5–12]. Chen [13] categorized the AM modeling studies into empirical, analytical, and numerical models, along with machine learning techniques. There are more than 130 factors/process parameters affecting the quality of the manufactured parts in the DMLS process [14]. A full factorial design of experiment (DoE) consists of an equal number of replicates of all the possible combinations of the levels (values) of each of the factors (processing parameters) [15]. For instance, for five factors each having five levels, 5^5 or 3125

experiments are required for this method. The advantage of this approach is having the exact response for the effects of parameters and all of the combinations of their interactions [16]. However, conducting full factorial DoE to determine DMLS process parameters for novel materials is practically impossible due to the high costs and time of manufacturing these samples, characterizing them, and modeling the correlations between the characterization and the process parameters. Therefore, fractional factorial DoE methods are required to evaluate the most significant process variables and to optimize the performance of the products.

The Taguchi method with orthogonal arrays is one of the fractional factorial DoE methods that is a simple and powerful tool. It offers a systematic and efficient method to optimize designs for quality and cost [17]. Taguchi method has been employed to optimize the settings of the DMLS process parameters for various materials, such as SS316L [18,19], AlSi10Mg [20], CoCrMo [21], and pure Ti [21]. Jiang et al. [18] evaluated the effect of three factors, i.e., laser power, scanning speed, and hatch spacing, at three levels, on three properties, i.e., top surface roughness, hardness, and density of DMLS parts. They concluded that laser power is the most significant parameter affecting all the examined properties. While Calignano et al. [20] found scanning speed to have the greatest influence on the surface roughness of the components fabricated by the DMLS process. Although the reason for this difference in conclusions is unclear, it may be attributed to differences in materials, i.e., stainless steel and aluminum alloys, or differences in machines, i.e., EP250 and EOSINT M270, used for these experiments.

Response surface method (RSM) is another DoE technique to determine design factor settings to improve or optimize the performance or response of a process or

product. RSM combines the DoEs, regression analysis, and optimization methods to optimize the expected value of a stochastic response. RSM can be used with a full factorial DoE or fractional factorial DoE. However, a complete factorial DoE with a large number of factors requires a very large number of observations as explained before. Therefore, the reduction in size of a complete factorial experiment can be very helpful when more than three factors are contributing to a response in an experiment. This is where the fractional factorial design is useful. In this method, known design properties are utilized to selectively reduce the size of an experiment [22]. Read et al. [23] employed RSM to evaluate the best settings of laser power, scanning speed, hatch spacing, and scanning island size to optimize the porosity level of DMLS AlSi10Mg parts. They found the critical energy density point that gives the minimum pore fraction for this alloy to be 60 J/m^3. El-Sayed et al. [24] used RSM to propose the optimum process parameters, including laser power, scan speed, and hatch spacing, for Ti-6Al-4V medical implants applications and concluded that higher energy densities result in lower surface roughness and lower porosity levels. Gajera et al. [25] utilized Box-Behnken Design of RSM and established the relationship between DMLS process parameters and surface roughness values of CL50WS steel parts to compare two optimization algorithms, namely a genetic algorithm and JAYA. Bartolomeu et al. [26] manufactured Ti-6Al-4V samples by varying three processing parameters (laser power, scanning speed, and hatch spacing) at three levels in the DMLS process and utilized the RSM for the analysis of the experimental results, i.e., shear stress, hardness, and density. They obtained a quadratic model for each of the output properties and presented a response surface for them. They obtained relatively good adequacy for their models with the coefficient of determination

R^2 of 0.62 to 0.68. R^2 has values between 0 and 1 (the closer to 1, the better the prediction) and increases when other higher-order terms are added to the model. Hence, an adjusted R^2 is recommended as a criterion for the model adequacy. The adjusted R^2 for their models range from 0.55 to 0.61. Krishnan et al. [27] used a full factorial DoE on three levels of three factors, i.e., laser power, scanning speed, hatch spacing, to determine the most significant parameter influencing macroscopic properties of DMLS AlSi10Mg samples, and made the conclusion of hatch spacing being the most significant parameter, which influences the mechanical properties of parts. Using the same approach Pawlak et al. [28] achieved porosities less than 0.5% for AZ31 magnesium parts using the DMLS process.

Machine learning (ML) techniques are able to perform complex pattern recognition and regression analysis without constructing and solving the underlying physical models. This method is widely used in modeling, prediction, and analyzing the interaction of parameters in different industries such as manufacturing, aerospace, and biomedicine [29,30]. Among ML algorithms, artificial neural networks (ANNs), which are mathematical models mapping an input space to an output space, are the most extensively used techniques because of their strong computational power and sophisticated architectures [31]. The architecture of an ANN consists of three types of layers namely, an input layer, one or more hidden layers, and an output layer [32]. Each layer consists of nodes representing neurons in the human nervous system. Each node in any given layer in the network is connected to nodes in its adjacent layers. The strength of the connection between any two connected nodes is given by a numerical weight. Each node receives the weighted responses from its connected nodes and produces an aggregate response or

output based on an activation function. In addition, each node receives an external bias input with a connection weight (similar to the intercept in a linear equation). The optimal connection weights are determined by training the ANN iteratively to generate the actual output for a given input. The prediction error is expressed as a function of the network weight and the loss function is optimized in terms of the network weight during training. To avoid falling into localized errors/traps in calculating the network coefficients, i.e., weights and bios values, a test process must be performed using new data that are not used in training and validation stages. One of the most widely used training methods is back-propagation, in which gradients are computed iteratively for each layer using the mathematical chain rule [33]. Once the ANN is trained, it is capable of predicting the responses based on unseen input values. Many applications in manufacturing engineering successfully implemented the ANN methodology as a beneficial empirical modeling method. Khorasani et al. [34] implemented an ANN with three hidden layers having four, three, and two hidden nodes to predict a single response (output) of top surface roughness of Ti-6Al-4V parts based on the input parameters of laser power, scan speed, hatch spacing, scan pattern increment angle, and heat treatment (HT) condition, i.e, different HT temperatures and cooling times. According to their results, heat treatment condition, which is a post-process parameter, is the dominant factor in determining the top surface roughness of DMLS-manufactured parts. Furthermore, they concluded that higher energy densities (higher laser power and lower scan speed) result in parts with lower surface qualities. Akhil et al. [35] used an ANN with five hidden nodes in one hidden layer to extract image texture parameters from surface images and predict the top surface roughness of DMLS-fabricated Ti-6Al-4V parts.

The application of ML and ANN to AM has been mainly focused on real-time process monitoring; e.g. in-situ melt-pool monitoring [36,37], computational modeling of the process [38], defect recognition [39–41], in situ acoustic emission [42,43]. Also, ML and ANN are used to optimize certain AM process parameters based on the measurement of a property of the samples after fabrication; e.g. porosity [44], strain in shape memory alloys [45], and fatigue performance [46]. Nevertheless, all these studies, similar to DoEs based on Taguchi and RSM methods, are limited to a single target property for optimization based on the variation of few numbers of AM process parameters. Most notably, layer thickness has been precluded from the list of the DMLS processing parameters for optimization. However, the layer thickness is reported [47–50] as the most significant parameter in the DMLS process. Furthermore, there is a lack of comprehensive study to compare the optimization of DMLS processing parameters via Taguchi, RSM, and ANN methods. In this study, the five most influential parameters, i.e. laser power, scan speed, hatch spacing, layer thickness, and stripe width, are considered as the design factors for DMLS processing of Ti-6Al-4V alloy. In addition to microhardness and relative density, the following seven roughness parameters, i.e. three surface roughness and four line roughness parameters, are considered as the target properties for optimization of the DMLS processing parameters: top, upskin, and downskin surface roughness parameters, and upskin/downskin horizontal/vertical line roughness parameters. First, L_{25} Taguchi orthogonal arrays are used for DoE of DMLS processing parameters in five levels. Also, a fractional factorial DoE resulting in $1/125^{th}$ of the full factorial experiments are used for RSM and ANN optimizations of the processing parameters. Second, the correlations between the DMLS processing

parameters and the target properties are discussed and modeled extensively. Third, a multi-parameter multi-response optimization was implemented on nine equally-weighted responses. Finally, the sets of optimum processing parameters predicted by each method are determined and compared with each other.

5.2 Materials and methods

All the DMLS manufacturing of the Ti-6Al-4V samples and powder characterization were carried out in the Metal Additive Manufacturing Laboratory (University of Memphis, Memphis, TN, USA), where the temperature and humidity are kept constant at 23±3 °C and 30±5%, respectively. The Ti-6Al-4V powders were purchased from EOS. Since these powders recycled and re-used in the machine multiple times prior to this study, the physical and chemical characteristics of the used powders were determined to provide the conditions of the powders used in this study. First, a GilSonic UltraSiever GA-8 was used to determine the size distribution of the powders according to ASTM B214-16 as shown in Table 14. A Qualtech Hall Flow Meter was used to determine the flowability of 24.14 (s/50g) according to ASTM B213-17. A Qualtech Tap Density Meter was used to determine the tap density of 2.70 (g/cm^3) and apparent density of 2.36 (g/cm^3) according to ASTM B527-15 and ASTM B212-17, respectively. Figure 9 shows the surface morphology of these Ti-6Al-4V powders. Most powders have a spherical shape while fine satellites are attached to some of them due to prior DMLS process and/or their production process. There are also some voids on the surface of the powders, which are resulted from the atomization process during the manufacturing of powders. Following ASTM E1409-13, a Bruker G-8 Galileo was used to measure the oxygen (O), nitrogen (N), and hydrogen (H) contents of the powders as 1634±76 ppm, 168 ±17 ppm,

and 30±3 ppm, respectively. Moreover, a Bruker G-4 Icarus was used to measure the total carbon (C) content in the powders as 78±9 ppm according to ASTM E1941-16.

Table 14. Size distribution of as-received and used Ti-6Al-4V powders.

Particle Size (μm)	Weight (g/100g)
>60	0.25
≤60>53	1.85
≤53>45	10.92
≤45>38	34.42
≤38>32	29.05
≤32>25	13.56
≤25>20	5.77
≤20	3.57
Total Recovered	99.39
Average Size*	33.49±4.40

An EOS M290 machine was used for DMLS of Ti-6Al-4V samples under inert argon atmosphere with a 0.6 mbar differential pressure, a recoating blade speed of 150 mm/s, and a build platform temperature of 37 °C. The stripe scanning strategy with zero stripe overlaps and 67° layer-by-layer stripe rotation were used in all the DMLS processes. The laser power (*P*), scanning speed (*v*), hatch spacing (*h*), layer thickness (t), and stripe width (s) are the DMLS parameters, effects of which on surface roughness, density, and microhardness of the manufactured parts are investigated in this study.

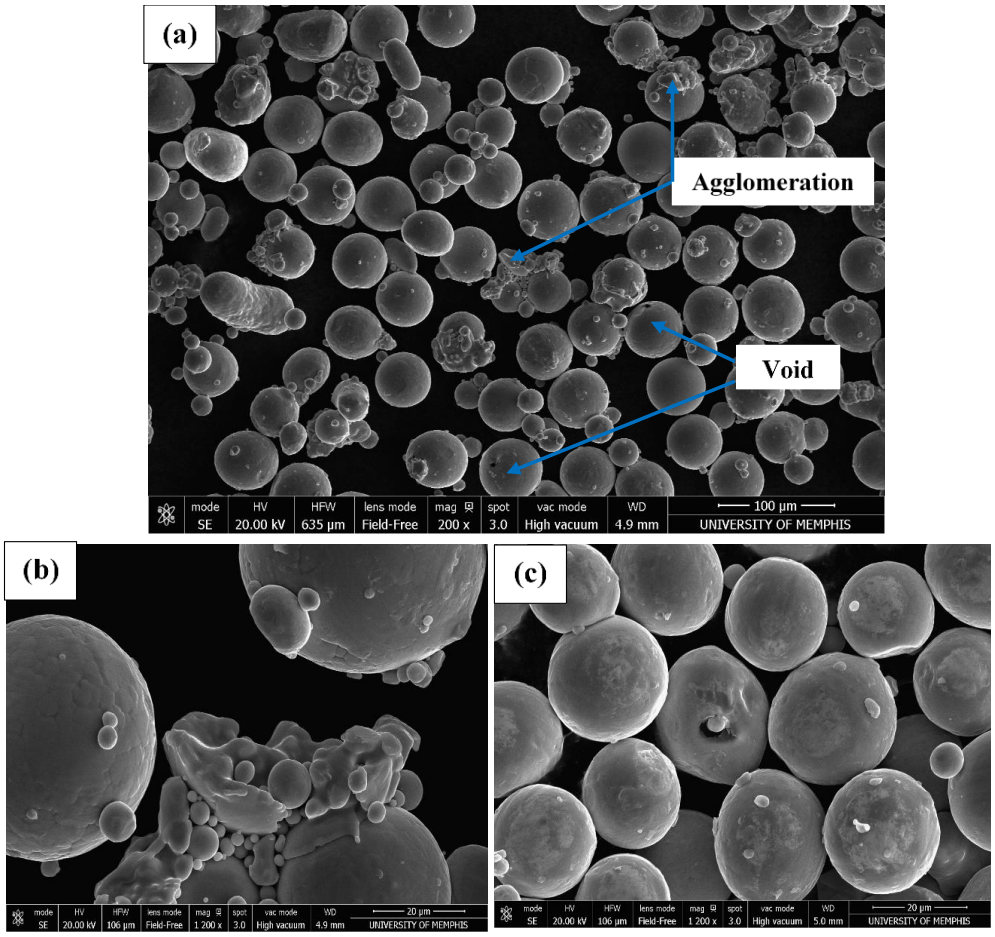

Figure 29. SEM images of the used Ti-6Al-4V powders: (a) Surface morphology, (b) Example of powder agglomeration due to prior DMLS process, and (c) Example of voids in powders.

Figure 30 illustrates the nominal geometry of the samples and two examples of the fabricated samples using the DMLS process. The samples are rectangular cub with 60° overhanging that allows studying the effect of process parameters on the roughness of upskin and downskin surfaces in addition to the top surface of the samples. Overall, the following seven roughness parameters, i.e. three surface roughness and four line roughness parameters, are measured: top, upskin, and downskin surface roughness parameters, and upskin/downskin horizontal/vertical line roughness parameters.

Horizontal lines are perpendicular to the build direction (z) and vertical lines are oriented in the z-direction. These roughness parameters were measured using a Keyence model VHX-6000 digital microscope according to the ASME B46.1.

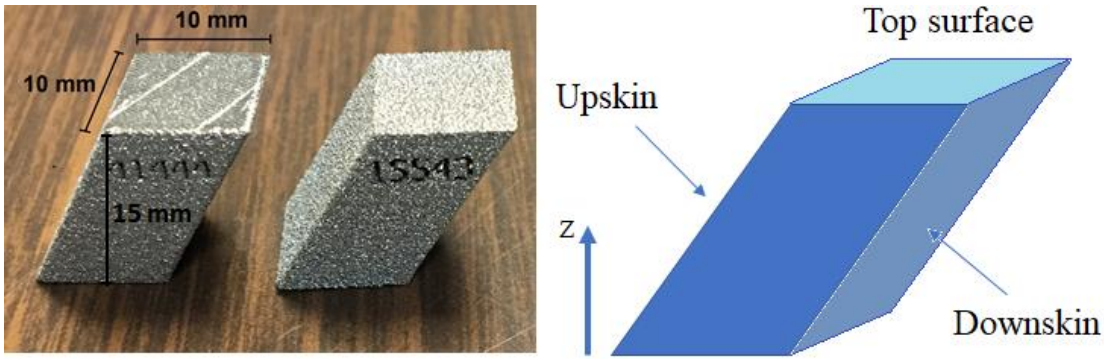

Figure 30. Illustration of the geometry and surfaces of the samples used in this study (left) and two examples of manufactured samples using various DMLS parameters.

For microhardness testing, the samples were mounted in Phenolic powder using a Leco PR-32 automatic pneumatic mounting press and polished using a Struers Rotoforce-4 polishing setup in three levels. For plane grinding, a diamond abrasive plate with a size of 220 μm was used with water as coolant until grinding almost half a width of the samples (to reach a cross-section surface at their center). For fine grinding, a 9 μm diamond abrasive plate was employed with DiaPro Allergorag with a size of 9 μm as a suspension for 7 minutes. For the polishing step, an abrasive plate of colloidal silica suspension in size of 0.04 μm was used, and OP-S* (90% OP-S, 10% H_2O_2) was employed as a lubricant for this step. A Shimadzu HMV-G Microhardness Tester with Vickers indentor was utilized for microhardness testing. The tests were conducted on a rectangular pattern, having 15 points on each sample for indentation. The average value of these 15 indentations on each sample is used as the value representing the microhardness of the samples.

A Mettler Toledo analytical weight balance model ME104E mounted with an Archimedes density kit model ME-DNY-4 was used for the relative density measurements of the samples according to the ASTM B311−17. All the samples were placed in the boiling water for one hour followed by a two-hour soak in water at room temperature before the density measurements.

5.3 Design of Experiments (DoE) for DMLS Process Parameters

5.3.1 Taguchi Method

The first step in DoE methodologies is to determine the parameters and their levels to be tested. The process parameters and corresponding levels considered for this research are shown in Table 15. The limits of the parameters are chosen based on the manufacturability of parts using various combinations of the parameters. Criteria to evaluate the part manufacturability is the absorbed energy density by the material during the DMLS process that can be estimated qualitatively by $E = P / (v.h.t)$ [51]. Too high and too low energy densities result in failure in the manufacturing of the samples [52]. The experimental design calculations and analysis of the Taguchi and response surface methods are done by using Minitab 18.1 software developed by Minitab, LLC.

Table 15. DMLS processing parameters and their levels used in this study

Process parameter	Symbol	Level 0	Level 1	Level 2	Level 3	Level 4
Laser power (W)	A	170	210	250	290	330
Scan speed (mm/s)	B	900	1050	1200	1350	1500
Hatch spacing (µm)	C	100	120	140	160	180
Layer thickness (µm)	D	20	30	40	50	60
Stripe width (mm)	E	3	4	5	6	7

To obtain the parameter combinations for the experiments of the Taguchi method, orthogonal arrays are used from any available Taguchi reference manual. For five factors, which have five levels each, the L_{25} Taguchi orthogonal arrays are used in this study and listed in Table 23 in the appendix. The next step is to calculate the Signal-to-Noise ratio (S/N). In every design, more signal and less noise is desired (regardless of the property), so the best design will have the highest S/N ratio. The S/N ratio η is defined as:

$$\eta = -10 \times log_{10}(MSD) \tag{5.1}$$

where *MSD* is the mean square deviation for output characteristics and it is formulated according to whether the objective is to minimize, maximize, or reduce the variation around the target value. The corresponding *MSD* formulae are:

$$MSD = \frac{1}{n}\sum_{i=1}^{n} y_i^2 \text{ for smaller-the-better,} \tag{5.2}$$

$$MSD = \frac{1}{n}\sum_{i=1}^{n} \frac{1}{y_i^2} \text{ for bigger-the-better, and} \tag{5.3}$$

$$MSD = \frac{1}{n}\sum_{i=1}^{n} \left(y_i - m\right)^2 \text{ for nominal-the-better} \tag{5.4}$$

where y_i is the ith observed response value, n is the number of test results, and m is the target value of the response.

5.3.2 Response Surface Method (RSM)

A fractional factorial design is employed in this study to design the process parameters combinations for RSM. In general, in an experiment with k factors, each of which has l levels, an l^{k-p} design is a fractional factorial design in l^{k-p} runs. In this study, for five factors in five levels, a 5^{5-3} design is chosen that requires 5^2 or 25 runs, which is only 1/125th of the full factorial design observations (5^5 runs). To generate 25 runs for a

5^{5-3} design, the 25 combinations of a 5^2 full factorial design are placed in the first two columns of the table. The cells of the three remaining columns are generated using the cells in the first two columns according to the following equations [53].

$$x_3 = x_1 + x_2,\ x_4 = x_1 + 2x_2,\ x_5 = x_1 + 3x_2 \text{ (mod 5)} \tag{5.5}$$

where x_i is the ith column of the table. Mod 5 refers to the modulus 5 calculus, which is employed in the construction of five-level designs (In modulus 5 calculus, any multiple of 5 equals zero.). The fractional factorial design combinations of the factor levels for the number of experiments are shown in Table 24 in the appendix.

The objective of RSM is to formulate the response as a function of contributing factors and to find the best set of factor levels, which provides the optimum response value based on the research goals. Quadratic relationships are of more interest to researchers since linear models are not capable of capturing any two-parameter influence on the response and cubic and higher degree interactions add to the cost of experiments and complexity in determining the RSM functions. In the present study, the results obtained by the Taguchi method show that the stripe width has a negligible effect on the measured responses, therefore, this factor is excluded from the rest of the study, i.e. RSM and ANN. A quadratic behavior of the response of a system of four factors can be modeled as:

$$\begin{aligned} y = {} & \beta_0 + \beta_1 x_1 + \beta_2 x_2 + \beta_3 x_3 + \beta_4 x_4 + \beta_{12} x_1 x_2 + \beta_{13} x_1 x_3 + \beta_{14} x_1 x_4 + \beta_{23} x_2 x_3 + \beta_{24} x_2 x_4 \\ & + \beta_{34} x_3 x_4 + \beta_{11} x_1^2 + \beta_{22} x_2^2 + \beta_{33} x_3^2 + \beta_{44} x_4^2 \end{aligned} \tag{5.6}$$

where x_1 to x_4 are the factors and β_i s are coefficients to be found using the experimental observations. The response y can be either of output parameters (e.g., surface roughness, microhardness, etc.) that need to be optimized based on the input processing parameters.

5.3.3 Artificial Neural Network

Using a trained ANN, all the sample properties can be predicted simultaneously based on the input process parameters. Here, the input layer is designed with four neurons corresponding to the four DMLS process parameters *P*, *v*, *t*, and *h*. To reduce the complexity of ANN, we only consider one of the surface roughness parameters as network response; i.e. top surface roughness. Therefore, the output layer was designed with three neurons to predict microhardness, relative density, and top surface roughness.

The network was trained and tested using raw, unnormalized measures of input process parameters and output sample properties. A total of 45 samples were used for training and testing the performance of the neural network. The network was trained using the Bayesian regularization method [54], which, after testing several algorithms, turned out to be the most accurate method for the data used in this study. The Bayesian regularization method does not require a separate group of validation data. Therefore, all available data were divided into a training group and a testing group. To be consistent with the Taguchi and the RSM methods, and to conduct a fair comparison among them, 25 data samples (55% of all data) were used for training and building the ANN. Therefore, the remaining 20 data samples (45% of all data) independent of the training data samples were used for testing the performance of the model.

Figure 31 illustrates the architecture of the feed-forward neural network with two hidden layers implemented in Matlab R2019b software, which is developed by Mathworks, and used in this study. The recommended range for the number of hidden neurons as the starting point for determining the optimal parameters for AM applications is 5–10 [31]. As the number of hidden neurons increases, the training data prediction

error decreases, and the network complexity as well as its capability for capturing more details of data behavior increases. With limited data of this study, however, increasing the number of hidden neurons makes the network biased to the training data and not capable of predicting new unseen data. After testing several networks with different numbers of hidden layers as well as different numbers of nodes in each hidden layer, we determined the best performance for the model with two hidden layers having six and five neurons for the first and second hidden layers, respectively. Fractional prediction error, which is defined as the mean absolute difference between the network predicted output and the true output divided by the true output for each new process parameter combination, was used to assess the prediction accuracy and performance of the Taguchi method, RSM, and the ANN. For all the three methods, 20 new (unseen) data sets are used for testing the model.

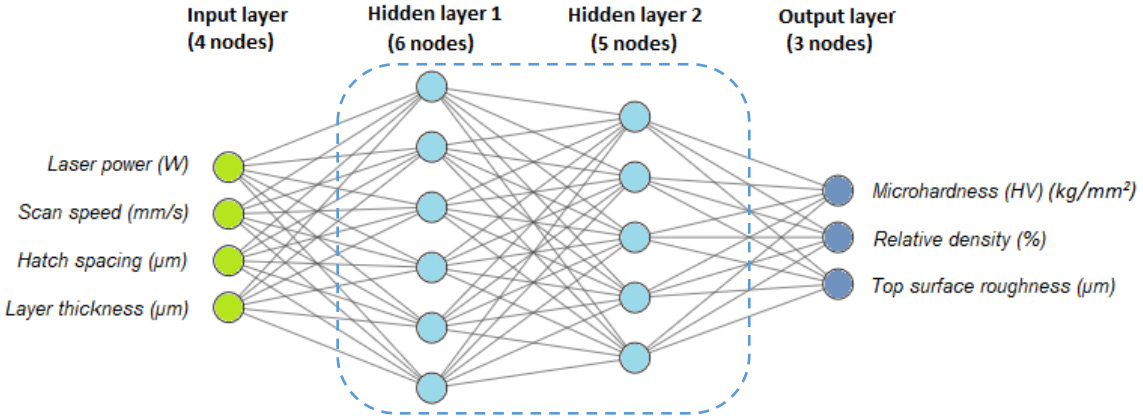

Figure 31. The neural network architecture with six and five nodes in two hidden layers

5.4 Results and Discussions

All the raw measurements for all the DMLS process parameters listed in Table 23 and Table 24 are presented in Table 25 in the appendix. In the next sub-sections, the Taguchi, RSM, and ANN calculations and discussions are presented.

5.4.1 Taguchi Method

MSD values are calculated using Equations 5.2 and 5.3, depending on the measured property, i.e., smaller-the-better (Eq. 5.2) for roughness values and bigger-the-better (Eq. 5.3) for density and microhardness values. Hereafter, we refer to these desired values (higher or lower depending on the property) as the optimum values for simplicity. Having the *MSD* values, S/N ratios are calculated using Eq. 5.1. Figure 32(a-i) shows S/N plots of different factors (A to E) and for different properties (e.g., microhardness, relative density, etc.). Each single point on the S/N graphs for each factor at each level is the average of S/N ratios of all the samples, which are manufactured using that factor at that level. For instance, the value of the first point from left on the graph shown in Figure 32a is the mean S/N value of microhardness of all the samples, which are manufactured using the laser power of 170 W.

As it was mentioned before, a high S/N ratio is always desired. So, the combination of the factors that leads to the optimum response is obtained by collecting the level of each factor that results in the highest S/N values for that response. For instance, Figure 32(a) shows that using the A4-B1-C1-D2-E2 combination of the factors results in the highest microhardness value in the given range of the process parameters. This is corresponding to DMLS process parameters of P=290 W, v=1200 mm/s, h=100 µm, t=30 µm, and d=4 mm.

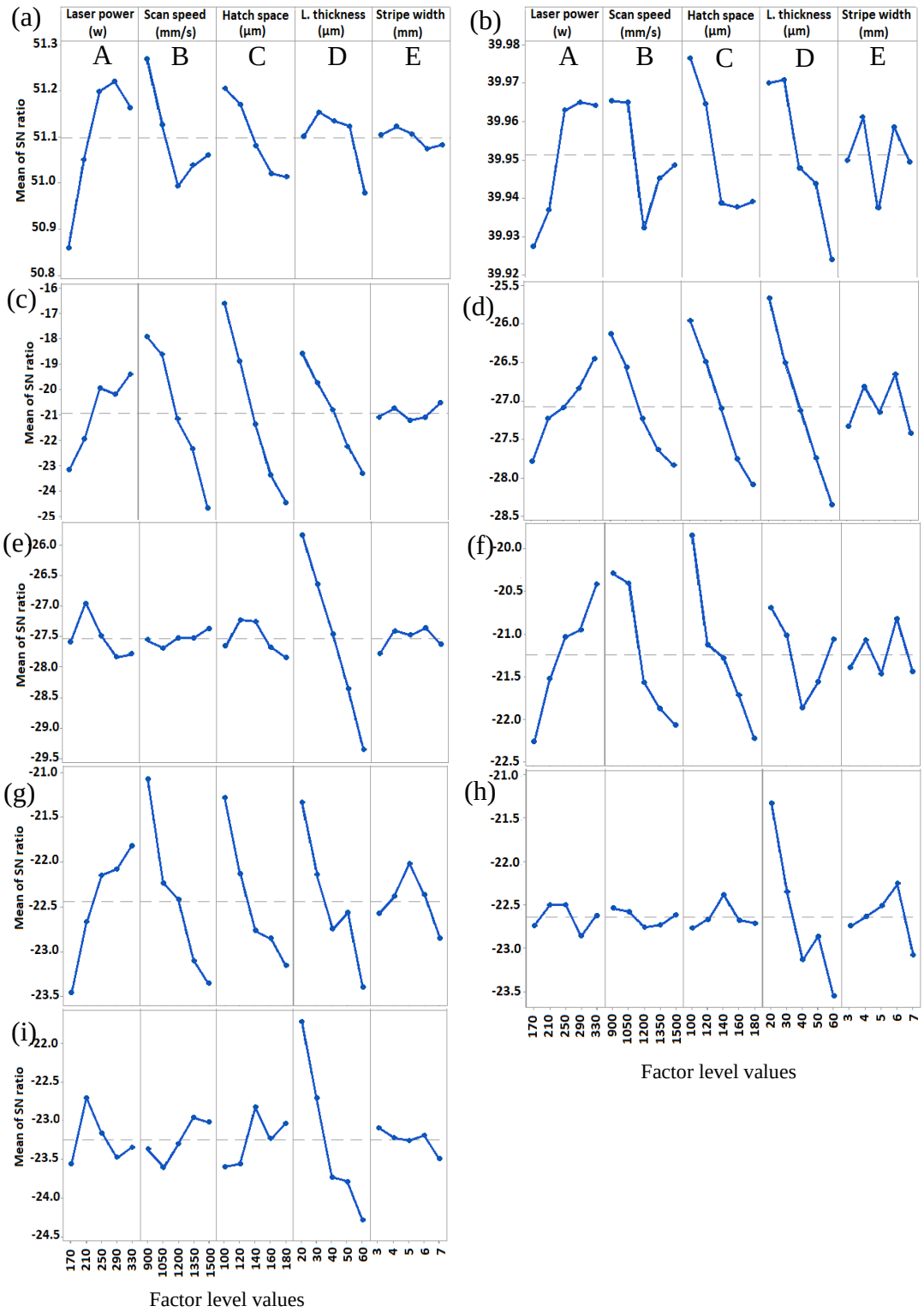

Figure 32. Main effects plot for S/N ratios of (a) microhardness, (b) relative density, (c) top surface roughness, (d) upskin surface roughness, (e) downskin surface roughness, (f) upskin horizontal line roughness, (g) upskin vertical line roughness, (h) downskin horizontal line

Table 16 lists the combinations of the DMLS processing parameters that resulted in the optimum values for all the considered properties based on the S/N plots shown in Figure 32. Analysis of variances (ANOVA) quantifies the contribution of each factor to the total variation of the response. P-values and contributions of the factors on different responses based on ANOVA linear regression results are presented in Table 17.

Table 16. Rankings and best combinations of the factors based on the Taguchi analysis.

Response	Best combination of DMLS parameters					Optimized Response	Energy density (J/mm^3)	Significance Ranking
Microhardness	A4 290	B1 900	C1 100	D2 30	E2 4	378.48	107.4	A>B>C >D>E
Relative density	A4 290	B1 900	C1 100	D2 30	E2 4	100.00	107.4	D>C>A>B>E
Top surface roughness	A5 330	B1 900	C1 100	D1 20	E5 7	0.01	183.3	C>B>D>A>E
Upskin surface roughness	A5 330	B1 900	C1 100	D1 20	E4 6	10.88	183.3	D>C>B>A>E
Downskin surface roughness	A2 210	B5 1500	C2 120	D1 20	E4 6	16.54	58.3	D>A>C>E>B
Upskin H. line roughness	A5 330	B1 900	C1 100	D1 20	E4 6	6.56	183.3	C>A>B>D>E
Upskin V. line roughness	A5 330	B1 900	C1 100	D1 20	E3 5	6.16	183.3	B>D>C>A>E
Downskin H. line roughness	A2 210	B1 900	C3 140	D1 20	E4 6	10.20	83.3	D>E>A>C>B
Downskin V. line roughness	A2 210	B4 1350	C3 140	D1 20	E1 3	9.92	55.6	D>A>C>B>E

*A: laser power (W), B:scan speed (mm/s), C: hatch spacing (µm), D: layer thickness (µm), E: stripe width (mm)

In statistical hypothesis testing, a p-value or probability value is the probability under a specified model that a statistical measurement of the data would be equal to or more than its observed value. In other words, P-value is the probability of obtaining test

results at least as extreme as the results observed during the actual test, assuming that the so-called “null hypothesis” is correct [55]. The null hypothesis often postulates the absence of an effect, such as a relationship between a factor and an outcome. Therefore, a p-value gives the ability to evaluate the incompatibility between a factor and a proposed model for the data. Smaller p-values show the greater statistical incompatibility of the data with the null hypothesis, meaning more significance of the factor for the model. The percent contribution for any parameter is calculated by dividing the sum of squares for that factor by the total sum of squares of all factors and multiplying the result by 100 [56]. The last column of Table 16 summarizes the ANOVA results by ranking the contributions of the factors on the response from the highest to the lowest. The significance in the contribution of each factor to the response can be also inferred from S/N plots. The factors with higher variations on S/N values have a higher influence on the related response. This is proportional to the contributions of the factors, which are inversely proportional to their p-value, presented in Table 17. For instance, factor A (laser power) is the most significant factor with 45.3 % contribution in predicting the microhardness. The next factors, in the order of significance, are B (23 %), C (13.9 %), D (7.9 %), and E (0.7 %).

Table 17. P-values and contribution percent of the process parameters in different responses based on ANOVA linear regression results.

Parameter	Microhardness		Relative density		Top surface roughness	
	P-Value	Contribution (%)	P-Value	Contribution (%)	P-Value	Contribution (%)
laser power	0.071	45.3	0.103	22.6	0.004	19.0
scan speed	0.185	23.3	0.197	14.1	0.002	27.7
hatch spacing	0.334	13.9	0.098	23.5	0.001	33.6
layer thickness	0.542	7.9	0.075	28.0	0.004	17.6
stripe width	0.984	0.7	0.464	6.2	0.282	1.3
Error	-	8.8	-	5.6	-	0.7
Parameter	Upskin surface		Upskin hor. line		Upskin ver. line	
	P-Value	Contribution (%)	P-Value	Contribution (%)	P-Value	Contribution (%)
laser power	0.304	11.4	0.192	22.6	0.035	20.4
scan speed	0.196	16.6	0.15	27.3	0.02	28.2
hatch spacing	0.114	24.8	0.131	30.0	0.034	20.8
layer thickness	0.065	35.9	0.5	8.8	0.029	22.8
stripe width	0.624	4.7	0.878	2.5	0.258	5.2
Error	-	6.6	-	8.8	-	2.6
Parameter	Downskin surface		Downskin hor. line		Downskin ver. line	
	P-Value	Contribution (%)	P-Value	Contribution (%)	P-Value	Contribution (%)
laser power	0.646	5.6	0.956	2.9	0.694	7.6
scan speed	0.996	0.3	0.99	1.2	0.879	3.6
hatch spacing	0.772	3.7	0.972	2.2	0.705	7.3
layer thickness	0.024	81.2	0.141	64.7	0.071	66.9
stripe width	0.974	0.9	0.769	9.0	0.966	1.6
Error	-	8.3	-	20.0	-	13.0

The presented results in Figure 32 and the last column of Table 16 and Table 17 suggest that the influence of factor D (layer thickness) on all three downskin roughness responses dominates the influence of all the other four considered factors; i.e. the contribution of all the other factors on the three downskin roughness responses are less than 10%. In all the three cases the optimum layer thickness is the smallest considered layer thickness, which is 20 µm. This observation shows that layer thickness-related

mechanisms such as stair-stepping are the dominant factor influencing the downskin roughness in the DMLS process in agreement with previous observations in the literature [57]. Thus, the smallest possible layer thickness is desired in the DMLS process based on Taguchi analysis to minimize the downskin surface roughness. However, there are other considerations for the DMLS process to set the lower limit of the layer thickness such as manufacturing time, the upper limit of the powder size distributions, and powder bed distortion due to the inert gas flow. To optimize the other four factors to achieve optimum downskin roughness, a reasonably small layer thickness must be chosen based on the considerations mentioned above as well as the tolerable downskin roughness. Then, another DoE such as Taguchi with the remaining four factors must be performed to determine the optimum DMLS processing parameters. Generally, it is expected to have lower energy densities to improve downskin roughness response compared to the energy density corresponding to the optimum bulk properties such as relative density or microhardness [58,59]. The slower cooling mechanism for downskin compared to the bulk of the part confirms this expectation; i.e. the cooling mechanism changes from the faster full conduction through the build plate to the half-conduction through the build plate and convection for downskin [60]. On the other hand, at each layer, the laser beam penetrates to some lower layers, and in down-facing surfaces, a beam with very high energy densities absorbs and partially melts surrounding powder particles that results in attaching them into the surface and increasing the roughness [61–63]. Therefore, the levels of the factors need to be adjusted to result in lower energy densities for the new DoE.

Similar analogy and conclusions apply to the upskin roughness values regarding the role of the layer thickness. However, the layer thickness is not the only factor influencing the upskin roughness values. Hatch spacing, scanning speed, and laser power are the three other factors significantly contributing to the upskin roughness values; this fact also applies to top surface roughness values. This three-factor combination effect suggests the chosen ranges of the levels are sufficient to optimize the upskin and top surface roughness given a fixed layer thickness chosen based on the tolerable downskin roughness responses. Interestingly, the optimum factors for all the three considered upskin roughness parameters and the top surface roughness are identical, P=330 W, v=900 mm/s, h=100 µm. These optimum parameter levels correspond to the limits of the levels that result in the highest energy density (183.3 J/mm^3) considering all the combinations of the used levels; i.e. the highest considered laser power and the lowest scanning speed and hatch spacing. Consequently, it can be concluded the Taguchi method recommends the highest energy density level to obtain the smallest roughness values for upskin and top surfaces roughness of DMLS-fabricated parts. This is in contrast with the finding related to the optimum downskin roughness values where lower values of energy density (~55 J/mm^3) correspond to the optimum downskin roughness values. A possible explanation for this observation may be offered by considering the gravity force that smoothens the melt lines on the top and upskin surfaces while it coarsens the melt lines that are unsupported for downskin surfaces [64,65].

The DMLS process parameters corresponding to optimum microhardness and relative density responses turn out to be identical, which are P=290 W, v=900 mm/s, h=100 µm, t=30 µm, and s=4 mm. However, the significance of factors and their

contributions are different for these responses suggesting they are influenced by different mechanisms. The significant factors influencing relative density are laser power (22.6% contribution), scan speed (14.1% contribution), hatch spacing (23.5% contribution), and layer thickness (28.0% contribution) while there is a slight contribution from stripe width (6.2% contribution). This conclusion from ANOVA agrees well with several past observations that suggest relative density qualitatively correlates with energy density with collective contributions from *P, v, h,* and *t* [26,50]. The reported trend in literature is valid here too, which is the relative density increases drastically by increasing the energy density due to the removal of the lack of fusion defects to a maximum value followed by a slight decrement due to the creation of entrapped gas porosities at higher energy densities [6,66–68]. This matter is evident by considering the S/N ratios behavior for relative density response in Figure 32(b) wherein there is a sharp increase of S/N ratios by increasing laser power and decreasing layer thickness and scan speed followed by slight decrement. The S/N ratio for *h* factor is an exception that increases monotonically by decreasing its levels. Finally, the stripe width has a small contribution to the relative density. It appears the contribution of stripe width in the total defects in part is more near the outer boundary of parts where the complete stripe width is not observed. For these incomplete stripe width scans, the cooling time before the adjacent line's scanning is shorter that may result in higher energy density and entrapped gas porosities.

Regarding the microhardness response, the correlation explained for energy density and relative density is roughly valid. However, only three factors have a meaningful contribution to the microhardness response. Laser power is the dominant factor (45.3% contribution) influencing the microhardness response followed by scan speed (23.3%

contribution) and hatch spacing (13.9% contribution) while the contributions of layer thickness and stripe width are less than the error in ANOVA analysis (8.8%) for this response and considered insignificant. The dominance of laser power on microhardness response is an interesting observation that is not justified regarding the energy density factor. A possible explanation can be offered by considering the significant influence of laser power on the fluid flow and recoiling pressure inside the melt-pool [20]. As laser power increases, the fluid flow inside the melt-pool becomes stronger resulting in more homogenous solid solution after solidification that in turn increases the microhardness. As the laser power increases further, the recoiling pressure increases, resulting in the collapse of the melt-pool and creating defects that in turn decrease the microhardness. Furthermore, microhardness is determined by Vickers indentations on cross-sections of parts in the XY direction, having the indentation diagonals around ~70 µm, which is larger than the thickness of the thickest layer. So, a single indentation, regardless of the layer thickness, always include more than one layer, thus is always affected by the part interlayer bondings and that explains the negligible influence of the layer thickness on the microhardness response. Finally, the microhardness indentations were performed away from the boundaries where the contribution of the stripe width on densification is significant; this fact justifies the observed insignificant influence of stripe width on microhardness response.

5.4.2 RSM

Quadratic models are fitted to Eq. (5.9) to calculate the coefficients (β_i) for each property. Parameter values were normalized before being used for regression. Table 18 presents the coefficients of the response surface equation of each property (e.g.,

microhardness, relative density, etc.) as functions of linear, two-way interaction, and quadratic terms of process parameters. To evaluate the significance of each coefficient P-values obtained from ANOVA of quadratic response surface regression for different responses are listed in Table 19. Response surface plots are very useful to evaluate the interaction effects between two parameters in a DoE study. Figure 33 illustrates the surface plots of each two-parameter combination when the other two parameters are kept constant at their default values, which are presented in the lower right section.

Table 18. Coefficients of the response equations.

Parm.	Micro-hardness	Rel. density	Top surface	Upskin surface	Up hor. line	Up ver. line	Down surface	Down hor. line	Down ver. line
Cons.	364.05	100.31	4.72	16.44	8.57	10.55	19.32	11.66	12.15
A	16.1	1.45	-15.78	-1.25	-3.16	-1.74	3.59	3.89	-2.13
B	7.1	-0.23	-9.3	6.98	5.91	0.43	-5.4	0.31	5.82
C	-35.3	-2.13	0.35	0.07	-1.06	3.87	5.73	2.83	2.20
D	7.2	-0.26	13.31	6.11	2.78	1.67	2.55	2.80	4.88
A^2	-26.74	-2.007	14.67	2.61	2.70	2.31	7.44	1.79	3.97
B^2	-6.7	-0.77	11.42	1.21	-0.74	5.15	2.12	0.72	-5.43
C^2	12.3	0.50	20.1	2.43	1.94	-0.29	-1.75	3.77	-3.43
D^2	-2.65	0.417	7.31	2.62	0.31	3.58	-0.49	-3.19	-3.97
AB	5.4	1.21	18.8	-3.27	-1.60	-0.49	-3.85	-7.38	-2.49
AC	34.3	1.89	-21.6	1.03	1.48	-3.03	-8.07	1.02	1.35
AD	3.79	-0.277	-10.62	-3.90	-2.22	-3.28	4.07	1.45	1.48
BD	-11.2	-0.50	-11.94	-2.95	-0.89	-3.85	6.71	4.74	2.90

Since normalized parameters are used to form the response equations, the magnitude of their coefficients (Table 18) is an indication of their significance in predicting the response. The response equation obtained for each property can be used to visualize the variations of that response versus the variations of two predictors at a time. Therefore, the rest of the factors should be kept constant while the variation of two of them is plotting the response surface. Any convolution on the surface plot indicates the variation of one factor alters the behavior of the other factor. For instance, in Figure 33(a), in the interaction between laser power and hatch spacing, i.e., the AC plot, it can be seen that when laser power (A) is at its highest level, with increasing hatch spacing (C), microhardness value increases, however, when laser power (A) is at its lowest level, microhardness decreases with increasing the hatch spacing (C). Therefore, it can be said that the effect of laser power on microhardness depends on the hatch spacing level. This surface is the most convoluted surface among the microhardness response surfaces (Figure 33a), indicating that these two parameters, i.e., laser power and hatch spacing, are the most correlated factors in predicting microhardness of the fabricated parts. This conclusion can be supported by comparing the coefficient (2nd column of Table 18) and contribution percentage (3rd column of Table 19) of AC with the other interactions, i.e., AB, AD, and BD. The contribution percentage of AC interaction in predicting microhardness is 13.9%, which is higher than 0.3%, 0.4%, and 2.2% for AB, AD, and BD, respectively. A similar significance of AC with respect to the other parameter interactions can be seen in predicting the relative density and top surface roughness (Figure 33(b, c), Table 18, and Table 19). Figure 33 (b) illustrates that the effects of laser scan speed on relative density at high levels of laser power are negligible, however, when

the laser power is low, the response decreases sharply with increasing the scanning speed. The interaction of scanning speed and layer thickness in predicting microhardness and relative density (BD interaction) in Figure 33 (a, b) shows that at a low layer thickness, e.g., 20 µm, with increasing the laser scan speed microhardness increases and relative density decreases. However, when the layer thickness is high, increasing the scan speed has the opposite effect of decreasing microhardness and increasing relative density. These behaviors can be justified considering the optimum values of these properties versus energy density [69]. For instance, take microhardness behavior with respect to energy density as an example. A low layer thickness, generally, results in a high energy density (higher than the optimum value, which gives the maximum microhardness value) so, increasing scan speed moves the microhardness towards the maximum value (increasing). However, high layer thickness values lead to energy densities lower than the optimum value, therefore, increasing scan speed, i.e., decreasing the energy density, moves it away from the peak and decreases the microhardness.

Table 19 shows that as oppose to microhardness and relative density, in upskin roughness properties, the interaction between laser power and layer thickness (AD interaction) is the most significant one among the other interactions. Figure 33 (d-f) illustrates this by showing changes in the effect of one parameter on the response when the other parameter is varied. In these cases, it can be seen that when laser power is low, the roughness value increases drastically with increasing the layer thickness, but it does not change with increasing the layer thickness at high levels of laser power. This may be attributed to the fact that high laser powers form deeper melt-pools [4], which penetrate deeper and melt the previously deposited layers regardless of their thickness and conceal

the effects of layer thickness on roughness values. However, this is not the case for down-facing surfaces. Increasing the layer thickness increases the roughness, regardless of the other parameters. This can be verified by the interaction of layer thickness with other parameters (AD, BD, and CD interactions in Figure 33 (g-i)). This behavior can be due to the stair-stepping effect as it was discussed earlier, and it is confirmed by being less observable in downskin horizontal line roughness, rather than downskin surface roughness and downskin vertical line roughness responses.

By comparing the p-values and contribution percentages of quadratic terms with the linear ones in the responses, the behavior type of each response can be realized. For instance, in the proposed model for upskin surfaces, the contribution percentages of quadratic terms are negligible compared to the linear ones. Also, the related response surface presented in Figure 33 (d-f) shows smaller curvature compared to the other response behaviors. Therefore, and since the R^2 values of these response equations are relatively high (Table 19), it can be concluded that modeling upskin roughness parameters using a linear model can be less expensive while it does not miss any significant quadratic effect of main factors and their interactions.

Table 19. P-values and contribution % associated with different coefficients obtained from ANOVA of response surface regression for different responses

Source	Micro-hardness		Relative density		Top surface		Upskin surface		Upskin hor. line		Upskin ver. line		Downskin surface		Downskin hor. line		Downskin ver. line	
	P-value	Cont. %	P-value	Cont. %	P-value	Cont. %	P-value	Cont. %	P-value	Cont. %	P-value	Cont. %	P-value	Cont. %	P-value	Cont. %	P-value	Cont. %
Model	0.001	-	0.123	-	0.001	-	0.002	-	0.001	-	0.008	-	0.020	-	0.024	-	0.070	-
A	0.001	30.6	0.029	19.9	0.004	14.5	0.192	3.7	0.025	10.1	0.012	19.5	0.003	31.2	0.004	32.1	0.052	13.5
B	0.405	1.3	0.051	15.1	0.045	6.0	0.003	26.5	0.000	47.6	0.008	23.0	0.417	1.6	0.776	0.2	0.578	0.9
C	0.059	7.7	0.127	8.5	0.002	19.9	0.039	10.4	0.032	9.0	0.065	9.4	0.980	0.0	0.650	0.5	0.584	0.9
D	0.781	0.1	0.501	1.5	0.002	17.9	0.002	30.5	0.045	7.7	0.131	5.9	0.004	29.6	0.016	19.4	0.009	27.7
A^2	0.006	19.8	0.044	16.3	0.049	5.7	0.494	1.0	0.180	3.1	0.440	1.4	0.223	3.8	0.517	1.1	0.180	5.9
B^2	0.521	0.8	0.615	0.8	0.206	2.1	0.801	0.1	0.765	0.1	0.186	4.5	0.778	0.2	0.836	0.1	0.152	6.8
C^2	0.366	1.6	0.772	0.3	0.092	4.0	0.695	0.3	0.544	0.6	0.952	0.0	0.857	0.1	0.406	1.8	0.466	1.6
D^2	0.794	0.1	0.685	0.5	0.398	0.9	0.579	0.6	0.899	0.0	0.337	2.3	0.946	0.0	0.358	2.3	0.274	3.8
AB	0.692	0.3	0.426	2.1	0.116	3.4	0.603	0.5	0.619	0.4	0.919	0.0	0.695	0.4	0.122	6.9	0.599	0.8
AC	0.016	13.9	0.329	3.2	0.057	5.3	0.859	0.1	0.620	0.4	0.506	1.1	0.381	1.9	0.808	0.2	0.758	0.3
AD	0.626	0.4	0.726	0.4	0.120	3.3	0.287	2.4	0.241	2.3	0.253	3.3	0.472	1.3	0.578	0.8	0.586	0.9
BD	0.290	2.2	0.630	0.8	0.186	2.4	0.541	0.8	0.719	0.2	0.314	2.5	0.379	1.9	0.189	4.8	0.428	1.9
Fitting coefficients																		
R^2 (%)	87.0		71.7		86.7		85.4		87.8		81.5		77.8		76.9		70.7	
R^2_{adj} (%)	73.9		37.7		73.4		70.8		75.5		63.0		55.6		53.8		41.4	

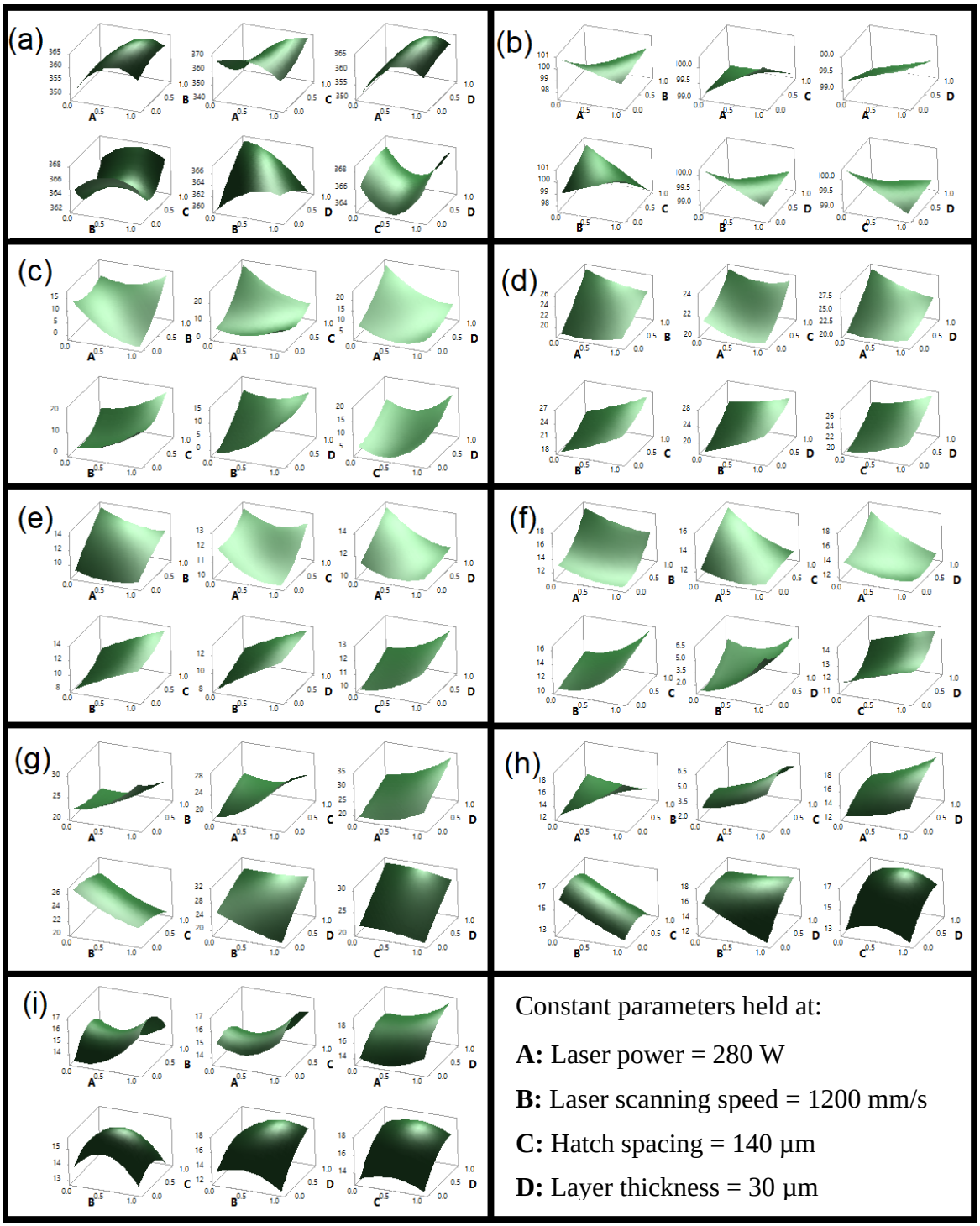

Figure 33. Response surface plots of each two-parameter combination for (a) microhardness, (b) relative density, (c) top surface roughness, (d) upskin surface roughness, (e) upskin horizontal line roughness, (f) upskin vertical line roughness, (g)

downskin surface roughness, (h) downskin horizontal line roughness, and (i) downskin vertical line roughness.

Response optimization helps to identify the variable settings that optimize a single response. Table 20 presents the parameter settings that minimize/maximize each of the response equations (Table 18) along with the optimized responses, which can be obtained using those parameter combinations. The standard error of the fit (SE fit) estimates the variation in the estimated mean response for the specified variable settings and it is used for the calculation of the confidence interval (CI) for the mean response. The 90% confidence intervals are ranges of values that are 90% probable to contain the mean response for the population that has the observed values of the factors in the model. Table 20 shows that the smallest layer thickness is recommended to achieve superior roughness parameters on all the surfaces investigated in this research. This is consistent with the Taguchi recommendation (Table 16). Similar to the Taguchi optimization, larger values of energy density is recommended for up-facing, i.e., top and upskin, surfaces rather than for downskin roughness parameters. According to the information presented for the roughness values in Table 20 columns A and B, the factors can be categorized into two groups: 1) downskin surface and vertical line roughness and 2) other surface properties. The recommended scanning speed values for the former is higher than the ones for the latter. This is consistent with the Taguchi results, as well.

Table 20. Optimization results of the RSM for different output properties

	Parameters combination				Optimized response	Energy density	SE fit	90% CI
	A	B	C	D				
Microhardness	330	1024	180	54	372.5	33.2	3.72	(365.9, 379.2)
Relative density	170	900	180	20	99.99	52.5	1.69	(97.1, 103.2)
Top surface roughness	250	900	138	20	0.1	100.6	3.77	(-6.59, 6.83)
Upskin surface roughness	208	900	100	20	16.29	115.6	1.49	(13.65, 18.94)
Upskin horizontal line roughness	262	900	104	20	7.64	140.0	0.893	(6.051, 9.233)
Upskin vertical line roughness	230	900	100	20	10.23	127.8	1.20	(8.08, 12.37)
Downskin surface roughness	173	1500	180	20	16.08	32.0	4.07	(7.71, 24.45)
Downskin horizontal line roughness	170	900	180	20	10.32	52.5	4.38	(2.51, 18.13)
Downskin vertical line roughness	236	1500	180	20	10.64	43.7	1.56	(6.84, 14.43)

A parameter combination that is best for a response does not necessarily optimize the other properties. A multi-response optimization is capable of obtaining a parameter setting that yields to the optimization of all the properties considering their weight. presents the results of the multi-response optimization of all the nine properties (with the same weights) studied in this research. As can be seen, each of the multi-optimized response values is slightly worse than the ones obtained for their individual optimization and this is the compromise for having all of them optimized using a single set of input parameters. It is worth mentioning that this approach can be implemented with different

weights for different responses based on the importance of each response to the specific application of the DMLS component.

Table 21. Multi-parameter multi-response optimization results achieved using the following parameters combination: laser power = 239.5 W, laser scanning speed = 1500 mm/s, hatch spacing = 100 µm, and layer thickness = 20 µm

Micro-hardness (HV, kg/mm^2)	Rel. density (%)	Top surface roughness (µm)	Upskin surface roughness (µm)	Upskin hor. line roughness (µm)	Upskin ver. line roughness (µm)	Down surface roughness (µm)	Down hor. line roughness (µm)	Down ver. line roughness (µm)
362.9	99.89	7.76	18.18	10.44	11.22	17.57	10.95	10.75

5.4.3 Artificial Neural Network

After the ANN is trained, all the data are fed to it and the predictions were compared to the actual values to validate the ANN model. Figure 34 illustrates this comparison for microhardness, relative density, and roughness training and test resulst. Good accuracy and performance of the trained ANN models is observed. A quantitative comparison between the prediction accuracy of the network and the other two employed methods is presented next.

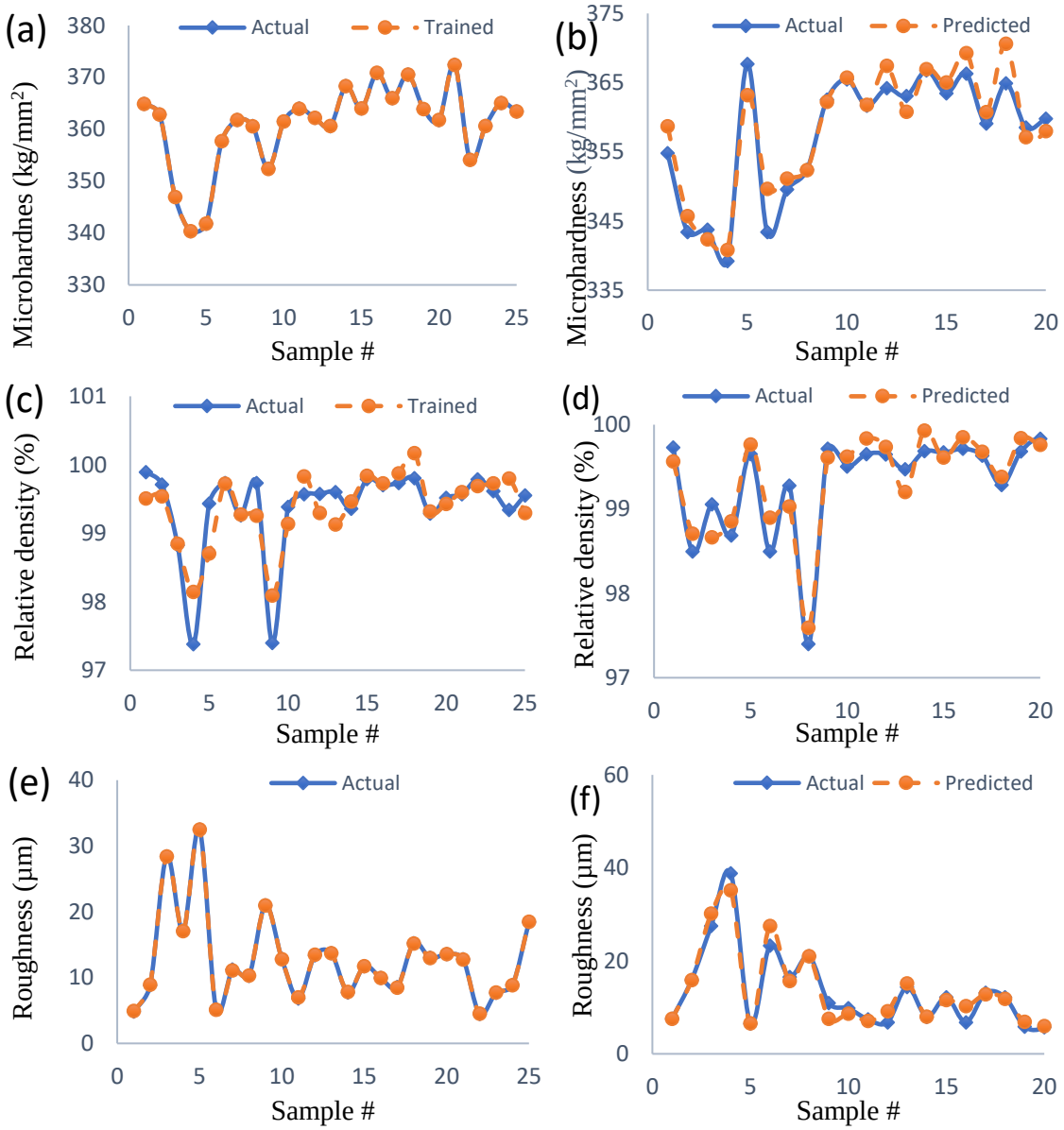

Figure 34. Comparison between the actual and ANN predicted results of training (a, c, e) and test data (b, d, f) for microhardness (a, b), relative density (c, d), and top surface roughness (e, f).

5.4.4 Comparison of Predictions for Taguchi, RSM, and ANN

To compare the performance of the three proposed methods, 20 new parameter combinations (unseen data) are used as input to each model and the output is considered as the predicted response. The difference between the predicted and actual responses is divided by the actual value to obtain the error for each of the 20 unseen data. The mean absolute values of these errors are then calculated for each response property and for all of them and are presented in Table 22. According to the results, the Taguchi method shows the largest mean absolute error values in predicting each and all of the response properties. This verifies that there are non-linear behaviors in responses that the Taguchi method is not able to capture as accurate as of the quadratic models. Considering the microhardness prediction error values, RSM performed slightly better than the ANN, however, the ANN showed much better performance in predicting the other properties of the unseen samples. The error using ANN was about three times larger than when the Taguchi or RSM was used. It can be due to the flexibility of ANN and show how this model can adapt itself based on the type and range of data used for training. ANN also returns a much lower total mean absolute error than the other two methods, which makes it superior in terms of the overall performance.

Table 22. Comparison of fractional error (%) in prediction performance of the Taguchi method, RSM, and the ANN using the testing data presented in this research

Method	Mean fractional error of prediction in percentage (95% CI)			
	Microhardness	Relative density	Top surface roughness	All
Taguchi	1.68 (1.15, 2.21)	0.41 (0.19, 0.62)	32.59 (15.54, 49.65)	11.56 (4.8, 18.32)
RSM	1.06 (0.68, 1.44)	0.30 (0.20, 0.39)	30.16 (16.73, 43.59)	10.51 (4.85, 16.16)
ANN	1.16 (0.78, 1.54)	0.23 (0.13, 0.32)	10.80 (4.80, 16.80)	4.06 (1.75, 6.38)

As the study limitations, we can point out many parameters, investigating the effect of which was not in the scope of this research, yet may influence the ANN results. For instance, the architecture and internal functions used for the ANN were chosen considering the performance of the model based on the experimental data obtained for this research. The size of the training dataset, which was kept constant due to the sake of having a fair comparison between different methods, is another parameter that affects the ANN performance. Therefore, for a different type of dataset with a different size, another ANN may be needed to be developed using a similar approache elaborated in this dissertation. Also, generally, a more promising test of the ANN performance would be to compare the predicted response values to the ones obtained by other researchers/labs using the same sets of process parameters used in this study.

5.5 Implications for Fatigue Performance

It is well known that fatigue is the primary mechanical failure mode of most structural components and that surface roughness significantly affects fatigue performance. However, the layer by layer process partially melted particles attached to the surface, and the stair-stepping effect due to the geometry of the part cause a rough

surface in AM. On the other hand, an important advantage of the AM processes is the ability to manufacture net-shaped components, typically with complex geometries, with no need for further surface treatment. Therefore, an in-depth understanding of the relationship between important AM process parameters and surface roughness discussed in previous sections is essential to the evaluation of the fatigue performance.

The negative effect of surface roughness on fatigue performance of AM metals has been evaluated in many studies, for example in [70]. This effect has been shown to be dominant, even in the presence of relatively large internal defects and various microstructures. Heat treatment processes such as Hot Isostatic Pressing (HIP) do not affect surface roughness. Therefore, only with decreased surface roughness achieved by using optimized build parameters, as discussed in this paper, fatigue performance can be noticeably improved. An example of the correlation between fatigue life and the square root of Ra as a representation of surface roughness is shown in Figure 35 from [71]. As can be seen, the fatigue life at similar stress levels consistently decreases with increasing Ra.

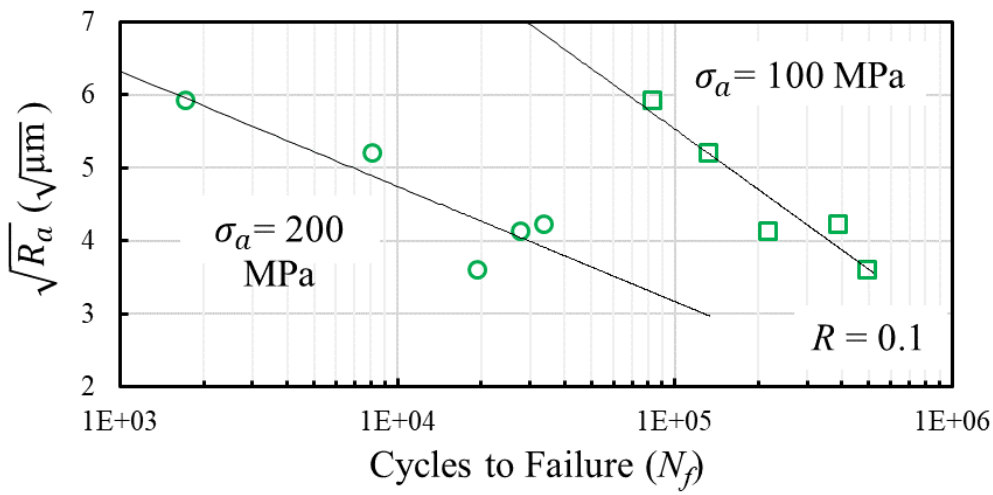

Figure 35. Correlations between fatigue life at two stress amplitudes with square root of Ra for L-PBF Ti-6Al-4V [71].

Different analytical models have been used to incorporate the effect of surface roughness on fatigue performance. In one approach, using the concept of stress concentration factor, surface irregularities can be considered as elliptical surface micro-notches with notch depth related to the maximum surface roughness. In another approach, the concept of fatigue notch factor based on fatigue strength ratio between different surface roughness conditions has been used. However, a more robust approach is based on fracture mechanics. A common example of this approach is Murakami's defect area method based on the effective defect size at fracture origin and the Vickers hardness, HV. In this method, an equivalent defect size for roughness is used, where surface roughness is assumed to be equivalent to periodic notches.

Using the fracture mechanics approach, surface roughness was treated as surface cracks with crack depth as the sum of maximum surface valley and defect induced crack length in [72]. The effect of surface roughness on fatigue behavior of laser-based powder bed fusion additively manufactured Ti-6Al-4V alloy was then experimentally evaluated

under fully reversed axial, torsion, and combined axial-torsion cyclic loading conditions. Experimental fatigue lives were satisfactorily predicted based on this approach, shown in Figure 36 from [72]. Model sensitivity to variations in the maximum valley depth of roughness profile Rv was also evaluated, as can be seen from this figure.

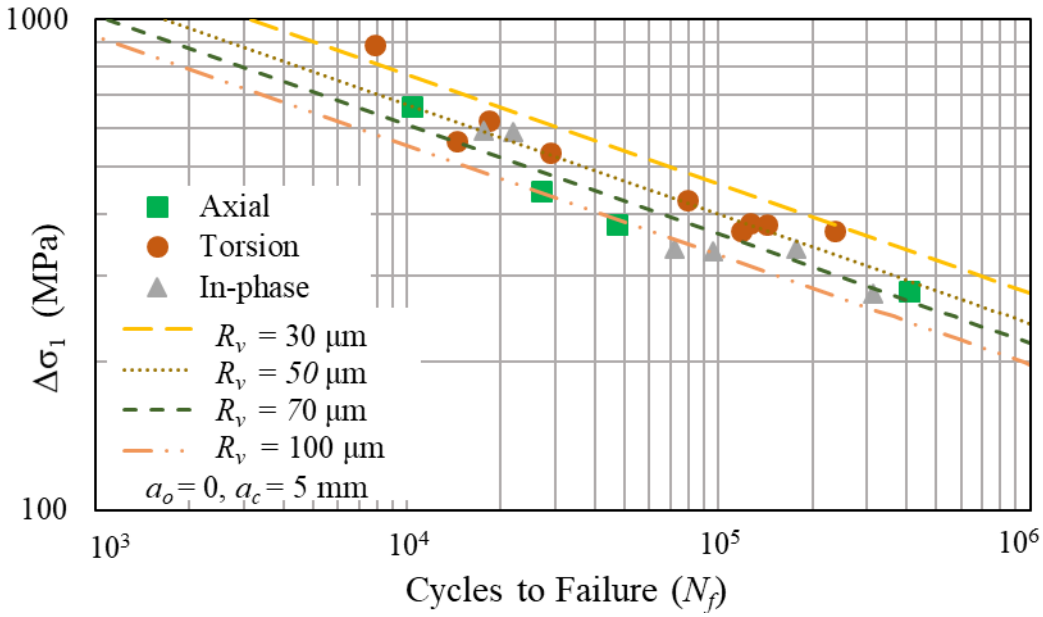

Figure 36. Experimental fatigue data from axial, torsion, and combined axial-torsion tests and fracture mechanics-based life predictions for annealed L-PBF Ti-6Al-4V, including prediction sensitivity to maximum valley depth, Rv [72].

5.6 Conclusion

In this study, the application of Taguchi and response surface method (RSM) for the design of experiment (DoE) in determining the DMLS processing parameters to achieve optimum properties were presented. Five DMLS processing parameters of laser power, scan speed, hatch spacing, layer thickness, and stripe width are considered for optimization of nine performance responses of relative density, microhardness, and six line and surface roughness parameters for top, upskin, and downskin surfaces. The major

conclusion is that both DoEs and models were successful in capturing the correlations between the DMLS processing parameters and responses by using only 1/125th of the full factorial experiments; i.e. each DoE only used 25 samples oppose to the total of 5^5 possible combinations of the DMLS processing parameters. The present analyses by both methods showed that the layer thickness is the dominant factor controlling downskin surface roughness parameters and it is a significant factor influencing top surface and upskin roughness parameters. On the other hand, the contribution of stripe width on most responses is negligible which was attributed to its local importance near the boundaries of parts. Microhardness and relative density were both influenced by energy density calculated based on laser power, scanning speed, layer thickness, and hatch spacing. However, laser power played a more dominant role in the microhardness response as opposed to the relative density response.

Furthermore, an artificial neural network (ANN) with six and five nodes in two hidden layers were established for predicting the responses of DMLS samples. The ANN was trained using the data used for the RSM DoE. Then, the responses corresponding to the Taguchi DoE were predicted by the ANN with a very good agreement with the actual values. In addition, the Taguchi model was used to predict the response of RSM DoEs and vice versa. The comparison of the prediction errors corresponding to ANN, RSM, and Taguchi showed that all the three models exhibit reasonable predictive capabilities while ANN outperforms the predictive capabilities of RSM and Taguchi.

Finally, the importance of the surface roughness characteristics on the fatigue performance of DMLS components was discussed. Future research suggestions include the need to correlate the fatigue performance to DMLS processing parameters by

developing models for fatigue-roughness correlations and implementing them in the present models.

Acknowledgements

This work is partially supported by the Contract N6893620C0022 from US Naval Air System Command through a subcontract from MRL Materials Resources LLC. This work is also partially funded through the Technology Development Grant by FedEx Institute of Technology.

References

[1] Y.M. Wang, T. Voisin, J.T. McKeown, J. Ye, N.P. Calta, Z. Li, Z. Zeng, Y. Zhang, W. Chen, T.T. Roehling, R.T. Ott, M.K. Santala, P.J. Depond, M.J. Matthews, A. V. Hamza, T. Zhu, Additively manufactured hierarchical stainless steels with high strength and ductility, Nat. Mater. 17 (2018) 63–70. doi:10.1038/NMAT5021.

[2] X. Zhao, A. Iyer, P. Promoppatum, S.C. Yao, Numerical modeling of the thermal behavior and residual stress in the direct metal laser sintering process of titanium alloy products, Addit. Manuf. 14 (2017) 126–136. doi:10.1016/j.addma.2016.10.005.

[3] J. Yin, L.L. Yang, X. Yang, H. Zhu, D. Wang, L. Ke, Z. Wang, G. Wang, X. Zeng, High-power laser-matter interaction during laser powder bed fusion, Addit. Manuf. 29 (2019). doi:10.1016/j.addma.2019.100778.

[4] B. Fotovvati, S.F. Wayne, G. Lewis, E. Asadi, A Review on Melt-Pool Characteristics in Laser Welding of Metals, Adv. Mater. Sci. Eng. 2018 (2018). doi:10.1155/2018/4920718.

[5] C. Qiu, M. Al Kindi, A.S. Aladawi, I. Al Hatmi, A comprehensive study on microstructure and tensile behaviour of a selectively laser melted stainless steel, Sci. Rep. 8 (2018). doi:10.1038/s41598-018-26136-7.

[6] G. Kasperovich, J. Haubrich, J. Gussone, G. Requena, Correlation between porosity and processing parameters in TiAl6V4 produced by selective laser melting, Mater. Des. 105 (2016) 160–170. doi:10.1016/J.MATDES.2016.05.070.

[7] G. Casalino, S.L. Campanelli, N. Contuzzi, A.D. Ludovico, Experimental investigation and statistical optimisation of the selective laser melting process of a maraging steel, Opt. Laser Technol. 65 (2015) 151–158. doi:10.1016/j.optlastec.2014.07.021.

[8] S. Pal, H.R. Tiyyagura, I. Drstvenšek, C.S. Kumar, The Effect of Post-processing and Machining Process Parameters on Properties of Stainless Steel PH1 Product

Produced by Direct Metal Laser Sintering, Procedia Eng. 149 (2016) 359–365. doi:10.1016/j.proeng.2016.06.679.

[9] A. Charles, A. Elkaseer, L. Thijs, V. Hagenmeyer, S. Scholz, Effect of process parameters on the generated surface roughness of down-facing surfaces in selective laser melting, Appl. Sci. 9 (2019) 1–13. doi:10.3390/app9061256.

[10] N. Perevoshchikova, J. Rigaud, Y. Sha, M. Heilmaier, B. Finnin, E. Labelle, X. Wu, Optimisation of selective laser melting parameters for the Ni-based superalloy IN-738 LC using Doehlert's design, Rapid Prototyp. J. 23 (2017) 881–892. doi:10.1108/RPJ-04-2016-0063.

[11] J.C. Fox, S.P. Moylan, B.M. Lane, Effect of Process Parameters on the Surface Roughness of Overhanging Structures in Laser Powder Bed Fusion Additive Manufacturing, Procedia CIRP. 45 (2016) 131–134. doi:10.1016/J.PROCIR.2016.02.347.

[12] M. Sadowski, L. Ladani, W. Brindley, J. Romano, Optimizing quality of additively manufactured Inconel 718 using powder bed laser melting process, Addit. Manuf. 11 (2016) 60–70. doi:10.1016/j.addma.2016.03.006.

[13] Z. Chen, Understanding of the Modeling Method in Additive Manufacturing, IOP Conf. Ser. Mater. Sci. Eng. 711 (2020). doi:10.1088/1757-899X/711/1/012017.

[14] I. Yadroitsau, Direct manufacturing of 3D objects by selective laser melting of metal powders, Saint-Etienne, 2008.

[15] D.C. Montgomery, Design and analysis of experiments, 9th ed., John Wiley and Sons, 2017.

[16] R.A. Fisher, Design of Experiments, BMJ. 1 (1936) 554–554. doi:10.1136/bmj.1.3923.554-a.

[17] R. Nath, M. Krishnan, Optimization of double diffusive mixed convection in a BFS channel filled with Alumina nanoparticle using Taguchi method and utility concept, Sci. Rep. 9 (2019) 19536. doi:10.1038/s41598-019-55897-y.

[18] H.Z. Jiang, Z.Y. Li, T. Feng, P.Y. Wu, Q.S. Chen, Y.L. Feng, S.W. Li, H. Gao, H.J. Xu, Factor analysis of selective laser melting process parameters with normalised quantities and Taguchi method, Opt. Laser Technol. 119 (2019). doi:10.1016/j.optlastec.2019.105592.

[19] S.L. Campanelli, G. Casalino, N. Contuzzi, A.D. Ludovico, Taguchi optimization of the surface finish obtained by laser ablation on selective laser molten steel parts, Procedia CIRP. 12 (2013) 462–467. doi:10.1016/j.procir.2013.09.079.

[20] F. Calignano, D. Manfredi, E.P. Ambrosio, L. Iuliano, P. Fino, Influence of process parameters on surface roughness of aluminum parts produced by DMLS, Int. J. Adv. Manuf. Technol. 67 (2013) 2743–2751. doi:10.1007/s00170-012-4688-9.

[21] D. Joguet, S. Costil, H. Liao, Y. Danlos, Porosity content control of CoCrMo and titanium parts by Taguchi method applied to selective laser melting process parameter, Rapid Prototyp. J. 22 (2016) 20–30. doi:10.1108/RPJ-09-2013-0092.

[22] R.F. Gunst, R.L. Mason, Fractional factorial design, 1 (2009) 234–244. doi:10.1002/wics.027.

[23] N. Read, W. Wang, K. Essa, M.M. Attallah, Selective laser melting of AlSi10Mg alloy: Process optimisation and mechanical properties development, Mater. Des. 65 (2015) 417–424. doi:10.1016/j.matdes.2014.09.044.

[24] M. El-Sayed, M. Ghazy, Y. Youssef, K. Essa, Optimization of SLM process parameters for Ti6Al4V medical implants, Rapid Prototyp. J. 25 (2019) 433–447. doi:10.1108/RPJ-05-2018-0112.

[25] H. Gajera, V. Darji, K. Dave, Application of Fuzzy Integrated JAYA Algorithm for the Optimization of Surface Roughness of DMLS Made Specimen: Comparison with GA, in: Adv. Intell. Syst. Comput., Springer Verlag, 2020: pp. 137–152. doi:10.1007/978-981-13-8196-6_13.

[26] F. Bartolomeu, S. Faria, O. Carvalho, E. Pinto, N. Alves, F.S. Silva, G. Miranda, Predictive models for physical and mechanical properties of Ti6Al4V produced by Selective Laser Melting, Mater. Sci. Eng. A. 663 (2016) 181–192. doi:10.1016/j.msea.2016.03.113.

[27] M. Krishnan, E. Atzeni, R. Canali, F. Calignano, D. Manfredi, E.P. Ambrosio, L. Iuliano, On the effect of process parameters on properties of AlSi10Mg parts produced by DMLS, Rapid Prototyp. J. 20 (2014) 449–458. doi:10.1108/RPJ-03-2013-0028.

[28] A. Pawlak, M. Rosienkiewicz, E. Chlebus, Design of experiments approach in AZ31 powder selective laser melting process optimization, Arch. Civ. Mech. Eng. 17 (2017) 9–18.

[29] Z. Li, Z. Zhang, J. Shi, D. Wu, Prediction of surface roughness in extrusion-based additive manufacturing with machine learning, Robot. Comput. Integr. Manuf. 57 (2019) 488–495. doi:10.1016/j.rcim.2019.01.004.

[30] I.A. Okaro, S. Jayasinghe, C. Sutcliffe, K. Black, P. Paoletti, P.L. Green, Automatic fault detection for laser powder-bed fusion using semi-supervised machine learning, Addit. Manuf. 27 (2019) 42–53. doi:10.1016/j.addma.2019.01.006.

[31] X. Qi, G. Chen, Y. Li, X. Cheng, C. Li, Applying Neural-Network-Based Machine Learning to Additive Manufacturing: Current Applications, Challenges, and Future Perspectives, Engineering. 5 (2019) 721–729. doi:10.1016/j.eng.2019.04.012.

[32] A.K. Sood, R.K. Ohdar, S.S. Mahapatra, Experimental investigation and empirical modelling of FDM process for compressive strength improvement, J. Adv. Res. 3 (2012) 81–90. doi:10.1016/j.jare.2011.05.001.

[33] D.E. Rumelhart, G.E. Hinton, R.J. Williams, Learning representations by back-propagating errors, Nature. 323 (1986) 533–536. doi:10.1038/323533a0.

[34] A.M. Khorasani, I. Gibson, A.H. Ghasemi, A. Ghaderi, Modelling of laser powder bed fusion process and analysing the effective parameters on surface characteristics of Ti-6Al-4V, Int. J. Mech. Sci. 168 (2020) 105299.

doi:10.1016/j.ijmecsci.2019.105299.

[35] V. Akhil, G. Raghav, N. Arunachalam, D.S. Srinivas, Image Data-Based Surface Texture Characterization and Prediction Using Machine Learning Approaches for Additive Manufacturing, J. Comput. Inf. Sci. Eng. 20 (2020) 1–16. doi:10.1115/1.4045719.

[36] B. Yuan, G.M. Guss, A.C. Wilson, S.P. Hau-Riege, P.J. DePond, S. McMains, M.J. Matthews, B. Giera, Machine-Learning-Based Monitoring of Laser Powder Bed Fusion, Adv. Mater. Technol. 3 (2018) 1800136. doi:10.1002/admt.201800136.

[37] Y. Zhang, G.S. Hong, D. Ye, K. Zhu, J.Y.H. Fuh, Extraction and evaluation of melt pool, plume and spatter information for powder-bed fusion AM process monitoring, Mater. Des. 156 (2018) 458–469. doi:10.1016/j.matdes.2018.07.002.

[38] A. Paul, M. Mozaffar, Z. Yang, W. Liao, A. Choudhary, J. Cao, A. Agrawal, A real-time iterative machine learning approach for temperature profile prediction in additive manufacturing processes, (2019).

[39] A. Caggiano, J. Zhang, V. Alfieri, F. Caiazzo, R. Gao, R. Teti, Machine learning-based image processing for on-line defect recognition in additive manufacturing, CIRP Ann. 68 (2019) 451–454. doi:10.1016/j.cirp.2019.03.021.

[40] C. Gobert, E.W. Reutzel, J. Petrich, A.R. Nassar, S. Phoha, Application of supervised machine learning for defect detection during metallic powder bed fusion additive manufacturing using high resolution imaging., Addit. Manuf. 21 (2018) 517–528. doi:10.1016/j.addma.2018.04.005.

[41] K. Aoyagi, H. Wang, H. Sudo, A. Chiba, Simple method to construct process maps for additive manufacturing using a support vector machine, Addit. Manuf. 27 (2019) 353–362. doi:10.1016/j.addma.2019.03.013.

[42] K. Wasmer, T. Le-Quang, B. Meylan, S.A. Shevchik, In Situ Quality Monitoring in AM Using Acoustic Emission: A Reinforcement Learning Approach, J. Mater. Eng. Perform. 28 (2019) 666–672. doi:10.1007/s11665-018-3690-2.

[43] S.A. Shevchik, C. Kenel, C. Leinenbach, K. Wasmer, Acoustic emission for in situ quality monitoring in additive manufacturing using spectral convolutional neural networks, Addit. Manuf. 21 (2018) 598–604. doi:10.1016/j.addma.2017.11.012.

[44] G. Tapia, A.H. Elwany, H. Sang, Prediction of porosity in metal-based additive manufacturing using spatial Gaussian process models, Addit. Manuf. 12 (2016) 282–290. doi:10.1016/j.addma.2016.05.009.

[45] M. Mehrpouya, A. Gisario, A. Rahimzadeh, M. Nematollahi, K.S. Baghbaderani, M. Elahinia, A prediction model for finding the optimal laser parameters in additive manufacturing of NiTi shape memory alloy, Int. J. Adv. Manuf. Technol. (2019). doi:10.1007/s00170-019-04596-z.

[46] M. Zhang, C.N. Sun, X. Zhang, P.C. Goh, J. Wei, D. Hardacre, H. Li, High cycle fatigue life prediction of laser additive manufactured stainless steel: A machine learning approach, Int. J. Fatigue. 128 (2019). doi:10.1016/j.ijfatigue.2019.105194.

[47] D. Gu, Y. Shen, Effects of processing parameters on consolidation and microstructure of W-Cu components by DMLS, J. Alloys Compd. 473 (2009) 107–115. doi:10.1016/j.jallcom.2008.05.065.

[48] M. Hiren, M.E. Gajera, K.G. Dave, V.P. Jani, Experimental investigation and analysis of dimensional accuracy of laser-based powder bed fusion made specimen by application of response surface methodology, Prog. Addit. Manuf. (2019). doi:10.1007/s40964-019-00076-8.

[49] C. Qiu, C. Panwisawas, M. Ward, H.C. Basoalto, J.W. Brooks, M.M. Attallah, On the role of melt flow into the surface structure and porosity development during selective laser melting, Acta Mater. 96 (2015) 72–79. doi:10.1016/J.ACTAMAT.2015.06.004.

[50] J. Sun, Y. Yang, D. Wang, Parametric optimization of selective laser melting for forming Ti6Al4V samples by Taguchi method, Opt. Laser Technol. 49 (2013) 118–124. doi:10.1016/j.optlastec.2012.12.002.

[51] H. Gong, K. Rafi, H. Gu, T. Starr, B. Stucker, Analysis of defect generation in Ti–6Al–4V parts made using powder bed fusion additive manufacturing processes, Addit. Manuf. 1–4 (2014) 87–98. doi:10.1016/J.ADDMA.2014.08.002.

[52] P. Promoppatum, R. Onler, S.-C. Yao, Numerical and experimental investigations of micro and macro characteristics of direct metal laser sintered Ti-6Al-4V products, J. Mater. Process. Technol. 240 (2017) 262–273. doi:10.1016/J.JMATPROTEC.2016.10.005.

[53] C.-F. Wu, M. Hamada, Experiments : planning, analysis, and optimization, Wiley, 2009.

[54] H.D. Beale, H.B. Demuth, M.T. Hagan, Neural network design, Pws, Boston, 1996.

[55] R.L. Wasserstein, N.A. Lazar, The ASA's Statement on p-Values: Context, Process, and Purpose, Am. Stat. 70 (2016) 129–133. doi:10.1080/00031305.2016.1154108.

[56] R.K. Roy, A primer on the Taguchi method, 2nd ed., Society of Manufacturing Engineers, 2010.

[57] T. Debroy, H.L. Wei, J.S. Zuback, T. Mukherjee, J.W. Elmer, J.O. Milewski, A.M. Beese, A. Wilson-Heid, A. De, W. Zhang, Additive manufacturing of metallic components-Process, structure and properties, Prog. Mater. Sci. 92 (2018) 112–224. doi:10.1016/j.pmatsci.2017.10.001.

[58] M. Mohammadi, H. Asgari, Achieving low surface roughness AlSi10Mg_200C parts using direct metal laser sintering, Addit. Manuf. 20 (2018) 23–32. doi:10.1016/j.addma.2017.12.012.

[59] Z. Chen, X. Wu, D. Tomus, C.H.J. Davies, Surface roughness of Selective Laser Melted Ti-6Al-4V alloy components, Addit. Manuf. 21 (2018) 91–103. doi:10.1016/j.addma.2018.02.009.

[60] G. Nicoletto, Directional and notch effects on the fatigue behavior of as-built

DMLS Ti6Al4V, Int. J. Fatigue. 106 (2018) 124–131. doi:10.1016/j.ijfatigue.2017.10.004.

[61] S. Kleszczynski, A. Ladewig, K. Friedberger, J. Zur Jacobsmühlen, D. Merhof, G. Witt, Position Dependency of Surface Roughness in Parts from Laser Beam Melting Systems, in: 26th Int. Solid Free Form Fabr. Symp., Austin, TX, 2015: pp. 10–12.

[62] Y. Tian, D. Tomus, P. Rometsch, X. Wu, Influences of processing parameters on surface roughness of Hastelloy X produced by selective laser melting, Addit. Manuf. 13 (2017) 103–112. doi:10.1016/j.addma.2016.10.010.

[63] H. Chen, D. Gu, J. Xiong, M. Xia, Improving additive manufacturing processability of hard-to-process overhanging structure by selective laser melting, J. Mater. Process. Technol. 250 (2017) 99–108. doi:10.1016/j.jmatprotec.2017.06.044.

[64] F. Calignano, Design optimization of supports for overhanging structures in aluminum and titanium alloys by selective laser melting, Mater. Des. 64 (2014) 203–213. doi:10.1016/j.matdes.2014.07.043.

[65] Y. Liu, J. Zhang, Y. Yang, J. Li, J. Chen, Study on the influence of process parameters on the clearance feature in non-assembly mechanism manufactured by selective laser melting, J. Manuf. Process. 27 (2017) 98–107. doi:10.1016/j.jmapro.2017.04.005.

[66] T. Vilaro, C. Colin, J.D. Bartout, As-fabricated and heat-treated microstructures of the Ti-6Al-4V alloy processed by selective laser melting, Metall. Mater. Trans. A Phys. Metall. Mater. Sci. 42 (2011) 3190–3199. doi:10.1007/s11661-011-0731-y.

[67] J. Yang, J. Han, H. Yu, J. Yin, M. Gao, Z. Wang, X. Zeng, Role of molten pool mode on formability, microstructure and mechanical properties of selective laser melted Ti-6Al-4V alloy, Mater. Des. 110 (2016) 558–570. doi:10.1016/j.matdes.2016.08.036.

[68] W.M. Tucho, V.H. Lysne, H. Austbø, A. Sjolyst-Kverneland, V. Hansen, Investigation of effects of process parameters on microstructure and hardness of SLM manufactured SS316L, J. Alloys Compd. 740 (2018) 910–925. doi:10.1016/j.jallcom.2018.01.098.

[69] F. Attarzadeh, B. Fotovvati, M. Fitzmire, E. Asadi, Surface roughness and densification correlation for direct metal laser sintering, Int. J. Adv. Manuf. Technol. 107 (2020) 2833–2842. doi:10.1007/s00170-020-05194-0.

[70] P. Li, D.H. Warner, A. Fatemi, N. Phan, Critical assessment of the fatigue performance of additively manufactured Ti-6Al-4V and perspective for future research, Int. J. Fatigue. 85 (2016) 130–143. doi:10.1016/j.ijfatigue.2015.12.003.

[71] A.F. Niloufar Sanaei, Analysis of the effect of surface roughness on fatigue performance of powder bed fusion additive manufactured metals, Theor. Appl. Fract. Mech. xxx (2020) xxx.

[72] J. Zhang, A. Fatemi, Surface roughness effect on multiaxial fatigue behavior of

additive manufactured metals and its modeling, Theor. Appl. Fract. Mech. 103 (2019) 102260. doi:10.1016/j.tafmec.2019.102260.

Appendix

Table 23 The L_{25} Taguchi orthogonal array for five factors and five levels

Experiment No.	Processing parameter level				
	A	B	C	D	E
1	0	0	0	0	0
2	0	1	1	1	1
3	0	2	2	2	2
4	0	3	3	3	3
5	0	4	4	4	4
6	1	0	1	2	3
7	1	1	2	3	4
8	1	2	3	4	0
9	1	3	4	0	1
10	1	4	0	1	2
11	2	0	2	4	1
12	2	1	3	0	2
13	2	2	4	1	3
14	2	3	0	2	4
15	2	4	1	3	0
16	3	0	3	1	4
17	3	1	4	2	0
18	3	2	0	3	1
19	3	3	1	4	2
20	3	4	2	0	3
21	4	0	4	3	2
22	4	1	0	4	3
23	4	2	1	0	4
24	4	3	2	1	0
25	4	4	3	2	1

Table 24 Fractional factorial design for five five-level factors

Experiment No.	Processing parameter level				
	A	B	C	D	E
1	0	0	0	0	0
2	0	1	1	2	3
3	0	2	2	4	1
4	0	3	3	1	4
5	0	4	4	3	2
6	1	0	1	1	1
7	1	1	2	3	4
8	1	2	3	0	2
9	1	3	4	2	0
10	1	4	0	4	3
11	2	0	2	2	2
12	2	1	3	4	0
13	2	2	4	1	3
14	2	3	0	3	1
15	2	4	1	0	4
16	3	0	3	3	3
17	3	1	4	0	1
18	3	2	0	2	4
19	3	3	1	4	2
20	3	4	2	1	0
21	4	0	4	4	4
22	4	1	0	1	2
23	4	2	1	3	0
24	4	3	2	0	3
25	4	4	3	2	1

Table 25 Raw data of all the experiments carried out for this research

Code*	Rel. density (%)	Hardness (HV, kg/mm^2)	Roughness (μm)						
			Top surface	Upskin surface	Up hor. line	Up ver. line	Down surface	Down hor. line	Down ver. line
11111	99.893	364.91	4.86	16.63	9.14	9.85	20.52	12.18	12.99
12222	99.726	354.80	7.54	19.55	11.62	13.86	19.73	13.00	14.63
12234	99.712	362.83	8.85	21.97	11.79	14.65	20.85	12.07	15.31
13333	98.493	343.40	15.86	23.72	13.72	14.67	22.30	13.28	15.08
13352	98.824	346.91	28.42	27.79	13.30	16.27	24.70	14.79	15.61
14425	97.379	340.33	17.09	24.46	12.75	15.95	20.30	14.00	14.64
14444	99.053	343.74	27.52	30.08	15.03	17.09	26.73	13.27	15.07
15543	99.431	341.80	32.52	32.27	17.12	21.52	28.18	15.54	15.10
15555	98.685	339.18	38.84	38.19	16.83	21.44	32.74	17.36	18.02
21222	99.732	357.64	5.26	18.96	7.74	12.66	23.64	15.26	13.14
21234	99.650	367.69	6.52	19.48	11.35	11.74	22.57	14.45	16.37
22345	99.258	361.82	11.23	24.02	11.15	14.51	24.29	14.14	14.68
23413	99.734	360.61	10.26	18.69	10.67	12.52	16.63	11.00	11.58
23451	98.493	343.4	23.30	30.04	13.63	16.58	27.03	15.02	14.56
24512	99.277	349.54	16.51	21.21	12.13	13.44	18.29	11.02	10.65
24531	97.399	352.40	20.98	26.77	13.65	14.84	24.70	14.99	16.37
25123	99.712	362.52	10.93	21.47	11.49	12.27	20.32	12.48	12.77
25154	99.383	361.53	12.83	26.63	14.11	15.21	25.48	16.45	15.91
31333	99.571	363.98	6.81	19.67	8.22	11.03	24.48	14.52	14.85
31352	99.503	365.48	9.81	23.61	10.04	12.70	28.47	13.81	15.31
32413	99.650	361.67	7.42	20.87	10.94	11.21	21.58	12.15	13.66
32451	99.573	362.20	13.39	25.31	11.62	15.71	27.59	15.37	16.12
33524	99.602	360.59	13.72	22.69	11.75	13.16	21.55	12.85	13.07
34135	99.646	364.18	6.79	22.11	11.86	13.48	22.60	14.97	15.11
34142	99.358	368.30	7.74	26.43	12.17	13.87	27.13	16.52	16.63
35215	99.789	364.02	11.74	25.00	12.59	17.80	19.41	12.19	11.94
35241	99.470	363.05	14.38	23.99	11.86	13.64	24.81	13.07	14.98
41425	99.684	366.77	7.96	19.36	9.68	11.12	22.39	13.23	14.40
41444	99.702	370.83	9.95	22.43	11.55	12.32	29.14	18.46	16.36
42512	99.735	365.98	8.54	23.54	11.36	14.14	24.15	14.66	13.68
42531	99.669	363.44	12.17	24.94	12.78	14.27	27.09	14.50	15.44
43135	99.801	370.56	15.24	19.02	10.35	10.46	24.93	14.97	15.63
43142	99.714	366.28	6.78	21.74	10.55	11.41	29.16	15.82	17.98
44253	99.286	363.92	13.00	25.16	11.50	13.91	28.96	15.70	16.69
45314	99.632	359.07	13.11	19.37	11.53	13.16	17.79	10.90	11.07
45321	99.516	361.75	13.55	23.36	11.83	14.93	23.58	13.75	13.48
51543	99.283	364.92	12.16	22.96	11.73	11.37	26.21	13.40	14.84
51555	99.570	372.44	12.78	25.81	10.37	13.27	31.39	17.78	15.67
52123	99.787	354.08	4.49	17.81	8.18	10.49	26.96	15.38	14.29

52154	99.681	358.51	5.83	17.92	6.97	11.25	29.87	13.65	17.58
53215	99.830	359.80	5.69	18.29	10.64	11.05	20.04	12.10	12.96
53241	99.615	360.61	7.69	25.32	11.88	13.62	39.59	20.22	20.96
54314	99.338	365.06	8.89	22.76	12.13	13.51	24.00	14.23	16.04
54321	99.600	361.15	9.55	22.83	11.81	13.81	23.74	14.02	13.58
55432	99.551	363.42	18.46	23.81	12.41	14.63	23.76	14.61	14.91

* Sample code is a five-digit code that each digit, from left to right, is representative for the level of factors A, B, C, D, and E, respectively, as shown in Table 15. For instance, the factor levels of the sample 12234 are A1, B2, C2, D3, and E4.

6. Conclusion

In this dissertation, the process-property-geometry correlations in the DMLS process of Ti-6Al-4V parts are thoroughly investigated and optimization methods for this process are evaluated and discussed. First, because of the significance of the melt-pool characteristics in determining the correlations between processing parameters and the properties of products, a state-of-the-art literature review on the properties of the melt-pool in laser welding and the relationship between welding process parameters and melt-pool characteristics, including geometry, thermodynamics, fluid dynamics, microstructure, and porosity is presented in chapter two.

The third chapter is dedicated to the investigation of the effect of size, geometry, and the location on the build platform, on the geometrical accuracy of DSLM manufactured parts. Results for various geometries such as walls, squares, tubes, and rods with different sizes, showed that with decreasing the feature size the error percentage increases. While all the geometric features follow this trend, a stronger size dependence of the error was observed for the geometries without curvatures, i.e. walls and squares. The possible cause of these dimensional inconsistencies is demonstrated to be the size-dependent shrinkage during the DMLS process because the geometry dependence of the error diminishes for features larger than 1 mm and the size dependence of the error converges to a fixed value for sufficiently large features. Additionally, the dimensional inaccuracy is shown to be independent of the location on the build platform in the DMLS process.

The effect of thickness, orientation, distance from free edges, and height on mechanical properties of DMLS-manufactured sheets and their correlation to material microstructure and thermal history as dictated by process parameters lead to the

following conclusions. Decreasing the sheet thickness results in lower cooling rates and accumulation of more heat in the sheets, causing more gas trapped porosities due to overheating. Testing specimens in different orientations resulted in obtaining a trend in the values of the tensile strength, i.e. an increase from 0° to 30°-45° and then a decrease from 45° to 90°. An opposite trend was observed in the variations of elongation at break. These behaviors are attributed to the competition between two opposing factors, namely the defect orientation factor and the β grain width factor. The variations of tensile strength versus height showed a significant decrement at high heights that is attributed to the increase in the porosity and prior β grain width with increasing height, which is affected by cooling mechanisms of the sheets during the process. A similar trend was observed in microhardness variations versus height, while it decreases by increasing the thickness of the sheets in contradiction with the trend observed for tensile strength. This is attributed to the decomposition of α′ to α and β, increasing the size of β nanoparticles, and/or the formation of the soft orthorhombic α″ during the DMLS process. Furthermore, it was observed that the distance from the free edge is insignificant in determining the mechanical properties of the DMLS-manufactured since the heat conduction to the build platform and convection through the side of the free surfaces are uniform at each layer in thin sheets. Moreover, the oxygen content increases exponentially with the height due to longer exposure of the material at high temperature to a low amount of Oxygen in the Argon inert gas due to the slower cooling rates at higher heights.

In the final chapter, two DoE techniques, including Taguchi and RSM are employed to determine the effects of five DMLS processing parameters on nine response properties and to achieve optimum properties. Furthermore, an ANN is presented to predict the

properties of DMLS samples with very high accuracy. The comparison of the prediction errors corresponding to Taguchi, RSM, and ANN showed that all three models exhibit reasonable predictive capabilities while ANN outperforms the predictive capabilities of RSM and Taguchi.

Future Work

Observation of melt-pool correlations with the processing parameters suggests several areas for future study. Apart from reducing the simplification assumptions in melt-pool modeling, more sophisticated methods of melt-pool monitoring can help to generate more experimental data on a wide collection of alloys and processing parameters, yielding results that would enhance verification and validation of models.

All the experiments for obtaining the process-property-geometry correlations that are discussed in this dissertation are carried out on as-fabricated DMLS parts without any post-processing. However, most of the time in real applications in industry, DMLS-manufactured components are heat-treated after being manufactured. Therefore, the effect of different heat treatments needs to be investigated on the process-property-geometry correlations presented in this dissertation.

Finally, the correlations between the fatigue performance of DMLS-manufactured parts and the processing parameters need to be more investigated by developing models for fatigue-roughness correlations and implementing them in the models presented in this dissertation.